Dynamical evolution of local gas-rich galaxy mergers from NIR spectroscopy

DISSERTATION

der Fakultät für Physik der Ludwigs-Maximilians-Universität München
zur Erlangung des Grades
Doktor der Naturwissenschaften
Dr. rer. nat.

vorgelegt von

Kalliopi-Maria DASYRA aus Athen, Griechenland

München, den 1. Mai 2006

Erstgutachter : Prof. Dr. Reinhard Genzel
Zweitgutachter : Prof. Dr. Andreas Burkert
Tag der mündlichen Prüfung : 23 Oktober 2006

Contents

Résumé / Zusammenfassung

This study aimed to trace how the stellar kinematics evolve when two gas-rich galaxies merge. To study the evolution of such mergers, Very-Large-Telescope observations were performed for the best-suited galaxy population in the local Universe, the Ultraluminous Infrared Galaxies (ULIRGs). The prodigious infrared emission in ULIRGs originates from the intense star formation that occurs when large amounts gas are driven to the center of the merging system. We acquired near-infrared H- and K-band spectroscopic data of 54 ULIRGs at various merger phases; approximately half of the sources in our sample have two distinct nuclei. For each source, we derived the stellar kinematics from the high-resolution spectra by studying the profile of the stellar CO absorption lines. The shape of the profile along various slit positions enables us to measure the rotational velocity, $V_{\rm rot}$ and velocity dispersion, σ, and to compute the stellar and black hole (BH) masses. We find that ULIRGs are mostly triggered by mergers of roughly equal-mass galaxies. Their mean velocity dispersion equals 150($\pm$ 33) km s^{-1} . A possible trend of dynamical heating of the galaxies as the merger evolves is observed at marginal statistical levels. The kinematic, structural, and photometric properties of ULIRGs indicate that they are dispersion-dominated systems and that they mainly result in the formation of 10^{10}-10^{11} $M_{\odot}$ mass elliptical galaxies (Es). Their locus on the fundamental plane of Es indicates that their end products are typically inconsistent with giant Es. The BH masses in ULIRGs are of the order 10^{7}- 10^{8} $M_{\odot}$. To investigate whether ULIRGs go through quasar (QSO) phases during their evolution, we have acquired similar data for 12 local Palomar-Green (PG) QSOs. The mean bulge dispersion of the PG QSOs in our sample equals 186 ($\pm$24) km s^{-1} . The measurement of the stellar dispersion in QSOs enables us to place them on significant observational diagrams, such as the local BH mass and host-galaxy bulge relation and the fundamental plane of Es. On the latter, PG QSOs are located between the regions occupied by moderate-mass and giant Es. Their bulge and BH masses are on the order of $10^{11} M_{\odot}$ and $5 \times 10^{7} - 10^{8}$ $M_{\odot}$ respectively. PG QSOs seem to be triggered by gas-rich mergers, and therefore likely formed in an analogous manner to ULIRGs. However, other local QSOs with supermassive black holes of $5 \times 10^{8} - 10^{9} M_{\odot}$ that reside in massive spheroids have a different formation mechanism.

Diese Arbeit untersucht die Entwicklung der stellaren Kinematik im Falle einer Verschmelzung zweier Galaxien mit hohem Gasgehalt. Zur Untersuchung der Evolution derartiger Verschmelzungen wurden Vertreter der hierfür am besten geeigneten Galaxienpopulation im lokalen Universum, die Ultraluminous Infrared Galaxies (ULIRGs), mit dem Very Large Telescope beobachtet; die Infrarotemission dieser ULIRGs hat ihre Ursache in intensiver Sternentstehung, die auftritt, wenn grosse Mengen an Gas in das Zentrum des verschmelzenden Systems transportiert werden. Wir haben spektroskopische Nah-Infrarot H- und K-Band-Daten für 54 ULIRGs in verschiedenen Stadien der Verschmelzung gewonnen; etwa die Hälfte dieser Quellen besitzt zwei getrennte Kerne. Für jede Quelle haben wir die stellare Kinematik aus hochaufgelösten Spektren durch Untersuchung der Profile stellarer CO-Absorptionslinien bestimmt. Die Linienprofile (und ihre Änderung mit der Spaltposition) ermöglichen uns die Messung der Rotationsgeschwindigkeit $V_{\rm rot}$ und der Geschwindigkeitsdispersion σ, sowie die Berechnung der Massen der Sterne und der Schwarzen Löcher (SL). Wir kommen zu dem Schluss, dass ULIRG-Aktivität im Wesentlichen durch die Verschmelzung von Galaxien annähernd gleicher Masse verursacht wird. Ihre mittlere Geschwindigkeitsdispersion beträgt 150 (33) km/s. Eine mögliche Tendenz in Richtung dynamischer Aufheizung der Galaxien mit fortschreitender Verschmelzung ist mit marginaler statistischer Signifikanz beobachtbar. Die kinematischen, strukturellen und photometrischen Eigenschaften von ULIRGs deuten darauf hin, dass sie dispersionsdiminierte Systeme sind und sie im Wesentlichen in der Bildung von elliptischen Galaxien (Es) mit 10^{10} - 10^{11} Sonnenmassen resultieren. Ihre Position in der Fundamentalebene der Es zeigt an, dass ihre Endprodukte typischerweise inkonsistent mit Riesen-Es sind. Die Massen der SL in ULIRGs bewegen sich im Bereich 10^7 - 10^8 $M_\odot$. Um zu untersuchen, ob ULIRGs während ihrer Entwicklung Quasar-Phasen durchlaufen, haben wir vergleichbare Daten von 12 lokalen Palomar-Green QSOs (PG QSOs) gewonnen. Die mittlere Bulge-Dispersion der PG-QSOs in unserer Stichprobe beträgt 186 (24) km s^{-1} . Die Vermessung der stellaren Dispersion in QSOs erlaubt es uns, sie in geeignete Diagramme, wie die Relation von lokaler SL-Masse und Geschwindigkeitsdispersion des galaktischen Bulges, sowie die Fundamentalebene der Es, einzutragen. Im zuletzt genannten Fall befinden sich PG-QSOs zwischen den Regionen von Es mittlerer Masse und denen von Riesen-Es. Ihre Bulge-Massen betragen um 10^{11} $M_\odot$, die Massen der SL um $10^{11} M_\odot$ and $5 \times 10^7 - 10^8$ $M_\odot$. PG QSOs scheinen ihren Ursprung in Verschmelzungen gasreicher Galaxien zu haben analog zu ULIRGs. Allerdings zeigen andere lokale QSOs mit supermassiven Schwarzen Löchern in massiven Sphäroiden eine unterschiedliche Entstehungsgeschichte.

1

Introduction: Galaxy mergers in a general framework

1.1 The role of mergers in galaxy evolution

The mergers of galaxies have been under examination for several decades. Already in 1941, Holmberg (1941) created an experiment to study how two rotating galaxies merge using light bulbs to simulate the stars in each galaxy. Somewhat later, observations of galaxies with perturbed morphologies and clear signs of interactions were performed (e.g., Arp 1966). While some cases showed an unambiguous sign of interaction, the presence of 2 perturbed galaxies, other showed tails of undetermined origin. In 1972, in what has become the seminal work on galaxy mergers, Toomre and Toomre pointed out that these perturbations had originated from galactic mergers instead of e.g. winds or outflows. The origin of these objects was then clearly established. Still, galaxy mergers were thought as local oddities. Toomre (1977) further suggested that mergers may convert one galaxy type (spiral) into another (elliptical) along the Hubble sequence. In the 90s it was clear that mergers drive galaxy evolution by forming elliptical galaxies (e.g., Kormendy & Sanders 1992; Kauffmann & White 1993). Nowadays, all recent simulations of galaxy formation and evolution (e.g. Springel et al. 2005c) aim to optimize the parameters upon which the mergers depend to allow for a better understanding of the galaxy counts at all redshifts.

Mergers not only transform one galaxy type into another but, during their

occurence, drive phenomena that are extra-ordinary compared to the processes that take place in quiescent galaxies. Such phenomena are the very intense formation of stars (starbursts), the formation of a central massive object (a black hole) and the accretion of matter upon it (see § 1.2 for more details). By altering the dominant stellar population in the colliding galaxies and forming objects with different stellar structure and orbits, mergers drive the most important phenomena in galaxy evolution and affect or explain various observational relations. Such examples are the luminosity function (which is the density of a galaxy type per luminosity bin; see Schechter 1976 and references therein), the fundamental plane of early-type galaxies (Djorgovski & Davis 1987; Dressler et al. 1987), and the relation between the black hole mass and the bulge dispersion in a galaxy (Ferrarese et al. 2001; Gebhardt et al. 2001). The origin and the influence of mergers on these relations are the object of study of many recent simulations (e.g. Hopkins et al. 2006; Kaviraz et al. 2006; Robertson et al. 2006a, Robertson et al. 2006b).

Accumulating evidence shows that the significance of mergers was higher in the early universe than at redshift z=0 (mainly from submillimeter studies, mid-infrared selected samples, and mid-infrared follow-up of deep optical surveys; see a nice review by Lonsdale et al. 2006). This is in part due to the small volume that the early Universe occupied. Furthermore, the younger galaxies had higher gas fractions (since smaller amounts of gas had collapsed to form stars) than present day galaxies. A dramatic increase in the number of mergers in the high-redshift Universe is predicted by several recent models of galaxy formation (Springel et al. 2005c; Khochfar & Burkert 2003; Kaviraz et al. 2006). The peak of the merger-induced infrared (IR) emission is believed to be in the redshift range $1 \lesssim z \lesssim 2$ (e.g., Pérez-González et al. 2005, Lagache et al. 2004, Elbaz 2005) and it is mainly responsible for the presence of a cosmic infrared background (Puget et al. 1996; Dwek et al. 1998).

1.2 The predicted evolution of galaxy mergers

The evolution and outcome of mergers of two gas-rich galaxies has been extensively studied in the literature from a theoretical viewpoint (e.g., Hernquist 1993; Barnes & Hernquist 1996; Mihos & Hernquist 1996; Naab & Burkert 2003; Springel et al. 2005b). The main parameters that determine the end products of such mergers are believed to be well understood; the outcome mainly depends upon the initial amount of gas and the mass ratio of the merging spiral galaxies (e.g., Mihos & Hernquist 1996; Mihos & Bothun 1998; Bendo & Barnes 2000; Naab & Burkert 2003; Mihos & Hernquist

1994). The importance of gas in the merger process is that it is provides a dissipative component that assists the collapse of the mass to the center of the system by overcoming the angular momentum which tends to drive the mass towards the exterior of the system (Hernquist et al. 1993; Hernquist & Mihos 1994); this way it enables the formation of systems with elliptical-like intensity profiles. The mass ratio of the initial galaxies is connected to the depth of the potential well of the most massive component and it is therefore proportional to the amount of gas of the least massive component that inflows to the center of the system.

For gas masses typical of those of local galaxies (i.e., $\sim$10% of the stellar mass) mergers of roughly equal mass systems, the so-called major mergers, lead to the formation of elliptical galaxies. In contrast, mergers of large mass ratio ($> 4 : 1$), which are called minor, can preserve or even enhance the pre-existing angular momentum depending on the orientation of the merging system (e.g., Mihos et al. 1994; Mihos & Hernquist 1996; Bendo & Barnes 2000).

The picture of how a major merger of gas-rich galaxies evolves in the local Universe is believed to be as follows: As the two galaxies approach each other, their stellar disks collide and distort and their gas starts flowing towards the center of the system. This phase is called "first encounter". As the distance between the galaxies decreases, the gravitational attraction between the bulges increases and so does the gas infall towards the center of the merger as a result of dissipation. The stars follow the gas in its infall due to changes in the potential well of the merging system that take place within less than a dynamical timescale ("violent relaxation"). Long tails (consisting of both stars and gas) are also formed due to gravitational torques and tidal forces caused by angular momentum conservation constraints. The two galaxies continue to approach one another until the time they reach the perigalacticon; due to momentum conservation they continue moving in a divergant orbit prior to falling back towards each other. At that point they rotate (possibly several times) around each other before they finally merge and reach relaxation. After the nuclei coalesce, the gas infall to the center of the merger decreases; it finally stops $\sim$ a few 10^8 yrs later due to outflowing supernova winds related to the on-going star formation and to feedback to the interstellar medium (ISM) from an active galactic nucleus (AGN). The final remnant is supported mainly by random motions instead of systematic rotation. The whole baryonic-matter-merger process takes $\sim 10^9$yrs. A description of this merger picture is presented in Fig. 1.1. This picture is taken from Springel et al. (2005b) and shows the evolution of the gas in the disks as the merger advances.

The end products of major mergers of high-redshift spiral galaxies are more

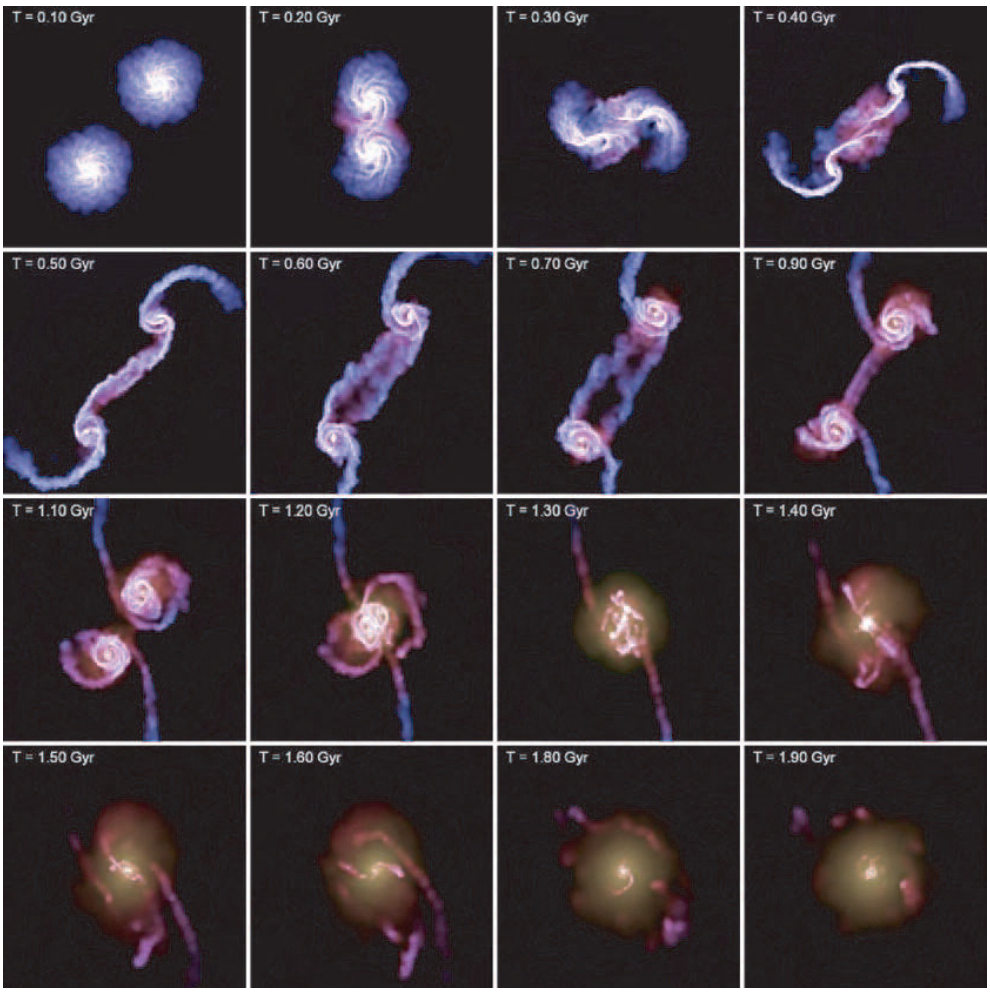

Figure 1.1: The dynamical evolution of the gas disks in a binary merger (taken from Springel et al. 2005b). The color map contains temperature information; blue colors have colder temperatures than red colors; the cold gas in the initial disks gets dynamically hot as the merger evolves. At the end most of the gas is either accreted to the center of the remnant or blown away. The geometry of the remaining gas is much more random-motion-dominated than that in the initial well-structured disks.

diverse because the amount of gas contained in their disks was greater than that in the current-epoch disks [1]. Simulations that assume the initial disks

[1] The gas fraction in high-z galaxies is higher than than in local spirals by up to 40% according to recent observations (Neri et al. 2003; Greve et al. 2005; Tacconi et al. 2006).

to be of gaseous nature indicate that the outcome of high-z gas-rich mergers may either be an elliptical or even a spiral galaxy that possesses a massive bulge (Springel et al. 2005a; Springel & Hernquist 2005). The result again depends on the amount of gas in the initial galaxies (it is found for purely gas disks) and on the presence of a bulge and an AGN. According to Springel et al. (2005a), the most important parameters for the determination of the outcome are the assumptions made for the way the AGN couples with its surrounding gas; these namely are the fraction of the gas accreting onto the black hole and the feedback of this accretion to the ISM.

While the picture we have for the end products of spiral-spiral (S-S) or gas-rich mergers [2] is well understood, that for the intermediate merger phases (i.e. between first encounter and final relaxation) is rather unclear. The uncertainties mainly originate from the simplified treatment of the ISM (i.e., the gas and the dust). For example, it is not well understood at what point in time the gas infall to the center of the merger is maximum; since the amount and pressure of the gas regulate the formation of new stars, it is unclear at what point the strongest star formation or starburst events occur. In individual sources, the time that the major starburst takes place may significantly vary (e.g., Mihos & Bothun 1998). On a statistical basis, it is believed that the starburst peaks roughly between first encounter and shortly after nuclear coalescence (see Fig. 1.2 ; Mihos & Hernquist 1996; Springel et al. 2005b; Di Matteo et al. 2005). The result mainly depends upon the size of the galaxy bulges (since large bulges stabilize the gas and delay its fall to the center of the system), the presence of a black hole (since it acts as a strong gravitational point at the center of the system), and the strength of the winds from the supernovae and the AGN (since they drive gas away from the center). Since the gas that flows to the center of the merger is responsible for both initiating circumnuclear starbursts and feeding the AGN, the growth of the central black hole depends upon the same parameters and carries similar uncertainties. It is not established, for example, whether the AGN accretion can be often strong enough to lead to an emission similar to those of Quasi-Stellar Objects (QSOs), i.e. 10^{12} $L_{\odot}$. Such a scenario was presented in Sanders et al. (1989) who suggested that ULIRGs go through a phase of high accretion onto the central AGN beyond the coalescence of the merging nuclei and prior to the formation of fully-relaxed remnants; this emission would reach QSO luminosities once most of the gas and the dust are either exhausted in star formation or expelled by winds from the center of the system, revealing the

[2] Onwards, spirals are often denoted as "gas-rich" galaxies; this term is broader and more appropriate for the merging systems under examination since it does not relate the presence of gas with the strength of the spiral structure in the disk.

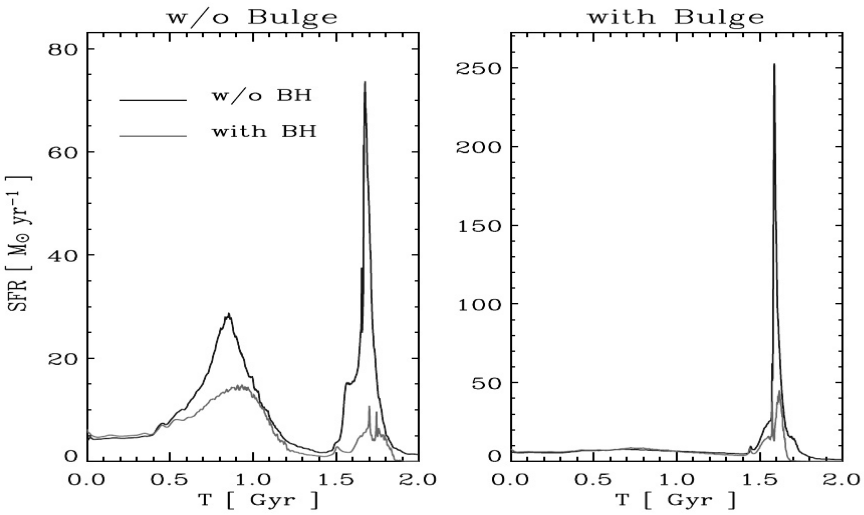

Figure 1.2: The predicted evolution of the star formation rate for gas-rich merger models that show how the major starburst depends upon a) the presence of a bulge, b) the presence of a black hole (and the accretion onto the black hole and its feedback to the ISM). This figure is from Springel et al. (2005b) who overlayed their results (black solid line) to those of Mihos & Hernquist (1996) (gray solid line). The presence of a bulge delays and that of a black hole suppresses the star-formation event(s) which can otherwise already occur after the first encounter (see Fig. 1.1).

central AGN. Furthermore, the relative strength at any point in time of the closely-related starburst and AGN activities (e.g., Scoville et al. 2003) is not known. Such questions are addressed by seeking observational constraints to the scenarios suggested in the literature.

Other types of merger (i.e., between a spiral and an elliptical galaxy and two ellipticals) have not been studied as systematically as gas-rich mergers. Spiral-elliptical (S-E) mergers are also believed to enhance the star-formation and AGN-accretion activity; however these activities in S-E mergers will be less intense than in gas-rich mergers since the latter possess greater amounts of gas then the former. Elliptical-elliptical mergers (E-E; the so-called "dry" mergers) are non-dissipative and therefore do not have significant AGN-accretion or star-forming events (van Dokkum 2005; Bell et al. 2006). The remnants of E-E mergers are predicted to have an increased mass and degree of random motions compared to the progenitor ellipticals, resembling mainly local giant Es (Naab et al. 2006).

1.3 Observational classification of mergers

To study the evolution of galaxy mergers it is of primary importance to observationally identify objects representing each merger category. Unfortunately, it is rather difficult to disentangle the various merger categories based on the often-used method of visual recognition. The latter is only possible in the case of mergers in early phases where both components are not significantly perturbed and their type can be identified. For the advanced mergers, where the individual components cannot be disentangled, it is not easy to distinguish between all possible initial conditions. Therefore, to select a homogeneous sample of mergers, i.e. S-S, E-S, or E-E, one needs to set criteria other than visual classification.

The most common method that has been established to identify mergers or interactions of gas-rich galaxies is related to the identification of an excess of infrared emission; the IR emission is known to originate from dust thermal radiation in star-forming clouds and AGN accretion, both phenomena triggered or enhanced by gas-rich mergers. The classification of mergers according to their IR emission was mainly used after the launch of the Infrared Astronomical Satellite (IRAS) in 1983, when a plethora of sources with high emission at 12, 25, 100, and 160 μm was discovered (Houck et al. 1985), although sources that output IR luminosity comparable to that in the optical were known to exist since 1970 (see Sanders & Mirabel 1996, Lonsdale et al. 2006 and references therein). According to their (mid- and far-) infrared luminosity $L_{\rm IR}$ (integrated from 8 to 1000 μm) mergers are classified as follows:

- **HyLIRGs:** The Hyper-Luminous InfraRed Galaxies (HyLIRGs) are the brightest of all gas-rich mergers. The IR luminosity of HyLIRGs is greater than 10^{13} $L_{\odot}$ and requires vast amounts of gas to generate such strong starburst and AGN emission. Given their extremely gaseous nature, HyLIRGs are particular of the high-redshift Universe.

- **ULIRGs:** Ultra-luminous InfraRed Galaxies (ULIRGs) have IR luminosities in the range $10^{12} < L_{\rm IR} < 10^{13}$ $L_{\odot}$. ULIRGs originate from the merger of two gas-rich galaxies, in order to possess the requered amount of gas to shine with bolometric luminosities comparable to those of quasi-stellar objects (QSOs). Although the volume density of ULIRGs increases with redshift (Lonsdale et al. 2006 and references therein), local ULIRGs are also rather frequent objects; they are 4 times more common (Sanders & Mirabel 1996) that the most bright local QSOs in the Palomar-Green Bright QSO survey (Schmidt & Green 1983). Given their number counts and their well-defined initial conditions (which are practically restricted to gas-rich mergers), local ULIRGs are the most

appropriate population fot the observational study of the evolution of galaxy mergers.

- **LIRGs:** With an IR luminosity $10^{11} < L_{\rm IR} < 10^{12}$ $L_{\odot}$, Luminous InfraRed Galaxies (LIRGs) are believed to have a wide variety of origins. Given their IR emission, which is higher than that of quiescent spirals, LIRGs require the presence of at least 1 gas-rich component to trigger their intense star formation episodes. However, they may sample both the gas-rich, and E-S merger categories, or even be triggered by other kind of interactions (e.g. fly-by) of spiral galaxies (e.g, Ishida 2004; Wang et al. 2006). Some LIRGs could become ULIRGs or could be former ULIRGs that faded away since all ULIRGs pass through a LIRG phase before and after the peak of their IR emission (Mihos & Bothun 1998). Other LIRGs do not possess adequate amounts of gas to overcome the $L_{\rm IR} > 10^{12}$ threshold. Given their wide range of merger properties, LIRGs are also frequent in the local Universe, although their number density peaks at $z \sim 1$ (Pérez-González et al. 2005).

1.4 Aim, observations, and techiques of this work

The scope of this work is to trace observationally the evolution of mergers in the local Universe. For this purpose we have carried out observations of the merger population with the most well-defined properties, the local ULIRGs, to solely sample gas-rich mergers. We have obtained spectroscopic data for 54 ULIRGs at various merger phases to derive their stellar kinematics. The observed sources sample a wide range of projected nuclear separations, from 40 kpc to fully merged systems.

We have also made similar spectroscopic observations of 12 local QSOs, to investigate dynamical links between the local ULIRGs and QSOs, following scenarios which suggest that gas-rich mergers undergo short QSO phases prior to forming fully-relaxed remnants (see § 1.2). These observations were initially carried out as part of a pilot program since the extraction of the stellar kinematics in the brightest local QSOs had not been presented before. The reason is the presence of the strong continuum from the localized AGN emission, which originates from the dust that surrounds the AGN. This dust component is heated by the AGN to temperatures of the order 1000 K (the grains dissipate at 1500K) and emits a thermal continuum that peaks between 2-3 μm. At the center of the system, the luminosity of this continuum is strong, more than an order of magnitude, compared to that of the stars. Therefore, it overwhelms the stellar light. To extract the kinematics of the host galaxy in a QSO, one needs to sample the host at large apertures, i.e.,

apertures roughly equal or larger than 1 half-light radius, $R_{\rm eff}$. However, at those apertures the photon flux falls to less than 20% of its central value. To overcome this problem the use of an 8-m class telescope is crucial; for this reason we carried out our observations at the Very Large Telescope (VLT) of the European Southern Observatory (ESO) at Cerro Paranal, Chile. The excellent seeing conditions that constrained the spatial extent of the AGN light, and the long on-source integrations (of 3-5 hrs) assisted our observations and enabled us to extract the host dynamics from the QSO data. In total, the observations of this program were allocated 21 nights (plus 3 nights of weather compensation) at the VLT [3].

The near-infared (NIR) spectrograph ISAAC (Moorwood et al. 1998) mounted on the Unit Telescope 1 of the VLT was used for the observations, with a spectral resolution $R = \lambda/\delta\lambda$ of 5100. The observations were carried out in the NIR regime, since ULIRGs are extremely obscured by the dust that inflows to the center of the merger (together with the gas); the dust affects the measured stellar dynamics (Baes & Dejonghe 2002; Silge & Gebhardt 2003) by absorbing light from the central regions of a galaxy where the velocity dispersion σ is highest and scattering a part of this light to the edges of the galaxy where σ is small. To avoid these effects, we chose to observe our sources in the H or in the K band, depending on the redshift of each source and the windows of atmospheric transparency. In these wavelengths, the stellar kinematics are mainly traced by the rovibrational transitions of CO molecules in the atmosphere of stellar giants and supergiants. To determine the stellar kinematics of a stellar ensemble, a template star that indicates the intrinsic shape of each absorption feature is needed. The kinematics of the entire galaxy can then be derived by comparing the line-of-sight (LOS) profile of the absorption feature compared to that of the template. Deviations between the two originate from the addition of red- or blue- shifted photons, which originate from various stars moving at different directions. Changes (of the peak) of the profile along different LOS enable us to measure the rotational velocity , $V_{\rm rot}$ and the width of the profile is a measure of the stellar velocity dispersion.

Various methods that extract the actual value of these velocity moments from the observed spectrum with the aid of a stellar template have been presented in the literature. The most common ones are the χ^2 minimization (see "Numerical Recipes", Press et al. 1992, and references therein) and the Fourier quotient techniques (e.g., Simkin 1974; Sargent et al. 1977). The former method first creates broadened spectra by convolving the spectral template with Gaussians of various dispersions and then selects the most ap-

[3]Large Program ID: 171.B-0442

propriate dispersion value by solving for the minimum difference between the χ^2 of the convolved and the observed spectrum. In the Fourier metholodogy, the template and the galaxy spectra are Fourier transformed to take advantage of the fact that in Fourier space convolution equals multiplication. The broadening function is computed from the ratio of the transformed galaxy function over the transformed template function and then converted back into normal space. However, this method assumes that the two observed functions can be described by series of exponentials of identical coefficients; in case of a template mismatch, wiggles are introduced to the resulting broadening function (Bender 1990). In this paper we use a somewhat more sophisticated technique presented in Bender (1990), which is less sensitive to template mismatch. The idea behind this method is that instead of computing the quotient of the Fourier-transformed functions, it is more accurate to compute the quotient of the correlation function of the galaxy and the template spectrum over the autocorrelation function of the template spectrum. Due to the multiplicative nature of convolution in Fourier space, the resulting broadening function should be theoretically identical to that of the simple Fourier quotient technique. Practically, the peaks of the correlation are mostly taken into account on the computation of the broadening function, providing a weight at those wavelengths where the resemblence between the template and the galaxy spectrum is maximum. Therefore, this method is more stable to template mismatch caused e.g., by noise that destroys the wings of the spectral features. Furthermore, a Wiener filter is also applied in Fourier mode to remove high-frequency signal (noise). We then compute the peak and the full-width-half-maximum (FWHM) of the broadening function (in normal space) by fitting a combination of a Gaussian and a low-order polynomial to it [4]. The velocity dispersion can then be easily computed as σ=FWHM/2.35 and the rotational velocity from the maximum difference in the peak of the broadening function along symmetric lines of sight.

The reduction of the spectra from which the kinematics of the sources are derived is not identical for local ULIRGs and QSOs. The data extraction techniques are therefore presented for each population in the chapter where it respectively appears. The chapters are organized as follows: In chapter 2 we study what are the initial conditions that are required for a merger to appear as ultraluminous in the mid- and far- infrared, through a study of the kinematics of binary sources. In chapter 3 we investigate for evolution of the

[4] If the broadening function is fitted with a Gauss-Hermite polynomial instead, then the curtosis and the skewness of the function provide further information on the stellar orbits (Bendo & Barnes 2000). This information can only be extracted for few nearby sources where the signal-to-noise ratio is sufficiently large to study the behaviour of the high moments of the distribution along several apertures.

stellar kinematics during the ultraluminous phases of a gas-rich merger by comparing the kinematics before and after nuclear coalescence. We further investigate what the end products of ULIRGs are by comparing the dynamical properties of the remnants to those of ellipticals. In chapter 4 we present the stellar dynamics in bright local QSOs and compare them to those of ULIRGs to investigate for similarities in the evolution of the two populations. In chapter 5 we summarize all conclusions derived from the analysis of the stellar kinematics in ULIRGs and QSOs.

2

Pre-coalescence ultraluminous merger phases

...or... Dynamical properties of ULIRGs I: Mass ratio conditions for ULIRG activity in interacting pairs

K. M. Dasyra, L. J. Tacconi, R. I. Davies, R. Genzel, D. Lutz, T. Naab, A. Burkert, S. Veilleux, & D. B. Sanders 2006, ApJ, 638, 745

Abstract

We present first results from our Very Large Telescope large program to study the dynamical evolution of Ultraluminous Infrared Galaxies, which are the products of mergers of gas-rich galaxies. The full data set consists of high resolution, long-slit, H- and K-band spectra of 38 ULIRGs and 12 QSOs (between $0.042< z <0.268$). In this paper, we present the sources that have not fully coalesced, and therefore have two distinct nuclei. This sub-sample consists of 21 ULIRGs, the nuclear separation of which varies between 1.6 and 23.3 kpc. From the CO bandheads that appear in our spectra, we extract the stellar velocity dispersion, σ, and the rotational velocity, $V_{\rm rot}$. The stellar dispersion equals 142km s^{-1} on average, while $V_{\rm rot}$ is often of the same order. We combine our spectroscopic results with high-resolution infrared imaging data to study the conditions for ULIRG activity in interacting pairs. We find that the majority of ULIRGs are triggered by almost equal-mass major mergers of 1.5:1 average ratio. Less frequently, 3:1 encounters are also observed in our sample. However, less violent mergers of mass

ratio >3:1 typically do not force enough gas into the center to generate ULIRG luminosities.

2.1 Introduction

In hierarchical cold dark matter models of galaxy formation and evolution, galaxy merging may lead to the formation of elliptical galaxies, trigger major starbursts, and account for the formation of supermassive black holes and quasars (e.g. Efstathiou & Rees 1988; Kauffmann & Haehnelt 2000; Haehnelt 2004). Despite the importance and prevalence of galaxy mergers in driving galaxy evolution, the physical details of the merging process are not yet well-understood even in the local Universe.

Mergers are responsible for producing some of the most luminous objects of the local Universe, the ultraluminous infrared galaxies. The bolometric luminosities of ULIRGs are greater than $10^{12} L_{\odot}$ and emerge mainly in the far-infrared (FIR). ULIRGs are mergers of gas-rich, disk galaxies and have large molecular gas concentrations in their central kpc regions (e.g. Downes & Solomon 1998; Bryant & Scoville 1999) with gas-mass densities comparable to stellar densities in ellipticals.

The ULIRG phase occurs in mergers after the first peri-passage (e.g. Sanders & Mirabel 1996, Veilleux, Kim & Sanders 2002) to post-coalescence. The nuclear separation, the presence of tidal tails and the high IR luminosities of these sources are all indications that ULIRG mergers are in a phase beyond the first approach of the halos (e.g. Veilleux, Kim & Sanders, 2002). These observations are consistent with the results from a plethora of numerical models in the literature (e.g. Mihos 1999; Mihos & Hernquist 1996; Springel et al. 2005), which indicate that starbursts intense enough to drive a ULIRG phase occur only after the first encounter and can be present after the nuclear coalescence, before complete relaxation sets in.

A quantitative observational technique to investigate galaxy merger evolution is to determine the kinematic and structural properties of their hosts at different merger timescales. With that goal in mind we have conducted a European Southern Observatory large program[1], where we performed high-resolution near-infrared spectroscopy of a large sample of ULIRGs spanning a wide range of merger phase and infrared luminosity. This work expands on the previous spectroscopic studies of Genzel et al. (2001) and Tacconi et al. (2002).

In this paper we focus on binary ULIRG sources; these systems are between the first and final encounter phases of a merger, thus they still have (at least)

[1] 171.B-0442 (PI Tacconi)

two well-separated nuclei. We investigate the mass ratios of the galaxies that, when merging, produce ULIRG-like luminosities. The results from the remnants, the sources which have coalesced and show a single nucleus in the NIR images, will be presented in a forthcoming paper, together with the evolution of the host dynamics and the black hole mass during the merger.

This paper is arranged as follows. After summarizing the observations and describing the data reduction method in § 2.2, we extract structural parameters of our sources in § 2.3. The stellar kinematics of the merging hosts, as derived from our long-slit spectra are presented in § 2.4. Using the kinematics, we calculate the progenitor mass ratio of the merging galaxies in § 2.5. To ensure that the observed mass ratio is not severely affected by the dynamical heating of the system or projection effects, we perform simulations that predict the time evolution of the mass ratio in § 2.6. An overview of our results is presented in § 2.7.

2.2 Observations and Data Reduction

We present near-infrared Very Large Telescope spectroscopic data of local mergers. In the current study, 21 ULIRGs are presented, 20 of which are binary systems and 1 of which, IRAS 00199-7426, may be a multiple merger (Duc et al. 1997; also see Appendix A). To these sources, we add 3 binary ULIRGs that have already been presented in Genzel et al. (2001). With the presentation of the spectroscopy of 23 binary sources in total, we complete the part of our sample that deals with sources in a merger state prior to the coalescence of the individual nuclei.

The entire sample consists of 38 sources and it is largely drawn from the combined 1 Jy catalog (Kim & Sanders 1998), and the southern-ULIRG (SULIRG) sample of the Duc et al. (1997) study. One source, IRAS 02364-4751, is from Rigopoulou et al. (1999). The sample size increases to 54 ULIRGs when the sources studied in Genzel et al. (2001) and Tacconi et al. (2002) are included. The 1 Jy catalog comprises a complete flux-limited (at 60 μm) sample of 118 ULIRGs compiled from a redshift survey of IRAS Faint Source Catalog version 2 objects (Moshir et al. 1990). Veilleux et al. (2002) have completed and analyzed an R- and K-band survey of the entire catalog, such that photometric and structural data (absolute magnitudes, surface brightnesses, half-light radii) are readily available. We have observed those sources with dec $< 25°$, and with redshifts where the strong rest frame H-band stellar absorption lines lie in parts of the H- and K-band with high atmospheric transmission ($z \leq 0.11$ and $z \geq 0.20$).

The left-panel histogram of Fig. 2.1 shows that the sources we selected from

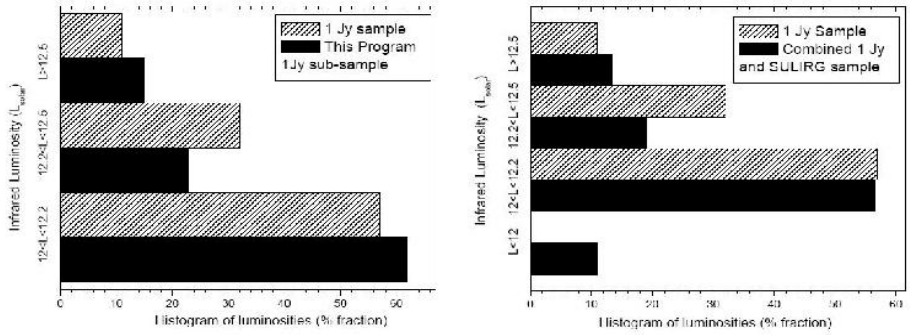

Figure 2.1: Histogram of luminosities of samples used in this study. Sources from the 1 Jy catalog (Kim et al. 2002) are denoted by the hatched bars. In the left panel, the sources we selected from the 1 Jy catalog are shown as filled bars and follow well the original sample's luminosity distribution. In the right panel, the mean luminosity of the combined samples is reduced due to the addition of the lower-luminosity Duc et al. (1997) sample.

the 1 Jy catalog follow a similar luminosity distribution as the entire catalog. Given that the latter is solely compiled according to the 60 μm flux, it does not favor any particular pre-merger initial conditions. When adding sources from the Duc et al. (1997) catalog, which contains less luminous sources than the 1 Jy sample (see right panel of Fig. 2.1), the average IR luminosity of our sample is reduced, but remains luminosity-selected. For the sources of the Duc et al. (1997) sample, we do not adopt the $L_{\rm IR}$ values of the authors, but we use the Sanders & Mirabel (1996) expression and the Faint Source Catalog version 2 mid-infrared (MIR) and FIR fluxes to calculate $L_{\rm IR}$. Two of the sources in our large program sample are less luminous than $10^{12} L_{\odot}$, however we also treat them as ULIRGs given that the classification often depends on the accuracy of the mid- and far-infrared flux measurements.

Our data were taken with the VLT ANTU telescope on Cerro Paranal, Chile. We used the ISAAC spectrometer (Moorwood et al. 1998) in mid-resolution mode in the H band ($\lambda/\delta\lambda = 5100$), and in the K band ($\lambda/\delta\lambda = 4400$), with a slit width of $0.6''$. The on-chip integration was 600 s per frame with typical total integration times of 1 hr per slit position angle (see Table 2.1). For most of the binary sources we observed along three slits, with the first slit going through both nuclei. The other two slits are (usually) perpendicular to the first one and go through the brighter and the fainter nucleus respectively.

Table 2.1: Binary ULIRGs source list

Galaxy (IRAS)	RA (2000)	Dec (2000)	z	$\log(L_{\rm IR}/{\rm L}_\odot)$	slit P.A. ($^\circ$)	$t_{\rm integration}$ (mins)
00199-7426 [a]	00:22:07.0	-74:09:42	0.096	12.23	-15,75,74	60,60,60
01166-0844	01:19:07.6	-08:29:10	0.118	12.03	-60,29,29	60,60,60
02364-4751	02:38:13.1	-47:38:11	0.098	12.10	0,90	60,50
06035-7102	06:02:54.0	-71:03:10	0.0795	12.12	65,153,153	60,50,60
10190+1322	10:21:42	13:07:01	0.077	12.00	64,149,149	40,40,40
10565+2448	10:59:18.1	24:32:34	0.0431	12.02	-66,24	40,40
11095-0238	11:12:03	-02:54:18	0.106	12.20	39,129	120,120
12071-0444	12:09:45.1	-05:01:14	0.128	12.35	-1,89	60,60
12112+0305	12:13:47	02:48:34	0.073	12.28	37,99	60,60,40
13335-2612	13:36:22	-26:27:31	0.125	12.06	-5	100
13451+1232	13:47:33	12:17:23	0.122	12.28	104,13	80,120
16156+0146	16:18:08	01:39:21	0.132	12.04	-50,-51,40,40	60,60,60,60
16300+1558	16:32:20	15:51:49	0.242	12.63	-1,89	150,90
19254-7245	19:31:21.4	-72:39:18	0.0617	12.00	-13,77	60,60
20046-0623	20:07:19.3	-06:14:26	0.0844	11.97	69,159	60,60
21130-4446	21:16:18.5	-44:33:38	0.0926	12.02	33	40
21208-0519	21:23:29	-05:06:59	0.13	12.01	-164,109,109	60,60,60
21329-2346	21:35:45	-23:32:36	0.125	12.09	31	60
22491-1808	22:51:49.2	-17:52:23	0.0778	12.09	-76,13,13	60,60,60
23128-5919	23:15:46.8	-59:03:15	0.045	11.96	-5,84,84	40,40,40
23234+0946	23:25:56.2	10:02:50	0.128	12.05	-64,25	60,60

The coordinates, the redshift, the bolometric luminosity, as well as the slit positions and the respective integration time for our source list are presented in this Table.
[a] This source may be a multiple merger (see the Appendix).

We have selected the central wavelength in a way such that most of the CO(3-0), CO(4-1), SiI, CO(5-2), and CO(6-3) H-band bandheads (at 1.558, 1.578, 1.589, 1.598, and 1.619 μm respectively), as well as the forbidden [FeII] emission line (at 1.645 μm), appear in our spectra. For the sources with redshift $z > 0.2$ we use (some of) the CO(8-5), CO(9-6), and CO(10-7) absorption bandheads (at 1.661, 1.684, and 1.706 μm respectively), which are then shifted to the K band. The CO and SiI absorption features trace the stellar, while the Fe emission line traces the warm gas kinematics. The observed central wavelength range varied from 1.68 to 2.08 μm, depending on the redshift of each source (Table 2.1). The most nearby of the objects presented in this study is at redshift $z = 0.0431$ while the most distant at $z = 0.242$.

For the data reduction we used standard IRAF routines. We first subtracted the frames of positive from the frames of negative chop throw (offset from the telescope pointing position) for the sky background removal, and flat-fielded the result. Then, we performed a bad-pixel and cosmic-ray removal, and corrected for detector deformations. For the spatial direction, we combined several spectroscopic frames of a point-like source (star) at a different chop throw and nod (random offset, smaller than the chop throw). By fitting all the stellar traces, we found the low-order polynomial that best corrects for deformations of the spatial axis. For the spectral axis we used a "sky" frame, which simply was a randomly selected, dark-subtracted frame of our exposures. We found the best wavelength correction matrix by identifying the sky-lines in that frame, and, again, by fitting a polynomial to them. After rectifying the images in both the spatial and wavelength directions, we spatially shifted the frames so that their traces overlap and, then, we combined them. The spectral extraction from the final frame was followed by an atmospheric correction with the aid of a telluric (usually B dwarf or solar type) star. The spectral extraction procedure was repeated for several apertures along each slit, and for two different slit position angles, so that the two dimensional image of the stellar kinematics could be reconstructed. The final spectra were shifted to restframe.

To extract the velocity dispersion σ and rotational velocity $V_{\rm rot}$ we correlated the source spectra with that of an appropriate template star. Due to the starburst nature of a ULIRG, the stellar population that dominates the near infrared (NIR) light is either a giant or a supergiant (or a combination of the two). For this purpose we selected either HD 25472 or HD 99817 (M0III giant and M1I supergiant respectively). We used the Fourier correlation quotient (FCQ) technique described in Bender (1990) with a Wiener filter to suppress the high-frequency noise; for this we used a code written by one of us. The FCQ technique is based on the deconvolution of the correlation function peaks of the source and the stellar template to the autocorrelation function peaks

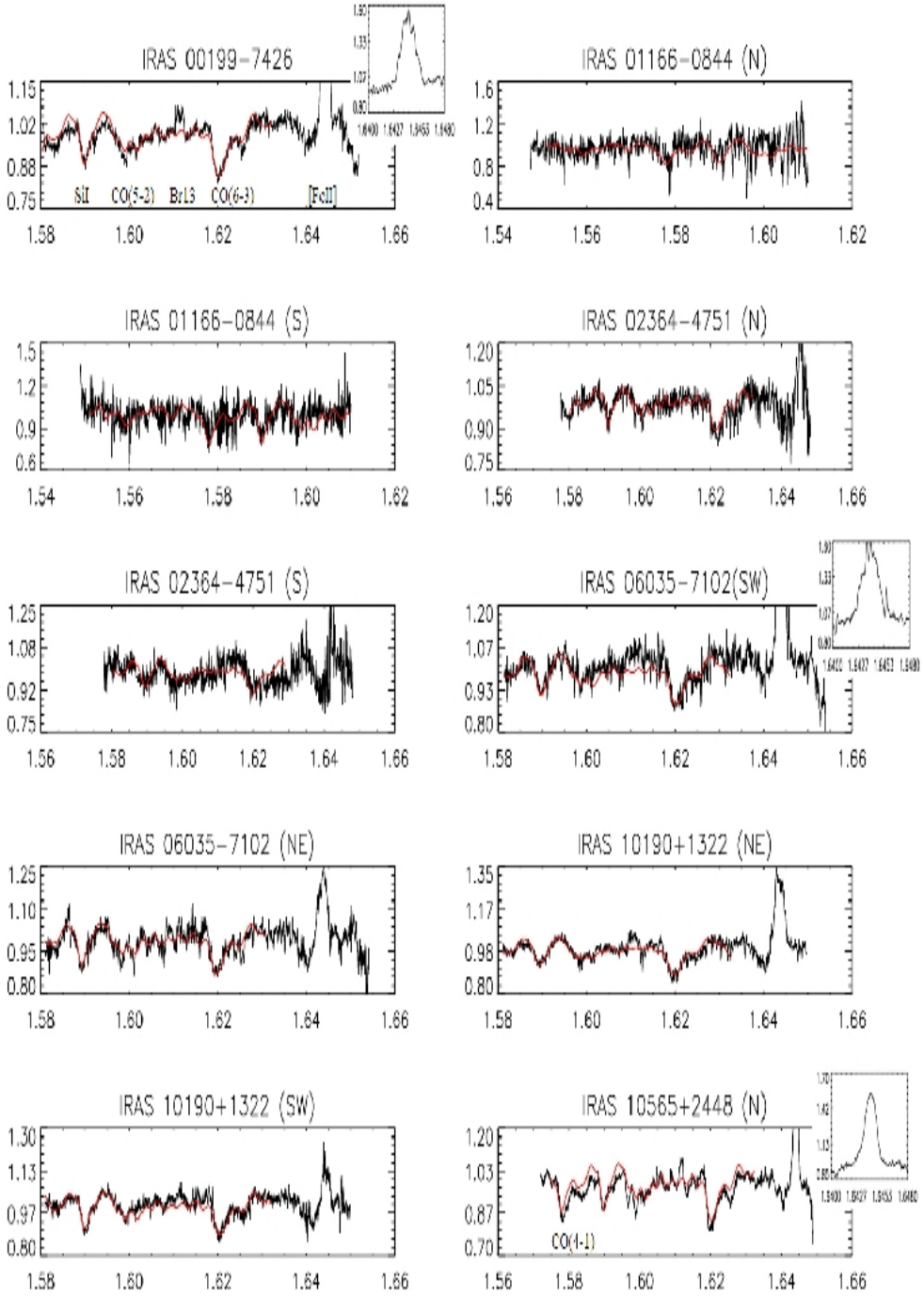

Figure 2.2: The reduced H-band spectra of the binary ULIRGs. The stellar templates, convolved with a Gaussian that represents their LOS broadening function, are overplotted in solid line. All the spectra are shifted to rest frame.

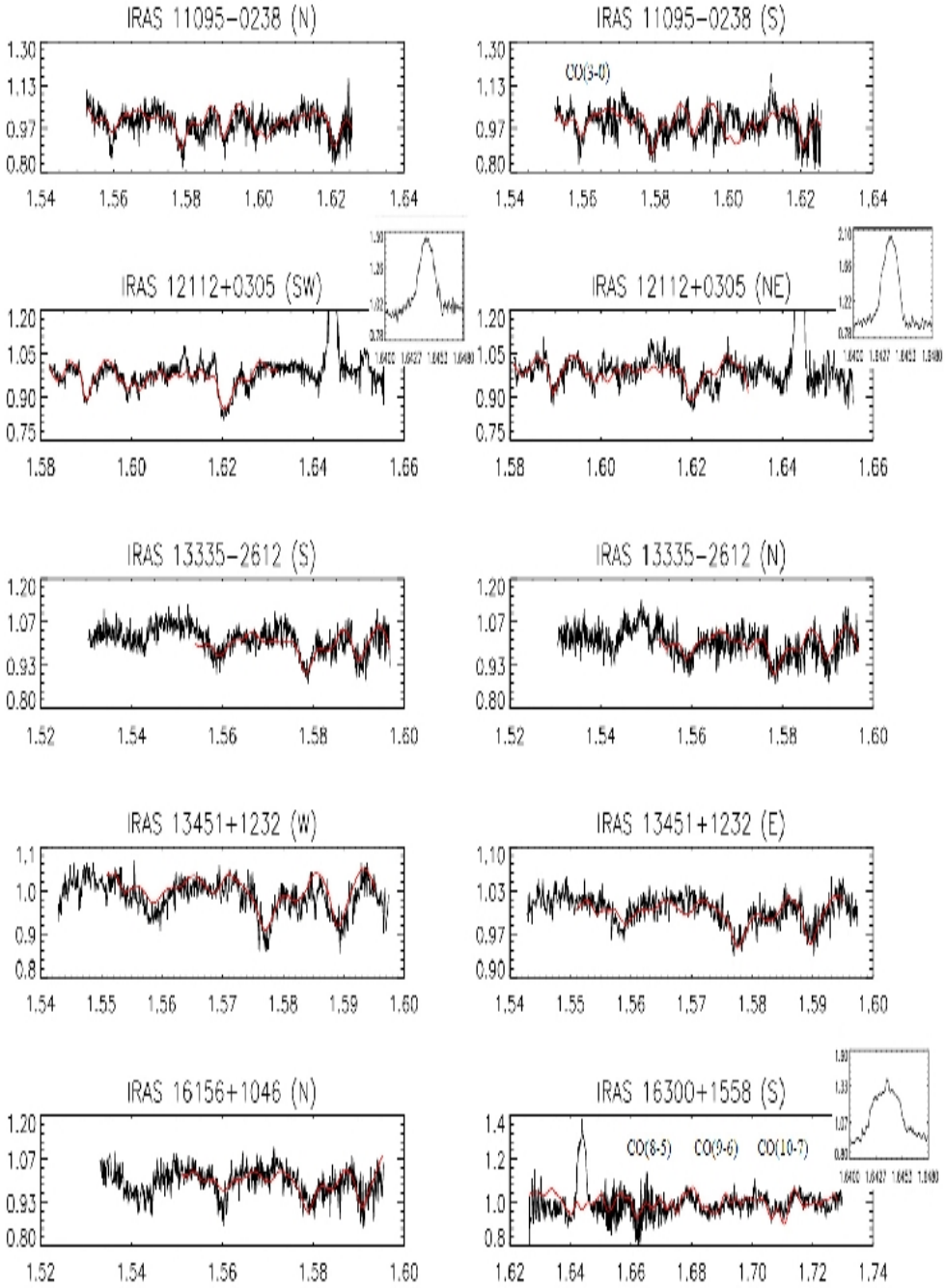

Fig. 2.2 continued.

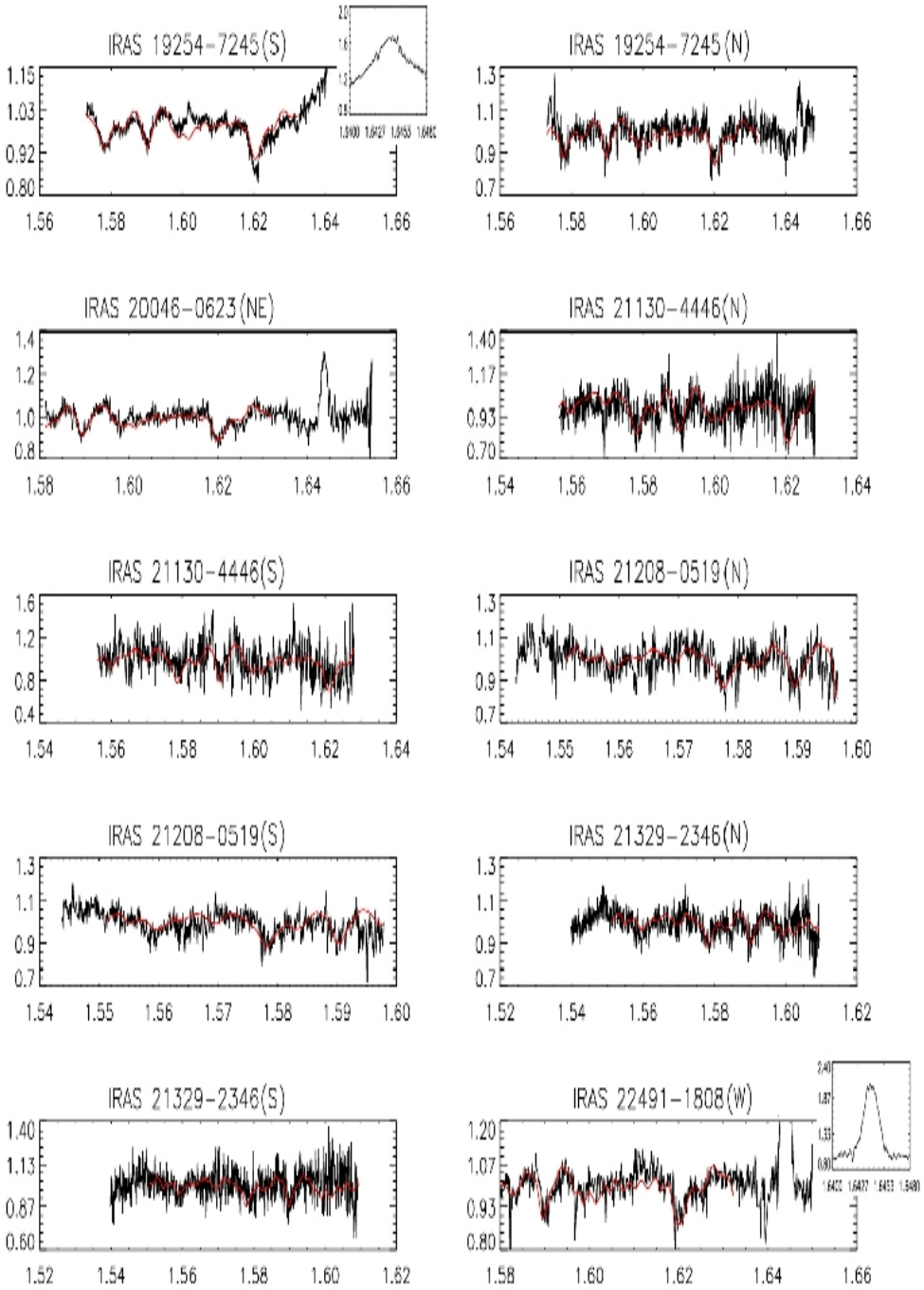

Fig. 2.2 continued.

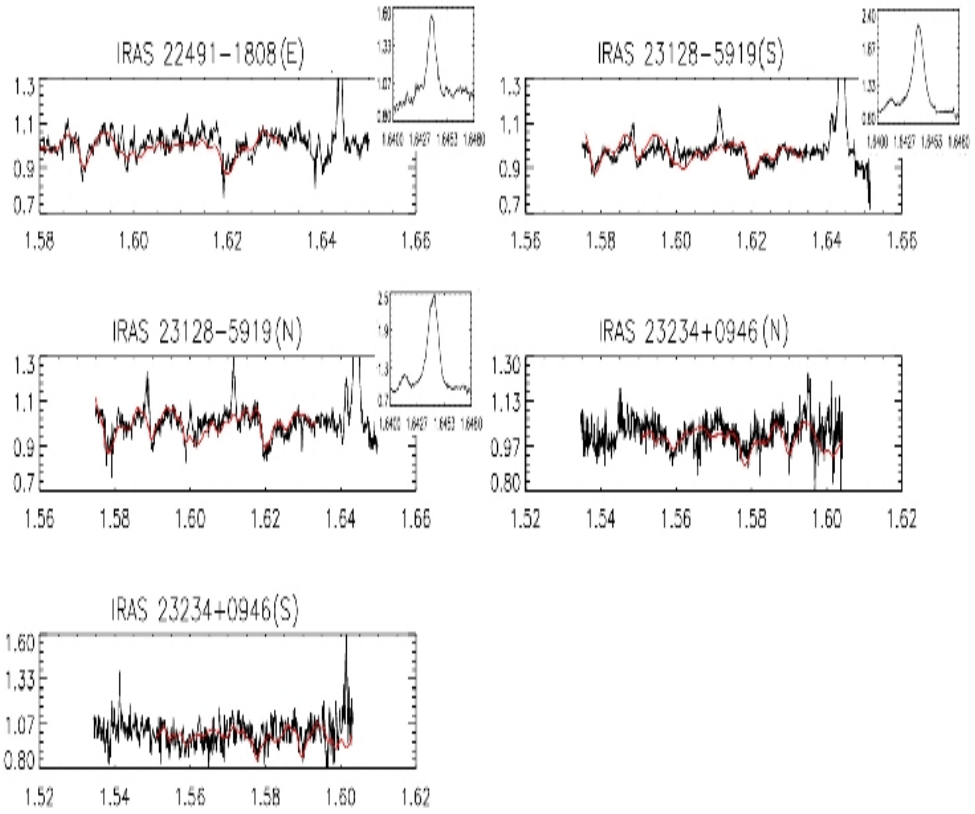

Fig. 2.2 continued.

of the template. It provides the broadening function along the line-of-sight (LOS) of the observations. We fit a high-order Gaussian (linear combination of Gaussian and second order polynomial) to the broadening function in order to derive the stellar dispersion and the recession velocity, $V_{\rm rec}$. For this purpose, we use all of the above-mentioned H-band bandheads that exist in our spectra, as long as the signal-to-noise allows us to do so, and we average the results. From the difference in the recession velocity along several apertures of the slit, we calculate the rotational velocity on the plane defined by the line-of-sight and the position angle of the slit.

We follow the above procedure to extract the spectra for each source (or nucleus). The central aperture spectra, combined over the slits and shifted to the restframe, are displayed in Fig. 2.2. In each panel, the stellar template is overplotted with a solid line, after being convolved with the Gaussian that best fits the respective LOS broadening function.

2.3 Structural parameters

The conversion of our dynamical measurements into masses requires complementary data that trace the structure of our sources, namely the half-light-radius $R_{\rm eff}$ and the inclination to the line of sight, i.

Given that ULIRGs originate from the merger of gas-rich disk galaxies, we use the (dynamically perturbed) progenitor disks to estimate the inclination. The rotational velocity of a disk is connected to its line of sight dependent value, $V_{\rm LOS}$ as follows

$$V_{\rm rot} = V_{\rm LOS}/(cos(\phi_\alpha)sin(i)). \tag{2.1}$$

The parameter ϕ_α is the angle between the slit position angle and the major axis of the inclined disk (which is an ellipsoid when projected in 2 dimensions).

We derive the structural parameters i and ϕ_α for the stellar disk of each ULIRG by fitting ellipses to the H-band acquisition images (see Fig. 2.3). The fit is performed with the aid of the SExtractor package (Bertin & Arnouts 1996), made available by the Institut d'Astrophysique de Paris. We first detect the center and the radial extent of each source by setting a threshold that separates the sky background from any real detection. We then deblend sources that spatially overlap to obtain the apparent ellipticity ϵ, the angle ϕ_α (which appear in Table 2.2), and the enclosed counts of each ellipsoid.

The apparent ellipticity is related with the inclination i of the heated stellar disk as

$$\epsilon(2-\epsilon) = \epsilon_t(2-\epsilon_t)(sini)^2 \tag{2.2}$$

(Binney & Tremaine 1987; Chapter 4.3). The quantity ϵ_t is the (true) ellipticity of the heated disk when seen edge-on. We assume that the ratio of the thickness to the truncation radius is 0.3 for the binary ULIRGs, which is the average value between field spirals and disky ellipticals (Binney & de Vaucouleurs 1981). In this case ϵ_t equals 0.7. The inclinations calculated with this method are presented in Table 2.2 and have a mean value of 43°. We note that when using the flat disk approximation ($\epsilon_t = 1$) the mean inclination of this sample is 40°. Solving and differentiating Eq. [2.2] for i shows that the smaller the inclination, the greater the error on its measured value for a given ϵ. The systems that are close to face-on are, therefore, those with the most uncertain inclination estimates.

We use the half-light radius as the fiducial aperture in which to calculate masses and luminosities for the progenitor nuclei. However, the half-light radii for most of the individual nuclei of our binary ULIRGs are not readily available in the literature; several binary systems have been treated as a single object (e.g. Veilleux et al. 2002; Scoville et al. 2000), often due to low angular resolution. When available, the effective radii are not usually measured from NIR data but, from optical bands where the light extinction is significant. Due to the extremely dusty environment of ULIRGS and to inclination effects, average extinction corrections are not always reliable for individual sources. For these reasons, we measure new half-light radii from our H-band acquisition images by fitting ellipsoids to the individual nuclei and finding the radius at which the ellipsoid contains half of the total counts. We tabulate the measured H-band $R_{\rm eff}$ in Table 2.2, after converting angular distances into linear sizes. All distances in this paper are for a H_0=70 km s^{-1} Mpc^{-1}, Ω_m=0.3, $\Omega_{\rm total}$=1 cosmology.

Our results are consistent with those of NIR imaging available in the literature, despite the fact that the acquisition images have short exposure times ($\sim$10 s) and could be tracing only the most luminous parts of the sources, leading to underestimates of the true half-light radius. To check this possible bias, we compare the effective radii for the sources we have in common with Scoville et al. (2000). We find that the effective radii for IRAS 12112+0305 (sw), IRAS 13451+1232 (w), and IRAS 22491-1808 (e) are 0.81, 4.14, and 1.99 kpc while the half-light radii for flux within 3 kpc given by Scoville et al. (2000) (at 1.6 μm) were 0.79, 1.07, and 1.66 kpc respectively. The results for two of the cases are very similar and the disagreement in the case of IRAS 13451+1232(w) is due to aperture effects. IRAS 13451+1232 is one of the most extended sources of the Scoville et al. (2000) sample with a radial extent $>$ 7 kpc. Furthermore, Veilleux et al. (2006) have recently acquired Hubble Space Relescope (HST) NICMOS H-band imaging for several ULIRGs of the 1 Jy catalog and have performed a two-dimensional decomposition of

the AGN point spread function (PSF) and the host. The effective radii measured from our acquisition images are in good agreement with those of the PSF-subtracted hosts of Veilleux et al. (2006, in preparation).

The structure of a merger, and in particular the nuclear separation, can be used to trace the timescales of each merging system (e.g. Barnes 2001). The majority of the pre-merged ULIRGs have intrinsic nuclear separation smaller than 10 kpc (see Table 2.2), a fact that classifies them as pre-merger close binaries according to the Surace et al. (1998) scheme. Only five of our galaxies, IRAS 01166-0844, IRAS 06035-7102, IRAS 10565+2448, IRAS 19254-7245, and IRAS 21208-0519 are considered wide binaries in the same classification scheme. The mean projected nuclear separation of our sample is 7.3 kpc (and the median 5.4 kpc).

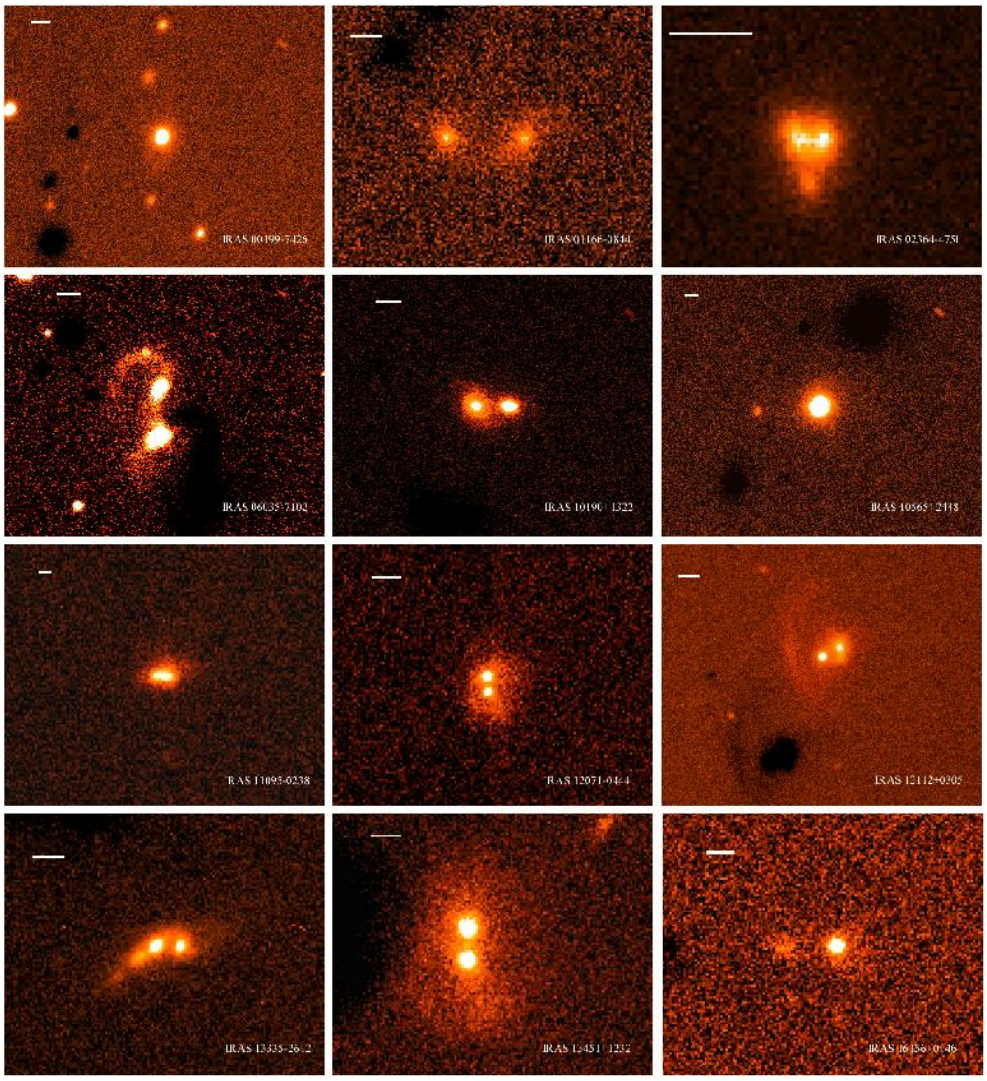

Figure 2.3: The (raw) H-band acquisition images. The horizontal line in the upper left corner of each panel corresponds to 5 kpc at the reshift of the source.

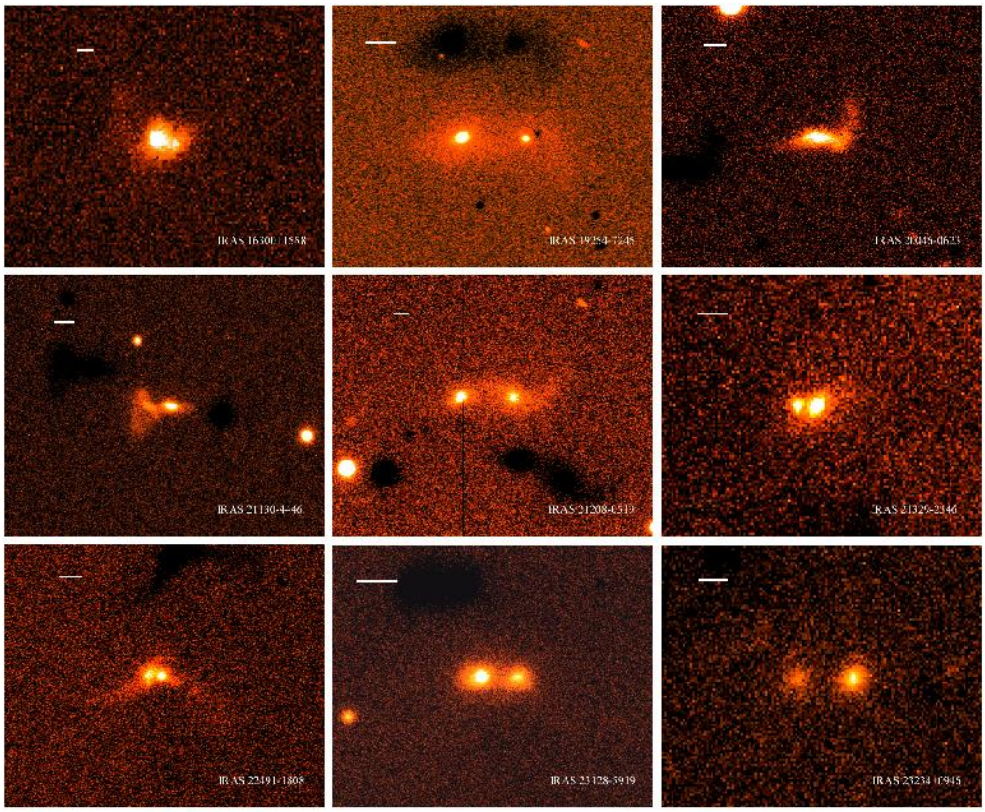

Fig. 2.3 continued.

Table 2.2: The structural parameters of the ULIRGs of this sample.

Galaxy IRAS	$R_{\rm eff}$ (kpc)	ellipticity (-)	inclination (°)	ϕ_α (°)	nuclear separation (kpc)
00199-7426	0.88 (±0.04)	0.115	29	18	...
01166-0844(s)	1.72 (±1.23)	0.177	37	-10	12.2 (±0.3)
01166-0844(n)	1.55 (±0.98)	0.178	37	61	...
02364-4751(s)	1.45 (±0.21)	0.250	44	52	1.6 (±0.3)
02364-4751(n)	1.18 (±0.14)	0.217	41	-78	...
06035-7102(sw)	1.79 (±0.51)	0.331	51	39	10.4 (±0.2)
06035-7102(ne)	1.41 (±0.13)	0.398	57	34	...
10190+1322(ne)	1.43 (±0.06)	0.298	48	6	6.5 (±0.2)
10190+1322(sw)	2.40 (±0.14)	0.223	41	37	...
10565+2448(s)	0.79 (±0.01)	0.042	17	-84	23.3 (±0.1)
10565+2448(n)	0.73 (±0.10)	0.125	30	72	...
11095-0238(ne)	2.07 (±0.90)	0.151	34	27	3.8 (±0.3)
11095-0238(sw)	3.04 (±1.20)	0.398	57	-22	...
12071-0444(s)	2.32 (±1.05)	0.095	26	-68	2.8 (±0.4)
12071-0444(n)	2.09 (±0.70)	0.083	25	71	...
12112+0305(sw)	0.81 (±0.01)	0.048	19	53	4.5 (±0.2)
12112+0305(ne)	1.67 (±0.29)	0.413	58	12	...
13335-2612(s)	2.88 (±0.17)	0.598	74	-34	3.9 (±0.4)
13335-2612(n)	2.25 (±0.08)	0.098	27	-55	...
13451+1232(w)	2.59 (±0.58)	0.094	26	-1	5.3 (±0.3)
13451+1232(e)	4.14 (±2.16)	0.168	36	-3	...
16156+0146(n)	0.90 (±0.10)	0.128	31	89	8.8 (±1.2)
16156+0146(s)	2.01 (±0.12)	0.626	76	1	...
16300+1558(s)	2.76 (±1.37)	0.227	42	-67	5.6 (±0.8)
16300+1558(n)	4.83 (±2.06)	0.351	53	-14	...
19254-7245(s)	0.97 (±0.78)	0.288	47	-21	10.2 (±0.2)
19254-7245(n)	0.70 (±0.35)	0.091	26	12	...
20046-0623(w)	2.67 (±0.19)	0.673	82	6	<4.4
20046-0623(e)	...	...	...	...	...
21130-4446(ne)	1.71 (±0.13)	0.398	57	8	5.4 ±0.3)
21130-4446(sw)	2.69 (±0.61)	0.584	72	32	...
21208-0519(s)	3.66 (±1.06)	0.139	32	21	17.9 (±0.4)
21208-0519(n)	2.34 (±0.67)	0.257	45	-33	...
21329-2346(n)	1.70 (±0.12)	0.312	50	-46	3.1 (±0.4)
21329-2346(s)	1.42 (±0.08)	0.128	31	-88	...
22491-1808(e)	1.99 (±0.04)	0.370	54	-62	3.3 (±0.2)
22491-1808(w)	1.77 (±0.10)	0.088	25	44	...
23128-5919(n)	4.20 (±0.08)	0.244	43	-11	4.3 (±0.1)
23128-5919(s)	4.16 (±0.03)	0.296	48	-7	...
23234+0946(n)	2.12 (±0.32)	0.154	34	-32	9.4 (±0.4)
23234+0946(s)	3.28 (±1.42)	0.116	29	-58	...

The ULIRG structural parameters are derived from the acquisition images. For each system, the nuclear separation is given once and the nucleus with the most massive bulge appears first.

2.4 ULIRG stellar velocities and black hole masses

The stellar dispersions extracted (according to the prescriptions of § 2.2) by the Fourier quotient technique from the central-aperture spectrum of each source are listed in Table 2.3. In the fainter sources, σ may be somewhat overestimated (at most by 20%) due to low signal-to-noise ratio, which can mimic broader dispersions. The stellar velocity dispersion may vary when measured from different bandheads (typically by 15%). This is both due to a possible template mismatch and to the sky-line contamination of our spectra. The velocity error bars are equal to the standard deviation of the measurements performed at the individual bandheads.

The mean observed dispersion of our binary ULIRG sample, combined with the sources in Genzel et al. (2001), is 142 km s^{-1} (with a standard deviation of 21 km s^{-1}). Sources of intrinsic nuclear separation close to or less than 1 kpc (Arp 220 and NGC 6240, see Genzel et al. 2001, Tecza et al. 2000) were removed from the above statistics. By the time the nuclei of two merging galaxies are separated by $\lesssim$ 1 kpc, the stellar velocities have almost reached their final relaxation values (Genzel et al. 2001, Mihos 2000, Bendo & Barnes 2000). As a consequence, these systems have dispersions very close to their (common) equilibrium value and resemble more the coalesced ULIRGs, despite the fact that their nuclei can still be resolved.

We measure the rotational velocity along each slit and we correct it for the angular deviation ϕ_α from the major axis of rotation as discussed in § 2.2. After averaging the results over the slits, we obtain the observed rotational velocity, $V_{\rm rot}(obs)$, which we display in Table 2.3 together with its error bar (calculated similarly to that of σ). In the same Table we also present the final, inclination corrected rotational velocity $V_{\rm rot}$.

The ratio of the observed rotational velocity to the dispersion, $V_{\rm rot}({\rm obs})/\sigma$, is given in Table 2.3 for each source. The mean $V_{\rm rot}({\rm obs})/\sigma$ ratio for the sample presented in this study is 0.42, while when using the inclination corrected velocity, the ratio $V_{\rm rot}/\sigma$ increases to 0.77. Both values are low compared to those of spiral galaxies. We now investigate whether this result is due to the violent relaxation process or due to systematics, such as beam-smearing effects. To check for beam smearing we calculate the $V_{\rm rot}/\sigma$ ratio for the sources for which we have been able to derive rotation curves (due to their large radial extent). These are the sources with z<0.07 as well as IRAS 20046-0623. We find that the $V_{\rm rot}/\sigma$ ratio for these sources is similar to that of our entire sample: 0.58 and 1.16 when using the inclined-disk and inclination-corrected velocities, respectively. We conclude that the low rotational velocitites observed in the binary ULIRGs is due to the actual dynamical heating of the merging systems. Similar conclusions are drawn from the work of Mihos

(2000), who presents simulations of the velocity moments during the merger process. The $V_{\rm rot}$(obs)/σ ratio implied from Mihos (2000) for our median nuclear separation (5 kpc) and for the radius containing 50% of the stellar mass (or the $R_{\rm eff}$ for constant M/L within the galaxy) is also ∼0.4.

Using the stellar dispersions listed in Table 2.3, we estimate a BH mass, M_{BH}, with the aid of the $M_{BH} - \sigma$ relation (e.g. Gebhardt et al. 2001; Ferrarese & Merritt 2001). The published estimates for the slope of the $M_{\rm BH} - \sigma$ relation span a significant range (see Tremaine et al. 2002; Gebhardt et al. 2001; Merritt & Ferrarese 2001). We use the Tremaine et al. (2002) expression $M_{BH} = 1.35 \times 10^8 (\sigma/200)^{4.02} M_\odot$ which lies between those of Gebhardt et al. (2001) and Merritt & Ferrarese (2001). We present the BH mass calculated for each source in Table 2.3. The mean black hole mass of the binary ULIRG sample is an order of magnitude greater than that of the Milky Way and equals 3.9×10^7 $M_\odot$ (for each nucleus). Converting the stellar dispersions into black hole masses carries the uncertainty of applying the $M_{\rm BH} - \sigma$ relation to systems that are not in dynamical equilibrium. The errors introduced by this conversion and the conditions under which the $M_{\rm BH} - \sigma$ relation may provide an accurate estimate of $M_{\rm BH}$ during a merger will be presented in a forthcoming paper (Dasyra et al. 2006, in preparation).

In Table 2.3 we present the (minimum) black hole mass that each source would have, if it were accreting at the Eddington rate ($L_{\rm Eddington}/L_\odot = 3.8 \times 10^4 M_{BH}$(Eddington)/$M_\odot$). We assign to the Eddington luminosity $L_{\rm Eddington}$ half of that emitted in the IR (Genzel et al. 1998; Sanders & Mirabel 1996). This is a statistically plausible assumption based on the fact that some ULIRGs are largely AGN- while others are starburst- powered (see Genzel et al. 1998; Duc et al. 1997; Lutz et al. 1999). However, for individual sources, the numbers given in Table 2.3 may be higher up to a factor 2 or much lower. We assign the luminosity to each nucleus according to the K-band luminosity ratios (Kim et al. 2002; Duc et al. 1997), under the assumption that both progenitors have a BH. To distribute the luminosity between the two nuclei of IRAS 12071-0444 and IRAS 21329-2346 we used the H-band count ratios (1.23 and 2.17 respectively; also see the Appendix) since no photometric information on individual nuclei was available in the literature. For the sources of apparent nuclear separation $< 0.7''$ we distributed 50% of the luminosity to each nucleus, since we used pixel masking (that affects the number counts) to deblend the progenitors. The ratio of the Eddington to the dynamical BH mass, the Eddington efficiency $\eta_{\rm Edd}$, is given in the last column of Table 2.3. On average, it is 0.34 for the individual nuclei, which implies that at the pre-merger phase the accretion onto the BH is lower than the Eddington limit.

Table 2.3: Stellar velocities and resulting black hole masses.

IRAS source	σ (km s^{-1})	$V_{\rm rot}$(obs) [a] (km s^{-1})	$V_{\rm rot}$ [b] (km s^{-1})	$V_{\rm rot}$(obs)/σ	$M_{\rm BH}$ ($M_\odot$)	$M_{\rm BH}$(Edd.) ($M_\odot$)	$\eta_{\rm Edd}$
00199-7426	137 (± 55)	30 (± 13)	76	0.22	2.95×10^7	2.23×10^7	0.76
01166-0844(s)	156 (± 61)	...	...	...	4.97×10^7	7.31×10^6	0.48
01166-0844(n)	116 (± 58)	...	...	...	1.51×10^7	6.79×10^6	0.14
02364-4751(s)	151 (± 32)	...	...	...	4.36×10^7	8.28×10^6	0.19
02364-4751(n)	100 (± 32)	...	...	...	8.32×10^6	8.28×10^6	0.96
06035-7102(sw)	136 (± 24)	41 (± 13)	52	0.30	2.86×10^7	5.61×10^6	0.20
06035-7102(ne)	125 (± 16)	14 (± 15)	17	0.11	2.04×10^7	1.17×10^7	0.57
10190+1322(ne)	169 (± 35)	107 (± 17)	143	0.63	6.86×10^7	7.69×10^6	0.11
10190+1322(sw)	127 (± 12)	105 (± 42)	159	0.83	2.18×10^7	5.47×10^6	0.25
10565+2448(s)	125 (± 31)	134 (± 23)	446	1.07	2.04×10^7	1.38×10^7	0.68
10565+2448(n)	...	...	...	...	...	...	...
11095-0238(ne)	147 (± 32)	...	...	...	3.92×10^7	1.04×10^7	0.27
11095-0238(sw)	137 (± 38)	...	...	...	2.95×10^7	1.04×10^7	0.35
12071-0444(s)	143 (± 36)	...	...	...	3.50×10^7	1.32×10^7	0.38
12071-0444(n)	130 (± 29)	...	...	...	2.39×10^7	1.62×10^7	0.68
12112+0305(sw)	133 (± 10)	34 (± 19)	107	0.26	2.62×10^7	1.53×10^7	0.58
12112+0305(ne)	124 (± 23)	5 (± 18)	6	0.04	1.98×10^7	9.81×10^6	0.50
13335-2612(s)	175 (± 43)	...	...	...	7.89×10^7	8.25×10^6	0.10
13335-2612(n)	140 (± 27)	...	...	...	3.22×10^7	6.86×10^6	0.21
13451+1232(w)	167 (± 48)	...	...	...	6.54×10^7	1.75×10^7	0.27
13451+1232(e)	146 (± 28)	...	...	...	3.81×10^7	7.57×10^6	0.20
16156+0146(n)	189 (± 27)	...	...	...	1.08×10^8	9.22×10^6	0.09
16156+0146(s)	...	...	...	...	...	5.21×10^6	...
16300+1558(s)	141 (± 47)	...	...	...	3.31×10^7	2.81×10^7	0.85
16300+1558(n)	...	...	...	...	...	...	...
19254-7245(s)	175 (± 24)	99 (± 22)	135	0.57	7.89×10^7	9.16×10^6	0.12
19254-7245(n)	120 (± 19)	47 (± 34)	113	0.39	1.73×10^7	4.00×10^6	0.23
20046-0623(w)	145 (± 14)	103 (± 13)	104	0.71	3.71×10^7	1.23×10^7	0.33
20046-0623(e)	...	...	...	...	...	...	...
21130-4446(ne)	165 (± 37)	...	...	...	6.23×10^7	8.48×10^6	0.14
21130-4446(sw)	152 (± 28)	...	...	...	4.48×10^7	5.33×10^6	0.12
21208-0519(s)	171 (± 22)	...	...	...	7.19×10^7	4.28×10^6	0.06
21208-0519(n)	126 (± 21)	...	...	...	2.12×10^7	9.19×10^6	0.44
21329-2346(n)	115 (± 21)	...	...	...	1.46×10^7	1.13×10^7	0.78
21329-2346(s)	113 (± 22)	...	...	...	1.36×10^7	4.86×10^6	0.36
22491-1808(e)	146 (± 20)	16 (± 31)	20	0.11	3.81×10^7	7.02×10^6	0.18
22491-1808(w)	121 (± 34)	27 (± 50)	64	0.23	1.79×10^7	9.17×10^6	0.51
23128-5919(n)	151 (± 21)	29 (± 16)	43	0.20	4.36×10^7	4.13×10^6	0.09
23128-5919(s)	148 (± 18)	82 (± 12)	110	0.56	4.02×10^7	7.87×10^6	0.20
23234+0946(n)	152 (± 23)	...	...	...	4.48×10^7	1.16×10^7	0.26
23234+0946(s)	113 (± 40)	...	...	...	1.36×10^7	3.14×10^6	0.23

The stellar dispersion and rotational velocities, and the $V_{\rm rot}/\sigma$ ratio are derived from the spectra of Fig. 2.2 with the aid of the parameters of Table 2.2. The dynamical and Eddington black hole mass of each nucleus and the ratio of the two are also presented here.

[a] Velocity corrected for deviations from the major axis of rotation.

[b] Observed velocity corrected for inclination effects.

2.5 Progenitor mass ratios

For the binary ULIRGs presented in this study, the stellar kinematics allow us to find the progenitor mass ratios, r_m, using the virial theorem. We assume a King model to relate the observed (LOS) dispersion to the total bulge dispersion. The disk and gas mass are accounted for by adding the contribution of the (inclination corrected) rotational velocity (for the cases where the measurement of $V_{\rm rot}$ is possible). The dynamical mass enclosed within an effective radius is then proportional to

$$M \propto R_{\rm eff}(3\sigma^2 + V_{\rm rot}^2), \tag{2.3}$$

Further factors that take into account the galactic structure are not important here since we are only interested in the mass ratio of the merging systems. We use the values of $V_{\rm rot}$, and σ of Table 2.3, and the half-light radius of Table 2.2.

We present the bulge mass ratio r_m(bulge) (calculated only using the dispersion velocity) and the total baryonic mass ratio r_m (calculated using both σ and $V_{\rm rot}$) in the first two columns of Table 2.4. For both ratios, the mass enclosed within the effective radius of each progenitor was used. The convention we use in this Table is that the total mass ratio r_m is greater than unity. As a consequence, a r_m(bulge) value < 1 means that the more massive galaxy of the pair has the less massive bulge.

For the sources that have a $V_{\rm rot}$ measurement, the mean mass ratio equals to 1.40 when only the bulge is considered, and 1.35 when the stellar disk is added. As a consequence, the difference between using the bulge and the total baryonic ratio is so small that it allows us to safely use the former for the cases where we were not able to extract $V_{\rm rot}$.

The mean progenitor mass ratio derived from Table 2.4 is 1.54, and shows that the majority of the sources we studied are major mergers of 1:1 to 2:1 progenitor mass ratios. As major mergers we denote systems of progenitor mass ratio as high as 3:1; mergers of 4:1 or greater mass ratio are considered minor. Progenitors of apparent nuclear separation less than $0.7''$ overlap on the detector (even though their nuclei are resolved), because they are spatially extended (with an average sample FWHM of 5 pixels). Their measured kinematics depend on the kinematics of their counterparts and, thus, we have decided not to include them in our statistics (IRAS 02364-4751, IRAS 11095-0238). Our result is in agreement with several merger models in the literature (e.g. Mihos & Hernquist 1994; Naab & Burkert 2003) that attribute the ultra-luminous phase to major mergers.

Another indication of the progenitor mass ratio can be drawn from the remnant $V_{\rm rot}$(obs)/σ ratio. Naab & Burkert (2003) performed gas-free, N-

body simulations of binary mergers of several mass ratios and orientations, and found that the major mergers were those that led to slowly rotating remnants. They suggested that the $V_{\rm rot}({\rm obs})/\sigma$ ratio is $\sim$ 0.2 for 1:1 and $\sim$ 0.4 for 2:1 merger remnants, while it reaches higher values (0.8) for minor merger remnants. The $V_{\rm rot}({\rm obs})/\sigma$ ratio for the merged ULIRGs of this study, which will be presented in a future paper (Dasyra et al. 2006, in preparation), is in good agreement with the results of Naab & Burkert (2003) and the more recent simulations of Burkert & Naab (2005).

Further observational evidence for the mass ratio of sources with luminosity cutoff $> 10^{12} L_{\odot}$ comes from the work of Ishida (2004), who calculated the optical (B-band) luminosity ratio of Luminous Infrared Galaxies, sources of $10^{11} L_{\odot} < L_{\rm IR} < 10^{12} L_{\odot}$. Ishida (2004) found a trend of decreasing luminosity ratio with increasing luminosity cutoff. Interacting sources of $L_{\rm IR} < 10^{11.5} L_{\odot}$ were characterized by a wide spread in the optical luminosity ratio. However, the majority ($> 80\%$) of sources of $L_{\rm IR} > 10^{11.5} L_{\odot}$ were strongly interacting (wide binaries with disturbed morphologies, tidal tails or internuclei bridges) or merging pairs with luminosity ratios $<$ 4:1. Since at least a sub-sample of the high-luminosity LIRGs will likely evolve into ULIRGs, the ULIRG luminosity ratios should be expected to have similar (or smaller) luminosity ratios.

On the other hand, we do not exclude the possibility of a minor merger evolving into a ULIRG. IRAS 20046-0623 does show a second nucleus in both the H- and R-band images, which is however too faint to be deblended from the bright source or to be spectroscopically reduced. IRAS 10565+2448, has an H-band luminosity ratio (calculated from the acquisition image) which is consistent with a 5:1 merger. Due to extinction effects, imaging results are not as reliable as spectroscopic ones in the tracing of the system mass, so this 5:1 ratio is only an indication that, even rarely, minor mergers may appear in our sample.

To address whether the luminosity can actually trace the mass of these dusty systems, we compare the luminosity ratio to the mass ratio of our ULIRGs. In the literature, the luminosity ratio is calculated within a specific aperture, equal for both nuclei. To be consistent in our comparison we also need to calculate the baryonic mass ratio inside a given aperture, which we name r_m(aperture). We present the latter ratio and the size of the selected aperture in Table 2.4. The use of a common aperture for both progenitors instead of their effective radii can make the intrinsically fainter nucleus appear brighter than its counterpart (IRAS 06035-7102, IRAS 10190+1322, IRAS 11095-0238, IRAS 21130-4446, IRAS 12112+0305). The area that is used for the calculation of the mass ratio may also significantly change the results.

The R- and K-band luminosity ratios derived from the literature (Kim et

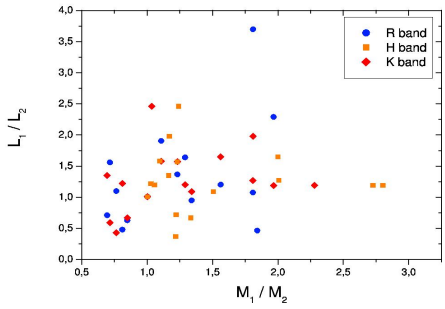

Figure 2.4: Luminosity vs mass ratio of merging systems for R-band (circles), H-band (squares) and K-band (diamonds) data. The data are taken from Kim et al. (2002), Duc et al. (1997), and when not available, our H band images (boxes). This plot shows the discrepancies between the luminosity estimates from different bands and the fact that luminosity does not trace the mass in a robust way.

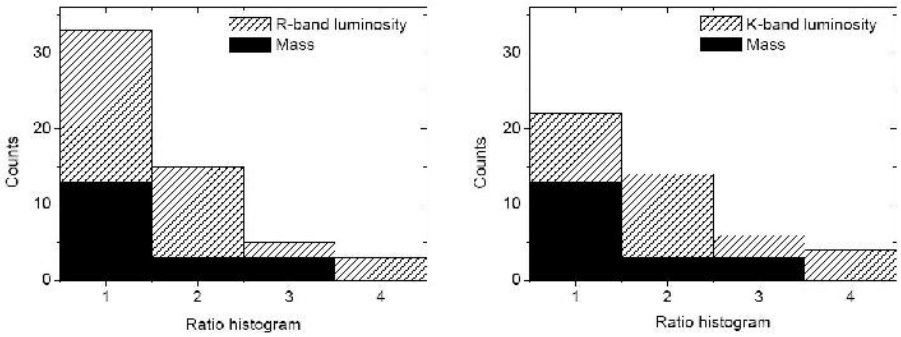

Figure 2.5: Mass and luminosity ratio histogram. In filled bars we show the mass ratio of the ULIRGs in our sample, measured from the stellar kinematics. In shaded we show the R-band (left panel) and the K-band (right panel) luminosity ratio of the combined 1 Jy and Duc et al. (1997) samples.

al. 2002; Scoville et al. 2000; Duc et al 1997) are given in the same Table. The correlation inferred from Fig. 2.4 is rather weak, implying that tracing the mass content of each individual merger by its luminosity can be misleading, due to extinction and population effects. Further support for this argument comes from the fact that, in several cases, the brightest nucleus in the NIR seems to be the faintest in the optical and vice-versa (see the luminosity ratios in Table 2.4). We conclude that the stellar kinematics are the most robust way to determine the mass ratios of merging galaxies.

In Fig. 2.5, we place the binary systems (of luminosity ratio up to 4:1) of the combined samples of Kim et al. (2002) and Duc et al. (1997) in four luminosity ratio bins, for both the R-band (left panel) and the K-band (right panel). The luminosity ratio distribution is different for the two bands due to extinction and population effects. We overplot our sample's mass ratio histogram in filled bars and we find that the distributions are consistent, even though there are deviations in individual cases. This result implies that when the merging galaxies are nearly equal mass (i.e. the 1.5:1 ratio that we find for this sample), individual deviations do not affect the statistical mean.

Table 2.4: Progenitor mass ratios.

Galaxy	r_m(bulge) [a]	r_m [b]	r_m(aperture) [c]	apert. (")	r_L(R band)	r_L(K band)
IRAS 01166-0844	2.01	2.01	1.81	1.18	0.70	1.08
IRAS 02364-4751	2.80	2.80	2.28	1.18	...	...
IRAS 06035-7102	1.07	1.03	0.81	1.47	1.21	0.48
IRAS 10190+1322	0.95	1.16	0.69	1.47	1.74	0.71
IRAS 11095-0238	1.28	1.28	0.87	0.88	...	...
IRAS 12071-0444	1.34	1.34	1.21	1.03	...	...
IRAS 12112+0305	1.48	1.22	0.72	1.47	1.56	0.59
IRAS 13335-2612	2.00	2.00	1.56	1.47	1.03	1.20
IRAS 13451+1232	1.22	1.22	0.76	1.76	1.10	0.43
IRAS 14348-1447	1.05	1.06	1.29	...	1.26	1.64
IRAS 19254-7245	2.94	2.73	1.97	1.18	1.45	2.29
IRAS 21130-4446	1.33	1.33	0.84	1.32	0.76	0.63
IRAS 21208-0519	2.88	2.88	1.84	1.47	1.32	0.47
IRAS 21329-2346	1.24	1.24	1.04	0.88	...	...
IRAS 22491-1808	1.64	1.51	1.34	1.04	1.10	0.95
IRAS 23128-5919	0.95	1.10	1.11	2.35	1.20	1.91
IRAS 23234+0946	1.17	1.17	1.81	1.76	2.38	3.70
arp 220	...	...	1.23	...	...	1.37
NGC 6240	...	...	1.00	...	...	1.01

The total baryonic mass ratio at the half-light-radius, and at a specific aperture (given in the fourth column), the bulge mass ratio and the R and K luminosity ratios of the progenitors can be found in this Table. [a]Bulge mass ratio calculated using the stellar dispersion and the effective radius of each progenitor.
[b]Total mass ratio calculated using the stellar dispersion, rotational velocity (whenever possible), and effective radius of each progenitor.
[c]Total mass ratio calculated within a constant aperture, common for both progenitors.

2.6 A model for the evolution of the mass ratio

We have run simulations of 1:1 and 3:1 mass ratio mergers of disk galaxies containing 10% gas to test whether the mass ratio inferred from observations traces the intrinsic mass ratio of the galaxies and to quantify the influence of tidal effects and disk orientation. The disk galaxies and their orbits were set up in exactly the same way as in Naab & Burkert (2003) (see their Section 2 and Table 1). To include the effects of a dissipative component we replaced 10% of the stellar mass in the initial disks with isothermal gas at a temperature of approximately 10000 K. The initial scale length h of the stellar disk was equal to that of the gas disk. Each galaxy had a stellar bulge with 1/3 of the disk mass and was embedded in a pseudo-isothermal halo to guarantee a flat rotation curve at large radii. The gas disks were represented by 20000 SPH particles (6666 for the low mass disks) other particle numbers are as in Naab & Burkert (2003). All galaxies approached each other on a nearly parabolic orbit with a pericenter distance of two disk scale lengths. The evolution of the stellar and the gas kinematics was computed with the N-body/SPH code VINE using an isothermal equation of state for the gas.

In this paper we analyzed mergers with 16 different initial disk orientations and mass ratios 1:1 and 3:1 (geometries 1-16 in Naab & Burkert 2003, geometries 17-32 for the 3:1 mergers did not change the results presented here). We followed every merger by analyzing snapshots in the orbital plane approximately every half-mass rotation period of the more massive disk. To avoid unrealistic values for $R_{\rm eff}$ when the galaxies overlap, we computed the effective radius of every galaxy as the projected spherical half-mass radius of the stellar particles within 5 scale lengths, taking into account only particles of the galaxy itself. In addition, we computed the projected central stellar velocity dispersion for each galaxy within $0.5R_{\rm eff}$ taking all stellar particles into account. For each merger we have computed the time evolution of the apparent mass ratio as $r_m = r_m(\mathrm{bulge}) = (\sigma_1^2 R_{\rm eff,1})/(\sigma_2^2 R_{\rm eff,2})$, where the indices 1 and 2 declare the most and the least massive progenitor respectively. In Fig. 2.6 we show the apparent mass ratios as a function of distance (in units of disc scale lenghts) for all 1:1 and 3:1 merger remnants.

Equal-mass mergers show apparent mass ratios in the range of $1 < r_m < 1.5$ which are very similar to the true mass ratio, independent of separation. For 3:1 remnants, however, the scatter is larger and the apparent mass ratio is in the range $1.5 < r_m < 4.3$ for distances greater than 10 scale lengths. In particular, there is a trend for r_m to decrease with decreasing distance which is mainly due to tidal heating of the low mass companion and not to a change in $R_{\rm eff}$. At distances below 5 scale lengths, a merger with an intrinsic mass ratio of 3:1 can easily be misclassified as 2:1. Given that the average half-

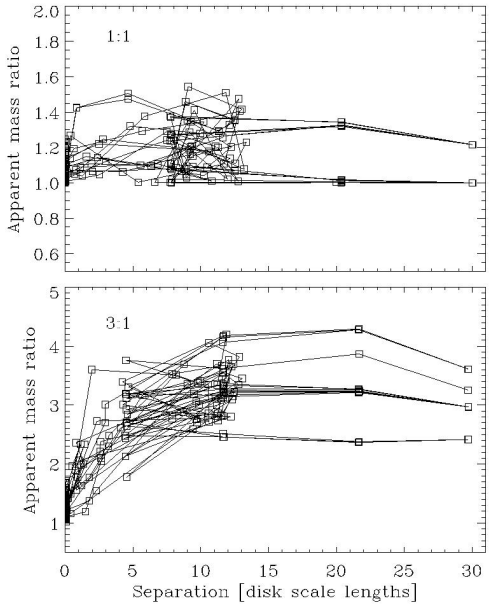

Figure 2.6: Apparent mass ratio measured as $(\sigma_1^2 R_{\rm eff,1})/(\sigma_2^2 R_{\rm eff,2})$ versus distance of simulated merging disk galaxies with a true mass ratio of 1:1 (upper panel) and 3:1 (lower panel). Every line represents one of 16 mergers with different initial disk orientations at a given mass ratio. The squares indicate the measured mass ratios of the ongoing mergers separated in time by a half-mass rotation period of the more massive disk.

light radius of this ULIRG sample is 2.2 kpc (and that $R_{\rm eff} = 1.68h$), 5 disk scale lengths equal 6.6 kpc. More than half of the mergers we observed have a nuclear separation < 6.6 kpc. Thus, the number of unequal-mass mergers that are able to lead to ultraluminous activity may be higher than what is measured. However, given that the majority ($\sim 60\%$) of the sources are almost equal mass mergers, we do not expect the dynamical heating to drastically change our conclusions.

2.7 Conclusions

We have acquired spectroscopic H-band, long-slit data of 21 ULIRGs at a variety of prior to coalescence merger phases to study the mass ratios of the interacting objects that typically trigger ultraluminous activity. Analysis of the kinematics indicates that the mean dispersion of these ULIRGs is 142 km s^{-1} . The dynamical heating that occurs during the merger leads to a low

rotational component of the velocity compared to that of spirals, as the simulations of Mihos (2000) predicted. The mean inclination-corrected $V_{\rm rot}/\sigma$ ratio of this sample is 0.77. The mean mass ratio of the ULIRG progenitors is 1.5:1, which indicates that ULIRGs are mainly the products of almost equal mass mergers. Less frequently, 3:1 mergers appear in our sample. However, our simulations show that the unequal-mass merger categories may be undersampled due to dynamical heating and projection effects. We do not find significant evidence for minor mergers of progenitor mass ratio greater than 4:1; only one source, IRAS 10565+2448, appears as a minor merger in NIR images. However, the luminosity ratio of individual sources may significantly deviate from the actual mass ratio due to extinction and population effects. Using the stellar dynamics is the most robust way to determine the mass content of a ULIRG. On a statistical basis, the mass ratios implied by our kinematical analysis agree with the 1 Jy sample (R-band) luminosity ratios. The major mergers are typically those that are violent enough to drive an adequate amount of gas to the center of the system and trigger ultraluminous infrared bursts.

Acknowledgments:
We are grateful to A. Verma for constructive comments. We thank A. Baker, M. Tecza, D. Rigopoulou, and C. Iserlohe for their input in the early phases of this study, and the ESO Paranal staff for their excellent support.

3

Post-coalescence ultraluminous merger phases

...or... Dynamical properties of ULIRGs II: Traces of dynamical evolution and end products of local ultraluminous mergers

K. M. Dasyra, L. J. Tacconi, R. I. Davies, T. Naab, R. Genzel, D. Lutz, E. Sturm, A. J. Baker, S. Veilleux, D. B. Sanders, & A. Burkert 2006, ApJ, submitted

Abstract

We present results from our Very Large Telescope large program to study the dynamical evolution of local Ultraluminous Infrared Galaxies and QSOs. This paper is the second in a series presenting the stellar kinematics of 54 ULIRGs, derived from high resolution, long-slit H- and K-band spectroscopy. The data presented in this paper (17 of which are new) are mainly focused on sources that have coalesced into a single nucleus. The stellar kinematics, extracted from the CO rovibrational bandheads in our spectra, indicate that ULIRG remnants are dynamically heated systems with a mean dispersion of 161 km s^{-1} . The combination of kinematic, structural, and photometric properties of the remnants indicate that they mostly originate from major encounters (also see the first paper in the series) and that they result in the formation of dispersion-supported systems (elliptical galaxies). The peak of

the velocity dispersion distribution and the locus of ULIRGs on the fundamental plane of early-type galaxies indicates that the end products of ultraluminous mergers are typically moderate-mass ellipticals (of stellar mass $\sim 10^{10}$-$10^{11} M_{\odot}$). Converting the host dispersion into black hole mass with the aid of the $M_{\rm BH} - \sigma$ relation yields black hole mass estimates of the order 10^7- 10^8 $M_{\odot}$ and high accretion rates (of Eddington efficiencies often > 0.5).

3.1 Introduction

Galaxy mergers, the frequency of which increases with redshift (e.g., Toomre 1977; Kauffmann & White 1993; Le Fèvre et al. 2000), are considered a key mechanism in driving galaxy evolution. In the local Universe, the best laboratories for studying violent merging events (believed to be the probable analogs of high-redshift mergers) are the ultraluminous infrared galaxies. ULIRGs are mergers of gas-rich galaxies observed during strong starburst events; these events are believed to last short ($\lesssim 10^8$ yrs; e.g. Canalizo & Stockton 2001; Mihos & Hernquist 1996) compared to the baryonic matter merging process ($\sim 10^9$ yrs; e.g. Barnes 1992; Hernquist 1993) and to have a strong infrared output. The starburst emission, often combined with emission originating from an active galactic nucleus, gives rise to IR luminosities greater than $10^{12} L_{\odot}$ (e.g., Sanders & Mirabel 1996; Lonsdale et al. 2006 and references therein); these luminosities are comparable to the bolometric luminosities of QSOs.

A plethora of studies indicates that ULIRGs transform (gas-rich) spiral galaxies into ellipticals through merger-induced dissipative collapse (Kormendy & Sanders 1992; Mihos & Hernquist 1996; Barnes & Hernquist 1996). The large molecular gas concentrations in the central kpc regions of ULIRGs (e.g. Downes & Solomon 1998; Bryant & Scoville 1999) have densities comparable to stellar densities in ellipticals. Kim et al. (2002) and Veilleux et al. (2002) have analyzed the structural parameters of a sample of 118 ULIRGs that have 60 μm flux greater than 1 Jy (hereafter the 1 Jy sample; Kim & Sanders 1998). They find that most (73%) are well-fit by an elliptical-like $r^{1/4}$ light profile. Similar findings on the near-IR light distributions of ULIRGs were reported by Scoville et al. (2000) and Rothberg & Joseph (2004). Genzel et al. (2001) and Tacconi et al. (2002) have made high-resolution near-infrared spectroscopic measurements of the stellar dynamics of small samples consisting mostly of fully-merged ULIRGs. They conclude that ULIRGs resemble intermediate mass ellipticals/lenticulars with moderate rotation, in their velocity dispersion distribution, their location in the fundamental plane (FP; e.g., Djorgovski & Davis 1987; Dressler et al. 1987) and their distribution

of the rotation/velocity dispersion ratio. Together, these results suggest that ULIRGs form moderate mass ellipticals (of stellar mass $\sim 10^{11}$ $M_{\odot}$).

One way to investigate the physical details and the evolution of ULIRGs is to determine the kinematic and structural properties of the merging (or interacting) galaxies in different merger phases. We therefore conducted a European Southern Observatory large program[1] that traces the host dynamics of a large sample of ULIRGs (spanning wide ranges of merger phase and infrared luminosity) through NIR spectroscopy. Our study extends the previous work by Genzel et al. (2001) and Tacconi et al. (2002). The updated sample comprises ULIRGs at wider ranges of merger phase, lower luminosities, and higher redshifts than that of Tacconi et al. (2002). The new observations of 38 sources increase the original sample by more than a factor of 3, enhancing our statistics and enabling us to study the merging galaxy properties as a function of time. In Dasyra et al. (2006, hereafter Paper I) we analyzed those ULIRGs that are in a merger phase later than the first encounter but prior to nuclear coalescence, and hence, show more than one nucleus in the NIR acquisition images. In this paper we present results mainly from those ULIRGs that have coalesced and show a single nucleus in our images, the so-called remnants. We compare the stellar kinematic properties of binary ULIRGs and ULIRG remnants to study the evolution of ultraluminous mergers.

Some of the ULIRGs presented in this study may in fact be binary sources very close to coalescence that have small projected nuclear separations; such sources cannot always be resolved (or kinematically disentangled) due to instrumental angular resolution constraints. At redshifts typical for the sources in our sample, the angular resolution achieved implies that any unresolved systems will have nuclear separations smaller than 1.5 kpc. Merger simulations (e.g. Mihos 2000; Mihos 1999) have shown that by the time the individual nuclei are separated by $\lesssim$ 1 kpc, the (low moments of the) stellar kinematics have almost reached their relaxation values. Therefore, the dynamical properties of all the sources we classify as remnants are representative of those at dynamical equilibrium.

This paper is arranged as follows. We briefly summarize the observations and data reduction methods and present the pre- and post- coalescence ULIRG samples in § 3.2. After studying whether the kinematic properties of the merging galaxies evolve during the ultraluminous merger phases in § 3.3, we investigate the origin and the potential end products of ultraluminous mergers in § 3.4 and § 3.5 respectively. We then focus on the black hole properties of ULIRGs: an analysis of the evolution of the $M_{\rm BH}$- σ relation during the merger is followed by a discussion of the nuclear activity implied by our data

[1] 171.B-0442 (PI Tacconi)

in § 3.6. Finally a summary is presented in § 3.7.

3.2 Observations And Data Reduction

3.2.1 Data Acquisition And Analysis

We combine the sources in our Very Large Telescope program with the sources presented in Genzel et al. (2001) and Tacconi et al. (2002) to compile a sample that comprises 54 ULIRGs and 12 QSOs. The stellar kinematics of the QSOs will be presented in a forthcoming paper (Dasyra et al. 2006, in preparation). In this paper, we perform a study of the stellar kinematics in post-coalescence ultraluminous mergers (ULIRG remnants), after presenting new data for 17 ULIRGs and summarizing pre-existing data for 13 (mainly post-coalescence) sources. Of the 54 ULIRGs observed in total, 30 are confirmed to be binary sources[2], and 1 (IRAS 00199-7426: Duc et al. 1997; Paper I) may be a multiple-interaction system. A detailed description of the criteria set to select these 54 sources from the 1 Jy catalog is given in Paper I.

Our new high-resolution, long-slit spectroscopic data were obtained using the ISAAC spectrometer (Moorwood et al. 1998) mounted on the Antu telescope unit of the VLT. The observations were made in the H and K bands, with an instrument resolution of $\lambda/\delta\lambda$=5100 and $\lambda/\delta\lambda$=4400 respectively. The slit length was $120''$ and the slit width $0.''6$ leading to a detector pixel scale of $0.''146$ per pixel. The total exposure times, and the slit position angles for each source are presented in Table 3.1. If the position angle of the major axis of rotation could not be identified for the remnants (e.g. from the elongation of the stellar disk), the slits were typically placed at 0° and 90°. The redshift range of all sources in our sample is $0.018 < z < 0.268$ (see Table 3.1). No sources are observed for the redshift sub-range $0.163 < z < 0.199$, since the CO bandheads are then shifted into wavebands of high atmospheric absorption.

As in Paper I, we derive the structural parameters of the sources that do not have high-resolution NIR imaging (e.g. Hubble Space Telescope NICMOS) data by fitting ellipses to our 10-second-long H-band acquisition images (with the aid of the SExtractor package; Bertin & Arnouts 1996). The half-light radius $R_{\rm eff}$, the ellipticity, and the angle ϕ_α between the major axis of rotation and the position angle of the first slit are presented in Table 3.2 for each source. To convert all angular distances into linear sizes we use a H_0=70 km s^{-1} Mpc^{-1}, Ω_m=0.3, $\Omega_{\rm total}$=1 cosmology. Whenever K-band effective radii are available in the literature (see Table 3.2), we assign to $R_{\rm eff}$ the

[2](20 first presented in Paper I and 10 presented or summarized here; see the Appendix)

mean value of the measurement in the H and in the K band (as in Genzel et al. 2001 and Tacconi et al. 2002). This assignment is performed to increase the accuracy of the $R_{\rm eff}$ measurement since the offset between the two values is usually small and non-systematic (Scoville et al. 2000; Surace & Sanders 1999).

The extraction of the stellar central velocity dispersion σ and rotational velocity $V_{\rm rot}$ from the spectra follows the method presented in Paper I. It is performed using the Fourier quotient technique (Bender 1990); this method provides the intrinsic line-of-sight (LOS) velocity profile along any given aperture. To this we fit a high-order Gaussian (linear combination of a Gaussian and a second order polynomial) to determine the average LOS radial velocity and velocity dispersion. The fit is performed to each bandhead individually and the errors are equal to the standard deviation of all measurements performed. The central aperture spectrum of each source (combined over the two slits and shifted to restframe) is displayed in Fig. 3.1. The stellar template that fits best the post-coalescence ULIRG spectra is an M0III giant (HD 25472; presented in Genzel et al. 2001). In general template missmatch affects the accuracy to which the stellar velocities are measured; we found that the difference in the velocity dispersion between the (best-fitting) M0III giant and an M1I supergiant (HD 99817; Genzel et al. 2001) is $\sim$15 km s^{-1} . The M0III template is overplotted with a dashed line in Fig. 3.1, after being convolved with the Gaussian that best simulates the LOS broadening function.

In all analyses of this paper we consider that aperture effects are negligible for the measurement of the stellar velocity dispersion. According to the merger simulations of Bendo & Barnes (2000), the dispersion velocity in (relaxed) remnants varies at most by 10% for the apertures considered here (up to $\sim 2R_{\rm eff}$), which are selected to maximize the signal-to-noise ratio. Resolution effects further reduce differences in the dispersion velocity measurement between various apertures.

From the LOS rotational velocity, $V_{\rm rot}$(LOS) measured along each slit, we calculate the observed rotational velocity $V_{\rm rot}(obs)$ by correcting for the angular deviation of the slit from the major axis of rotation as

$$V_{\rm rot}(obs) = V_{\rm rot}[{\rm LOS}]/cos[\phi_\alpha], \tag{3.1}$$

and by averaging the result over the slits. The value of the observed rotational velocity is given in Table 3.3 and is related to the actual rotational velocity $V_{\rm rot}$ by

$$V_{\rm rot}({\rm obs}) = V_{\rm rot} sin(i). \tag{3.2}$$

In this paper we do not compute the inclination i from the ellipticity of each source (as we did in Paper I); this conversion is very uncertain for the ULIRG

remnants since their stellar disks are dynamically hot (due to the advanced phase of the merger). Instead, we statistically determine the mean inclination that needs to be applied to the sample. For this purpose, we use the mean (weighted) value of $sini$ observed for disk-like galaxies on the sky. Since the probability $p[i]$ of finding a galaxy at an inclination i (in the range [0°,90°]) scales with $sini$ (Collin et al. 2006), the mean value of $p[i]sini$ is 2/3. The stellar kinematic results (central velocity dispersion and rotational velocity) can be found in Table 3.3.

Table 3.1: List of Observed ULIRGs

Galaxy (IRAS)	RA (2000)	Dec (2000)	z	$\log(L_{\rm IR}/{\rm L}_{\odot})$	slit P.A. ($^{\circ}$)	$t_{\rm integration}$ (mins)	Merger phase [a] classification
00091−0738	00:11:43.3	−07:22:08	0.118	12.19	17,106	60,60	R
00199-7426 [b]	00:22:07.0	-74:09:42	0.096	12.23	-15,75,74	60,60,60	U
00262+4251 [c]	00:28:54.0	+43:08:18	0.0927	12.02	45,0	20,60	R
00397−1312	00:42:15.5	−12:56:04	0.262	12.90	-1,89	120,120	R
00456−2904 [c]	00:48:06.8	−28:48:19	0.110	12.12	30	40	B
F01004−2237	01:02:49.9	−22:21:57	0.118	12.24	-1,89	60,60	R
01166-0844 [b]	01:19:07.6	-08:29:10	0.118	12.03	-60,29,29	60,60,60	B
01388−4618 [c]	01:40:55.9	−46:02:53	0.090	12.03	0,90	40,40	R
01572+0009 (Mrk 1014) [c]	01:59:50.2	+00:23:41	0.163	12.53	20, -70	80, 60	R
F02021−2103	02:04:27.3	−20:49:41	0.116	12.01	53,142	60,60	R
02364-4751 [b]	02:38:13.1	-47:38:11	0.098	12.10	0,90	60,50	B
04103−2838	04:12:19.5	−28:30:24	0.117	12.55	89	60	R
04313−1649	04:33:37.1	−16:43:32	0.268	12.55	-1,89	120,120	R
05189−2524	05:21:01	−25:21:46	0.043	12.09	-1,89	200,160	R
06035-7102 [b]	06:02:54.0	-71:03:10	0.0795	12.12	65,153,153	60,50,60	B
09039+0503	09:06:34.2	+04:51:25	0.125	12.07	-1,89	60,60	R
09111−1007	09:13:38.8	−10:19:20	0.054	11.95	34,124	120,60	B
10190+1322 [b]	10:21:42	13:07:01	0.077	12.00	64,149,149	40,40,40	B
10565+2448 [b]	10:59:18.1	24:32:34	0.0431	12.02	-66,24	40,40	B
11095-0238 [b]	11:12:03	-02:54:18	0.106	12.20	39,129	120,120	B
11223−1244	11:24:50	−13:01:13	0.199	12.59	-1,89	80,80	U
12071-0444 [b]	12:09:45.1	-05:01:14	0.128	12.35	-1,89	60,60	B
12112+0305 [b]	12:13:47	02:48:34	0.073	12.28	37,99	60,60,40	B
12540+5708 (Mrk 231) [c]	12:56:14.2	−56:52:25	0.042	12.50	10,-30,-80	40,40,40	R
13335-2612 [b]	13:36:22	-26:27:31	0.125	12.06	-5	100	B
13428+5608 (Mrk 273) [c]	13:44:42.1	−55:53:13	0.037	12.13	15,95	40,40	R
13451+1232 [b]	13:47:33	12:17:23	0.122	12.28	104,13	80,120	B
14070+0525	14:09:31.3	+05:11:31	0.264	12.76	-1,89	120,120	R
14348−1447 [c]	14:37:38.3	−15:00:23	0.0823	12.3	30	240	B
14378−3651 [c]	14:40:58.9	−37:04:33	0.068	12.24	-45	80	R
15130−1958	15:15:55.2	−20:09:17	0.109	12.09	-171,-81	80,110	R
15250+3609 [c]	15:26:59.4	−35:58:38	0.055	11.99	45, -45	40,40	R
15327+2340 (Arp 220) [c]	15:34:57.1	23:30:11	0.0181	12.1	52, -91	120,120	R
15462−0450	15:48:56.8	−04:59:34	0.100	12.16	179,-91	180,160	R
16156+0146 [b]	16:18:08	01:39:21	0.132	12.04	-50,-51,40,40	60,60,60,60	B
16300+1558 [b]	16:32:20	15:51:49	0.242	12.63	-1,89	150,90	B
16504+0228 (NGC 6240)[c]	16:52:58.9	02:24:03	0.0245	11.8	-158,-31	20,20	R
17208−0014 [c]	17:23:21.9	−00:17:00	0.0428	12.33	90,120	30, 30	R
19254-7245 [b]	19:31:21.4	-72:39:18	0.0617	12.00	-13,77	60,60	B
20046-0623 [b]	20:07:19.3	-06:14:26	0.0844	11.97	69,159	60,60	B
20087−0308 [c]	20:11:23.2	−02:59:54	0.106	12.40	-45,45	40,40	R
20414−1651	20:44:18.2	−16:40:16	0.087	12.26	54,144	100,80	R
20551−4250 [c]	20:58:26.9	−42:39:06	0.0428	11.98	-45,45	60,60	R
21130-4446 [b]	21:16:18.5	-44:33:38	0.0926	12.02	33	40	B
21208-0519 [b]	21:23:29	-05:06:59	0.13	12.01	-164,109,109	60,60,60	B
21219−1757	21:24:41.6	−17:44:46	0.112	12.06	-1,89	50,40	R
21329-2346 [b]	21:35:45	-23:32:36	0.125	12.09	31	60	B
21504−0628	21:53:05.5	−06:14:50	0.078	11.92	-39,59	60,60	R
22491-1808 [b]	22:51:49.2	-17:52:23	0.0778	12.09	-76,13,13	60,60,60	B
23128-5919 [b]	23:15:46.8	-59:03:15	0.045	11.96	-5,84,84	40,40,40	B
23230−6926	23:26:03.6	−69:10:19	0.106	12.17	-1,89	60,60	R
23234+0946 [b]	23:25:56.2	10:02:50	0.128	12.05	-64,25	60,60	B
23365+3604 [c]	23:39:01.3	+36:21:10	0.0645	12.09	45, -30	15, 40	R
23578−5307 [c]	00:00:23.6	−52:50:28	0.125	12.10	107,14	60, 40	R

The coordinates, the redshift, the infrared luminosity, as well as the position angles and respective integration time for all our sources are presented in this Table. The data are presented in this paper unless otherwise noted.

[a] Pre- or post- coalescence classification, according to the scheme described in § 3.2.2. "B" refers to a binary (pre-coalescence) source. "R" refers to a remnant (in post-coalescence). Remnants may also have two nuclei, separated by no more than 1.5 kpc. "U" indicates that the classification is uncertain.

[b] Source presented in Paper I.

[c] Source presented in Genzel et al. (2001) and Tacconi et al. (2002).

Table 3.2: Structural and photometric parameters

Galaxy (IRAS)	$R_{\rm eff}(H\ band)$ (kpc)	ellipticity	ϕ_α (°)	$R_{\rm eff}(K\ band)$ (kpc)	$\mu_{\rm gal}(H\ band)$ mag $(''){}^{-2}$	$\mu_{\rm gal}(K\ band)$ mag $(''){}^{-2}$
00091−0738	2.47(±0.21)	0.220	15	...	...	16.96 [g]
00262+4251 [a]	...	...	...	3.4 (±1.0) [e]	...	...
00397−1312 [b]	2.04 (±0.76)	0.35	-25	...	16.58	15.28 [g]
F01004−2237 [b]	0.40 (±0.07)	0.02	26	...	14.42	13.05
01388−4618	1.62 (±0.03)	0.074	55	...	...	14.86 [i,g]
01572+0009	1.31 (±0.10)	0.140	81	3.16 (±1.42) [c]	14.77 [d]	13.83 [d]
F02021−2103 [b]	5.38 (±3.95)	0.34	1	...	17.24	17.35 [g]
04103−2838 [b]	1.61 (±0.12)	0.19	-80	...	15.71	15.11 [g]
04313−1649 [b]	4.04 (±0.89)	0.26	86	5.7 [f]	18.00	18.17 [g]
05189−2524 [b]	0.57 (±0.08)	0.06	77	0.79 (±0.02) [c]	13.38	13.64 [d]
09039+0503 [b]	1.62 (±0.90)	0.15	-18	...	16.34	15.66 [g]
11223−1244	3.83 (±0.38)	0.101	70	...	...	16.27 [g]
12540+5708 [b]	1.40 (±0.21)	0.08	-11	0.2 [e]	14.80	13.33
13428+5608 [c]	1.03 (±0.29)	0.498	-77	1.15(±0.24) [c]	15.23 [d,g]	14.27 [d,g]
14070+0525 [b]	3.62 (±0.53)	0.17	-19	...	17.37	16.39 [g]
14378−3651	0.36 (±0.02)	0.031	20	0.67 [e]	14.64 [h]	13.57 [j,g]
15130−1958 [b]	1.62 (±0.27)	0.23	-88	...	16.20	15.18 [g]
15250+3609 [c]	2.10 (±0.09)	0.207	-72	1.49(±0.12) [c]	17.02 [d,g]	16.70 [d,g]
15462−0450 [b]	5.57 (±1.38)	0.048	62	1.6 [f]	18.59	16.40 [g]
17208−0014	1.69 (±0.08)	0.196	54	1.63(±0.07) [c]	16.00 [d,g]	15.79 [d,g]
20087−0308	1.87 (±0.22)	0.324	-86	...	...	15.39 [j,g]
20414−1651 [b]	1.37 (±0.47)	0.67	3	...	16.36	15.80 [g]
20551−4250	1.32 (±0.25)	0.113	84	...	...	15.80 [j,g]
21219−1757 [b]	4.19 (±3.29)	0.14	-50	...	17.04	15.73 [g]
21504−0628	1.95 (±0.26)	0.164	12	...	...	...
23230−6926	2.03 (±0.25)	0.177	41	...	16.92 [h]	16.37 [j,g]
23365+3604 [a]	4.8 (±1.0) [e]	...	...	...	...	...
23578−5307	3.96 (±1.36)	0.447	-80	...	...	...
Arp 220 [d]	3.00	...	...	0.69(±0.03) [c]	17.56 [d,g]	16.98 [d,g]
NGC 6240 [d]	1.44	...	...	0.92(±0.23) [c]	14.42 [d,g]	13.93 [d,g]
00456−2904(SW)	2.09 (±0.15)	0.067	-88	...	16.47	...
09111−1007(W)	2.18 (±0.36)	0.397	-26	...	...	...

Structural and photometric properties of (mainly) ULIRG remnants. The H-band structural parameters $R_{\rm eff}$, ellipticity, and ϕ_α are derived from the ISAAC acquisition images unless otherwise noted in the first column. The galaxy surface brightness within the effective radius, $\mu_{\rm gal}$ is derived from Veilleux et al. (2006) and Kim et al. (2002) respectively, unless otherwise noted. The H- and K-band $\mu_{\rm gal}$ data are presented after subtraction of the nuclear PSF for both bands; we indicate when individual PSF and galaxy magnitudes are not available in the literature. All data presented in this Table are derived from maximum-aperture photometry (enclosing the whole galaxy) and are not corrected for extinction effects.

[a] For the sources observed using NIRSPEC and the slit monitoring camera, the structural parameters are not extracted; the slit projection drawn on the acquisition image does not allow for photometric analysis.

[b] Data taken from H-band NICMOS imaging by Veilleux et al. (2006). All quantities are PSF-subtracted and are converted to our cosmology.

[c] Structural parameters extracted from NICMOS imaging data, kindly provided to us by Nick Scoville.

[d] Based on Scoville et al. (2000).

[e] Effective radius from Genzel et al. (2001) or Tacconi et al. (2002).

[f] Data from the 1 Jy sample analysis (Veilleux et al. 2002).

[g] For these sources the relative strength of the PSF and the Sérsic component fit to the underlying galaxy are not known. We assume that $L_{gal}(H\ \text{band}) = 0.64 L_{tot}(H\ \text{band})$ and that $L_{gal}(K\ \text{band}) = 0.48 L_{tot}(K\ \text{band})$, (Colina et al. 2001; Surace & Sanders 1999; Veilleux et al. 2006).

[h] H-band magnitude taken from Colina et al. (2001).

[i] K-band magnitude taken from Rigopoulou et al. (1999).

[j] K-band magnitude taken from Duc et al. (1997).

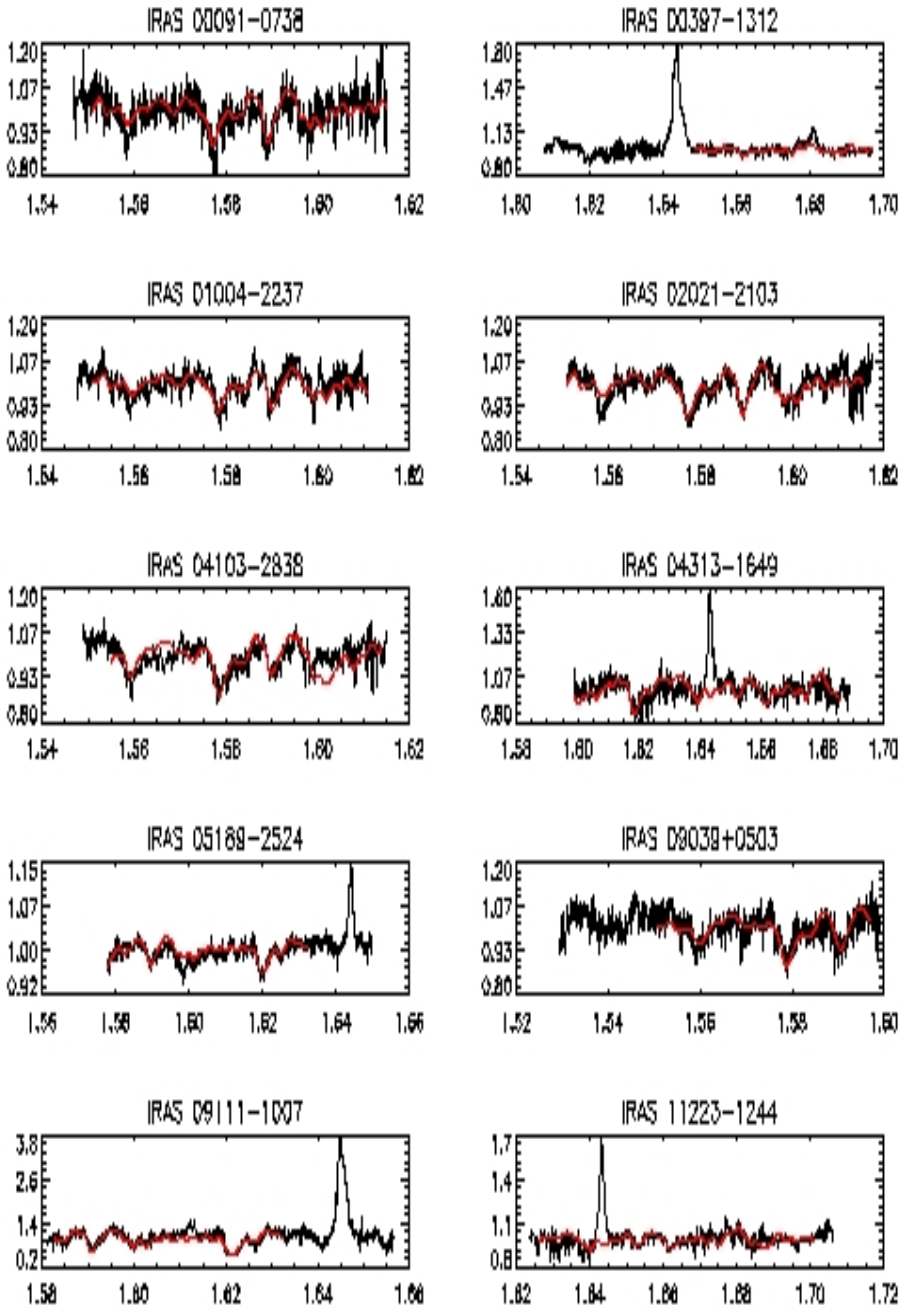

Figure 3.1: The H-band spectra of the ULIRG remnants from this study. The stellar template, convolved with Gaussians that represent the LOS broadening function of the sources, is overplotted as a solid line. All spectra are shifted to rest frame.

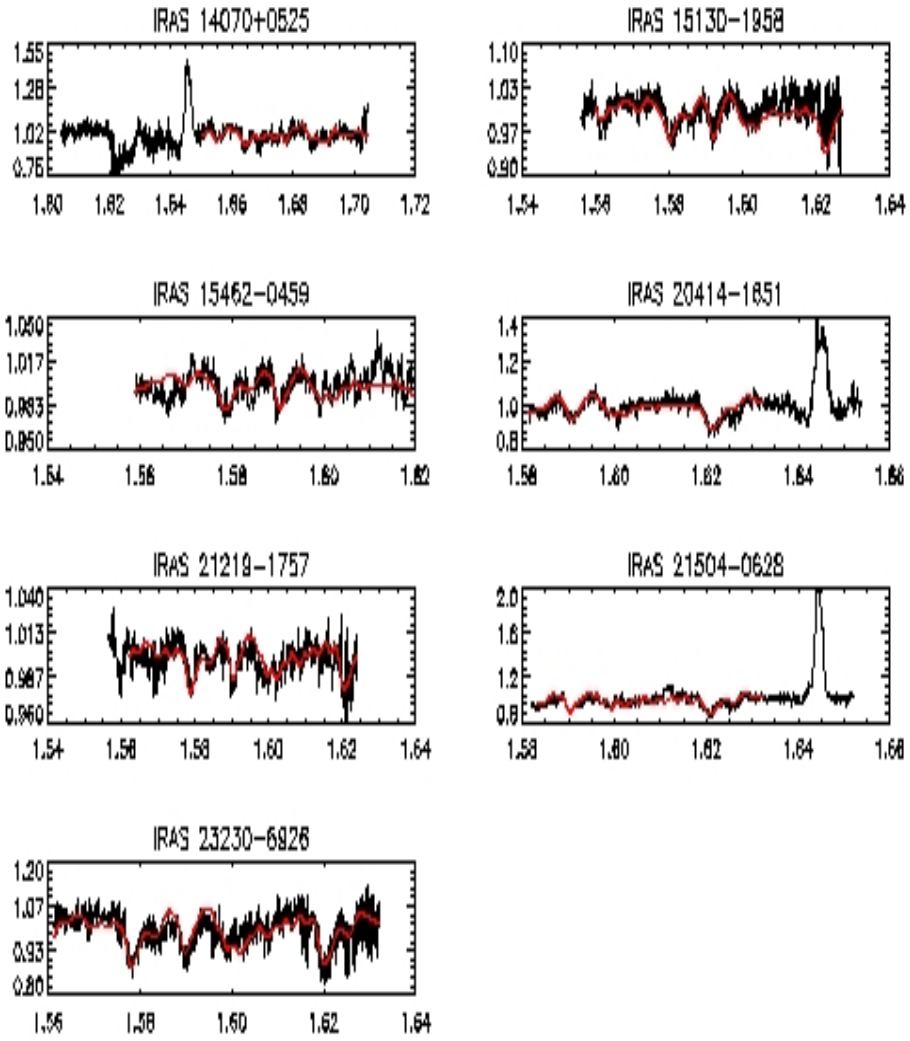

Fig. 3.1 continued.

Table 3.3: Stellar velocities and resulting black hole masses.

Source IRAS	σ (km s^{-1})	aper.[a] $''$	$V_{\rm rot}$(obs) [b] (km s^{-1})	aper.[c] $''$	$V_{\rm rot}$(obs)/σ	$M_{\rm BH}$ [d] ($M_\odot$)	$M_{\rm BH}$(Edd.) [e] ($M_\odot$)	$\eta_{\rm Edd}$ [f]
00091−0738	131 (± 39)	0.45	...	...	...	2.46×10^7	2.04×10^7	0.83
00262+4251	170 (± 15)	...	< 15	...	< 0.09	7.02×10^7	1.32×10^7	0.19
00397−1312	106 (± 26)	0.36	49 (± 17)	0.58	0.46	1.05×10^7	1.05×10^8	9.94
F01004−2237	132 (± 29)	0.29	22 (± 13)	0.60	0.17	2.54×10^7	2.29×10^7	0.90
01388−4618	144 (± 10)	...	130 (± 15)	...	0.90	3.60×10^7	1.32×10^7	0.37
01572+0009	200 (± 60)	...	...	...	...	1.35×10^8	4.46×10^7	0.33
F02021−2103	143 (± 21)	0.37	42 (± 10)	0.76	0.29	3.50×10^7	1.35×10^7	0.38
04103−2838	129 (± 40)	0.29	4 (± 5)	0.31	0.03	2.32×10^7	1.86×10^7	0.80
04313−1649	157 (± 21)	0.38	31 (± 27)	0.57	0.20	5.10×10^7	4.67×10^7	0.92
05189−2524	137 (± 16)	0.29	70 (± 14)	0.51	0.51	2.95×10^7	1.62×10^7	0.55
09039+0503	183 (± 38)	0.58	...	...	...	9.45×10^7	1.55×10^7	0.16
11223−1244	149 (± 27)	0.73	...	...	...	4.13×10^7	5.12×10^7	1.24
12540+5708	120 (± 10)	...	25 (±10)	...	0.21	1.73×10^7	4.16×10^7	2.40
13428+5608	285 (± 30)	...	110 (±20)	...	0.39	5.61×10^8	1.66×10^7	0.03
14070+0525	139 (± 21)	0.70	54 (± 19)	0.77	0.39	3.13×10^7	7.57×10^7	2.42
14378−3651	153 (± 10)	...	15 (±10)	...	0.10	4.60×10^7	1.66×10^7	0.36
15130−1958	177 (± 39)	0.58	33 (± 21)	0.66	0.19	8.26×10^7	1.62×10^7	0.20
15250+3609	150 (± 10)	...	60 (±15)	...	0.40	4.25×10^7	1.32×10^7	0.31
15462−0450	169 (± 38)	0.58	...	...	...	6.86×10^7	1.90×10^7	0.28
17208−0014	229 (± 15)	...	110 (± 20)	...	0.48	2.33×10^8	2.63×10^7	0.11
20087−0308	219 (± 14)	...	50 (± 15)	...	0.23	1.94×10^8	3.31×10^7	0.17
20414−1651	187 (± 32)	0.44	96 (± 38)	0.88	0.51	1.03×10^8	1.82×10^7	0.18
20551−4250	140 (± 15)	...	40 (± 10)	...	0.29	3.22×10^7	1.32×10^7	0.41
21219−1757	121 (± 11)	0.58	...	...	...	1.79×10^7	1.51×10^7	0.84
21504−0628	90 (± 31)	0.32	9 (± 28)	0.48	0.10	5.45×10^6	8.30×10^6	1.52
23230−6926	143 (± 14)	0.48	23 (± 13)	0.73	0.16	3.50×10^7	1.44×10^7	0.41
23365+3604	145 (± 15)	...	< 15	...	< 0.10	3.71×10^7	1.62×10^7	0.44
23578−5307	190 (± 70)	...	...	...	...	1.10×10^8	1.66×10^7	0.15
Arp 220	164 (± 10)	...	185 (± 30) [g]	...	0.84	6.08×10^7	1.66×10^7	0.27
NGC 6240	229 (± 43) [h]	...	240 (± 108) [h]	...	1.05	2.33×10^8	8.30×10^6	0.04
00456−2904(SW)	162 (± 25)	...	45 (± 10)	...	0.28	5.79×10^7	1.73×10^7	0.30
09111−1007(W)	112 (± 18)	0.29	68 (± 16)	1.17	0.61	1.31×10^7	9.53×10^6	0.73

The stellar central velocity dispersion, rotational velocity, and the $V_{\rm rot}/\sigma$ ratio are derived from the spectra of Fig. 3.1 with the aid of the parameters of Table 3.2. The dynamical and Eddington black hole mass of each ULIRG and the ratio of the two are also presented here.

[a] Radial extent of the central aperture used for the extraction of σ.

[b] The observed rotational velocity value presented in this column is corrected for angular deviations from the major axis of rotation but not for inclination effects.

[c] Center of the outer aperture used for the extraction of $V_{\rm rot}$.

[d] Dynamical black hole masses estimated from their relation to the bulge dispersion (Tremaine et al. 2002).

[e] Eddington black hole mass, calculated by attributing 50% of $L_{\rm IR}$ to the AGN.

[f] Ratio of Eddington black hole mass over dynamical black hole mass.

[g] We use as rotational velocity of Arp 220 that of the east component, since that of the west component is only a lower limit (Genzel et al. 2001).

[h] Data are taken from Tecza et al. (2000). The average of the velocity dispersion values at the two nuclei and the internuclear region is tabulated here. This value is also close to the luminosity-weighted average of the two nuclei which equals 225 km s^{-1} .

3.2.2 Pre- and Post-coalescence Sample Classification

Prior to performing statistics on the kinematic results of the pre- and post-coalescence ULIRG samples, we descibe the criterion we use to compile the two samples; we set a nuclear separation threshold beyond which binary sources can be considered relaxed. According to numerical simulations, this nuclear separation should be roughly 1 kpc (Mihos 2000). The actual value of the threshold we set depends on the resolution of the images we use to investigate for the presence of secondary components.

Our acquisition images have been obtained with ISAAC, on the $H-$band imaging mode of the instrument (corresponding to a scale of $0\farcs147$ per pixel). We compute the resolution of our images (which also depends on the seeing) by averaging the FWHM of bright stars in the field. Our mean resolution corresponds to a FWHM of 4.3 pixels and enables us to resolve individual sources separated by 1 kpc up to z=0.080. If we set the nuclear separation threshold to 1.5 kpc, we can distinguish individual sources up to z=0.118. The number of sources in our ULIRG remnant sample that are verified to satisfy the coalescence criterion increases respectively from 10 to 23. We adopt a nuclear separation cutoff of 1.5 kpc. For this nuclear separation, the low velocity moments are still close to their relaxation values according to the models of Mihos (2000) and Naab et al. (2006, in preparation).

From the 7 sources at $z > 0.118$, 5 have been observed with the NICMOS camera onboard the Hubble Space Telescope by Veilleux et al. (2006) and Scoville et al. (2000). According to these authors, none of IRAS 00397-1312, IRAS 01572+0009, IRAS 04313-1649, IRAS 09039+0503, and IRAS 14070+0525 has a secondary object at distances <1.5 kpc that can be unambiguously characterized as a nucleus. For one of the remaining 2 sources, IRAS 23578-5307, the large elongation and the tidal tails indicate the possible presence of two components (see Fig. 3.2; left panel). To investigate this possibility, we deconvolve our acquisition image with its point-spread-function (PSF) which has a FWHM of 4.1 pixels. For this task, we use the LUCY algorithm of IRAF (Lucy 1974; Richardson 1972). The deconvolution increases the resolution of the image by a factor of $\sim$2 (since the new FHWM is 2.1 pixels). The resulting image (see Fig. 3.2; right panel) confirms the presence of a second nucleus and constrains its separation to a linear size of 1.4 ± 0.4 kpc. Unlike that of IRAS 23578-5307, the redshift of IRAS 11223-1244 is too high to enable us to derive any conclusions using image deconvolution techniques. IRAS 11223-1244 is therefore excluded from all statistics that follow. The same applies to the (possibly) multiple merger IRAS 00199-7426.

A summary of the classification of all sources in our sample can be found in Table 3.1. We have a total sample of 29 ULIRG remnants, which consists

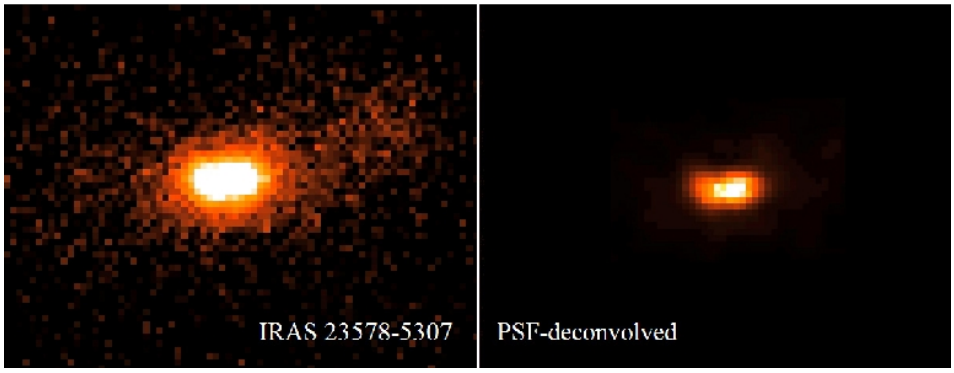

Figure 3.2: The ISAAC H-band raw (*left panel*) and PSF-deconvolved (*right panel*) acquisition image of IRAS 23578-5307.

of 21 single-nucleus or unresolved sources, and 8 (confirmed) binaries that have nuclear separations below (or equal to) the selected threshold; these sources namely are IRAS 00091-0738, IRAS 09111-1007, IRAS 14378-3651, IRAS 15250+3609, IRAS 23578-5307, Mrk 273, Arp 220 and NGC 6240 (see the Appendix). The pre-coalescence binary sample comprises 23 sources; of those, 40 individual components have velocity dispersion measurements.

3.3 Traces of Evolution In The Stellar Kinematics

Taking into account the classification scheme of § 3.2.2, we find that the σ distribution of ULIRG remnants has a mean (median) of 161 (150) km s^{-1} . The accuracy within which the mean of the distribution is known, its standard error, is 8 km s^{-1} since the standard deviation equals 42 km s^{-1} . For the pre-coalescence ULIRGs, we find that the mean (median) is 142 (145) km s^{-1} , with a standard error of 3 and a standard deviation of 21 km s^{-1} . The pre- and post- coalescence dispersion distributions are shown in Fig. 3.3 (left panel). While the difference in the mean of the two distributions is small and the modes are the same, the remnant velocity dispersion distribution has a larger variance and a tail at the high-σ end, the statistical significance of which needs to be quantified.

To investigate whether the two distributions are independent, we begin by using the Kolmogorov-Smirnov (KS) test, which makes no assumptions on the shape of the distributions under examination. We find that the maximum deviation D between the cumulative-fraction distribution of the two ULIRG populations is 0.285, which for the number of sources we observed, corresponds to a probability of 89.4% that the populations are independent.

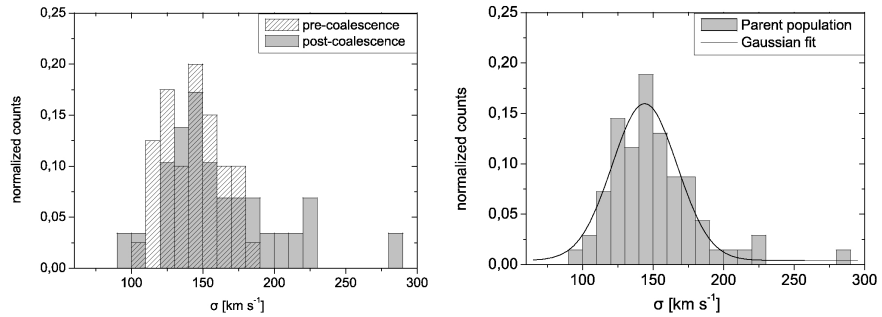

Figure 3.3: *Left panel:* The distributions of stellar dispersions in ULIRGs before and after nuclear coalescence. *Right panel:* The ULIRG parent-population distribution (and the Gaussian fit to it) used in our Monte Carlo simulations.

This probability is below the widely-accepted significance levels. However, a well-known disadvantage of the KS test is that it is sensitive to small number statistics. To address whether a better handling of small number statistics may alter our conclusions we created Monte Carlo simulations.

The Monte Carlo code begins with the assumption that the two distributions are drawn from the same parent population. We used 10^6 points to simulate a Gaussian that fits the velocity dispersion distribution of the combined pre- and post- coalescence ULIRGs, the so-called parent population (see Fig. 3.3, right panel). From the parent distribution, we selected random points to generate two artificial progenitor/remnant subsamples (which are not necessarily Gaussian). Each generated subsample had a number of elements equal to that of the corresponding real population. We then calculated the difference in the mean of the two generated samples and the difference in the variance between each real population and the (corresponding) generated sample. We repeated this procedure for 10000 iterations and found that the probability of the difference in the mean of the two generated samples to be equal or greater than the measured one (19 km s^{-1}) is 1.6%. The probability p that the variances of both generated samples ($\sigma^2_{\rm gen,1}$ and $\sigma^2_{\rm gen,2}$ respectively) are greater than those measured (or $p[\sigma_{\rm gen,1} > 21{\rm km\ s^{-1}}] * p[\sigma_{\rm gen,2} > 42{\rm km\ s^{-1}}]$) is 1.9%. In other words, the probability that the means of the observed distributions are independent is 98.4% and the probability that their variances are independent is 98.1%. Since these probabilities correspond to ∼2.35-2.45 Gaussian sigma, the difference in the distributions is now above the widely-used significance levels. This result favors the hypothesis that the apparent kinematic evolution is real rather than an artifact of limited-number statistics.

Despite the large range of confidence levels indicated by the statistical tests,

we summarize that it is possible, although uncertain, that the observed increase in sigma reflects the dynamical heating of the merging galaxies. The significance of this result consists in that observations are able to constrain the dynamical heating that models predict for the ultraluminous phases of gas-rich mergers. Strong starbursts (and associated ULIRG phases) in gas-rich mergers typically occur between first encounter and nuclear coalescence, despite the fact that, in individual cases, their actual occurance may significantly vary in terms of time (Mihos & Hernquist 1996; Mihos 1999; Springel et al. 2005b; Veilleux et al. 2002; Mihos & Bothun 1998; Murphy et al. 2001). On a statistical basis, a binary ULIRG sample may be expected to be (roughly) mid-way from first encounter to coalescence; a ULIRG remnant sample is probably close to coalescence. For these merger phases, the theoretically predicted increase of the stellar velocity dispersion is small (Naab et al. 2006, in preparation); therefore observationaly tracing it is very important. However, prior to comparing observations with models, further data are needed to quantify at 3 Gaussian-sigma levels the evolution in σ before and after nuclear coalescence.

Another possibility that needs to be investigated prior to comparing evolution in the stellar kinematics between observations and models is whether the double- and single- nucleus ULIRGs originate from mergers of galaxies of somewhat different mass contents: the ULIRGs that are prior to nuclear coalescence may be more gas-rich (and possibly more massive) than the remnants in order to have an ultraluminous phase of comparable IR output at earlier merger phases (Mihos & Hernquist 1996). In that case, the observed dynamical heating may be less than what we would measure if we were able to observe a specific galaxy pair from the beginning until the end of the merging process. To investigate whether the starburst activity is triggered under similar conditions for pre- and post- coalescence ULIRGs, we need to quantify and compare the gas-mass content of both samples. Molecular gas mass measurements obtained by Gao & Solomon (1999) in local Luminous Infrared Galaxies (sources of $10^{11} L_{\odot} < L_{\rm IR} < 10^{12} L_{\odot}$) and ULIRGs indicate that a correlation between nuclear separation and gas fraction is observed in LIRGs but not in ULIRGs. This result indicates that the hypothesis is more likely untrue. However, to properly address the question we are now performing an extended study of the molecular gas content of 1-Jy ULIRGs using the Institut de Radio Astronomie Millimétrique (IRAM) 30-meter telescope (PI Tacconi).

The mean value of the rotational velocity is 62 (and the standard deviation is 59) km s^{-1} for the ULIRG remnants, increasing to 93 km s^{-1} when inclination effects are statistically accounted for. The observed stellar rotational velocity of each individual source and its ratio over the velocity dispersion is

presented in Table 3.3. The mean $V_{\rm rot}$(obs)/σ ratio of the remnants is 0.36, increasing to $V_{\rm rot}/\sigma$=0.55 when we apply the statistical inclination correction to the rotational velocity. The individual progenitors of the binary systems have a mean rotational velocity of 59 (with a standard deviation of 38) km s^{-1} or 105 (with a standard deviation of 96) km s^{-1} when the inclination effects are corrected from the ellipticity of each progenitor. The corresponding observed and inclination-corrected $V_{\rm rot}/\sigma$ ratio of the progenitors is 0.42 and 0.76. The somewhat lower $V_{\rm rot}/\sigma$ ratio of the remnants can only be attributed to their higher (than the progenitors) value of σ, since the difference between the pre- and post- coalescence rotational velocity is insignificant. In these calculations we have not attempted to correct the central velocity dispersion for inclination effects.

3.4 Origin Of The ULIRG Remnants

We infer the initial conditions of the mergers that lead to ultraluminous IR activity by comparing the kinematic properties of ULIRG remnants with those predicted by simulations in the literature. According to various authors (e.g. Bendo & Barnes 2000; Naab & Burkert 2003) the remnant $V_{\rm rot}$(obs)/σ ratio is an indicator of the mass ratio of the merging galaxies. In the gas-free, N-body simulations of binary mergers performed by Naab & Burkert (2003) for several mass ratios and orientations, the major mergers produced slowly rotating remnants. Those authors suggested that the $V_{\rm rot}$(obs)/σ ratio is $\sim$ 0.2 for 1:1 and $\sim$ 0.4 for 2:1 merger remnants, while it reaches higher values (0.8) when the remnants originate from minor (4:1) mergers. Our remnants agree best with a 1:1 and 2:1 merger origin, also agreeing with the directly measured progenitor mass ratios of Paper I and confirming that ULIRGs are representative of the most violent local mergers.

Naab & Burkert (2003) and Burkert & Naab (2005) have also shown a connection between the $V_{\rm rot}$(obs)/σ ratio and the remnant ellipticity at the effective radius for several progenitor mass ratios. We overplot our results with those of Naab & Burkert (2003) in Fig. 3.4; our ULIRGs are given in triangles, while the squares and the open diamonds correspond to boxy and disky isophotal-profile ellipticals (data provided to Naab & Burkert 2003 by R. Bender). Each panel corresponds to mergers of different progenitor mass ratios (denoted at the upper-left corner of each panel). Naab & Burkert (2003) show in bold, solid, and dotted contours the 90%,70%, and 50% probability of finding a merger remnant of each category in the enclosed region. We find that ULIRGs are more likely to be formed by major mergers (see Paper I).

The simulations of Naab & Burkert (2003) and Burkert & Naab (2005) did

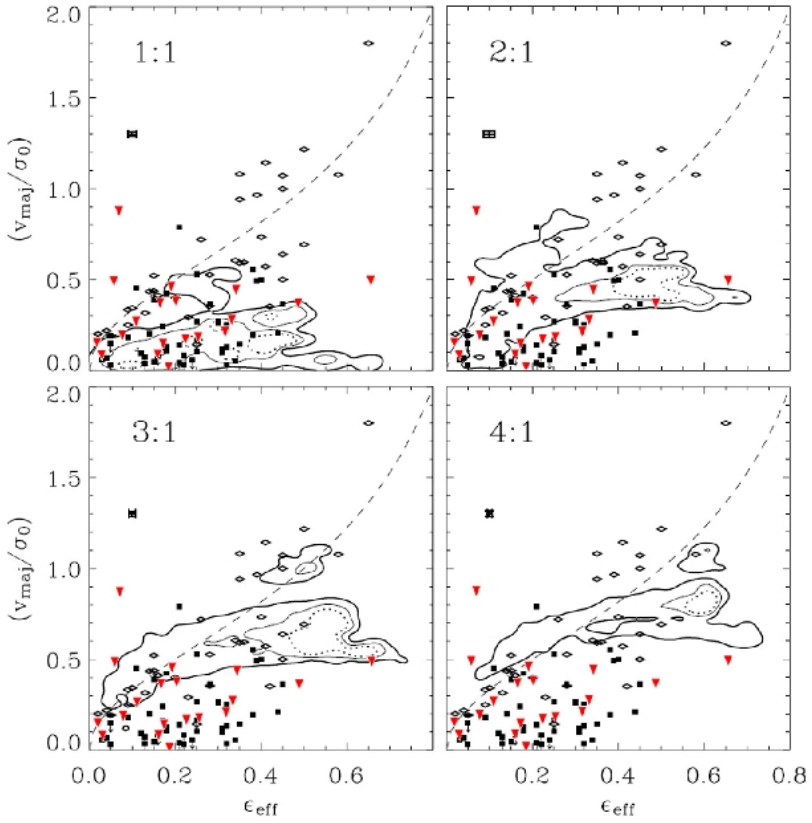

Figure 3.4: Ratio of observed rotational over dispersion velocity versus ellipticity for merger remnants (from Naab & Burkert 2003). Each panel corresponds to mergers of different progenitor mass ratios (cases from 1:1 to 4:1 are studied). The bold line, solid line, and dotted contours indicate the position of the diagram where mergers of each category are expected to be found at 90%,70%, and 50% probability levels respectively. The squares and open diamonds correspond to boxy and disky ellipticals. The dashed line shows the theoretical values for an oblate isotropic rotator. ULIRG remnants are shown as triangles.

not include gas. The addition of gas and star formation will probably result in an increase of the theoretically predicted $V_{\rm rot}({\rm obs})/\sigma$ ratio and ellipticity, since the gas that is not consumed during the merger will primarily settle in a dynamically-cold disk component(Barnes 2002; Springel 2000). According to Burkert & Naab 2005 the increase in $V_{\rm rot}({\rm obs})/\sigma$ and ellipticity would not significantly change the results. Independent of its actual value, this increase

would shift the probability contours to higher values on both axes further supporting our findings, that ULIRGs are produced mainly by mergers of galaxies of comparable masses. On the other hand, the position of ULIRGs on this diagram could be shifted upwards along the $V_{\rm rot}/\sigma$ axis due to aperture correction effects. The $V_{\rm rot}$ values used are not necessarily measured from apertures where the rotation curve has reached its flat part (van Albada et al. 1985). However, the facts that $V_{\rm rot}$ has been measured from apertures between 0.5 and 2 $R_{\rm eff}$ and that the shift cannot alter the ellipticity axis are good indications that the correction will probably not be sufficiently large to alter our conclusions.

3.5 End Products Of ULIRGs

3.5.1 The Masses Of Ultraluminous Merger Remnants

A direct way to investigate the nature of the end products of ultraluminous mergers is to calculate the mass m of their remnants. According to Bender et al. (1992) the galaxy mass is related to the stellar kinematics as

$$m = c_2 \sigma_{100}^2 R_{\rm eff}, \tag{3.3}$$

where σ_{100} is the projected central velocity dispersion in units of 100 km s^{-1} , $R_{\rm eff}$ is in kpc, and m is in 10^{10} $M_\odot$. The geometrical factor c_2 depends on the distribution of matter in the galaxy. Following Tacconi et al. (2002), we adopt $c_2 = 1.4$, as appropriate for a constant m/L King model whose tidal-to-core radius ratio is 50, midway between those of dwarf and giant ellipticals. By combining the above, the total dynamical mass is computed from

$$m = 4.7 \times 10^5 (3\sigma^2 + {V_{\rm rot}}^2) R_{\rm eff}, \tag{3.4}$$

where σ and $V_{\rm rot}$ are now in units of km s^{-1} $R_{\rm eff}$ is in kpc and m is in $M_\odot$.

We use the mean values of the stellar dispersion and inclination-corrected rotational velocity from § 3.3. Whenever $V_{\rm rot}$ is not available, we use the mean inclination-corrected $V_{\rm rot}/\sigma$ ratio of the remaining sources (0.55) to infer it. We find that the mean dynamical mass of the remnants is 8.98×10^{10} $M_\odot$ (in good agreement with Tacconi et al. 2002), suggesting that ultraluminous activity mainly originates from mergers of sub-m_* galaxies, for $m_* = 1.4\times10^{11}$ $M_\odot$ (Genzel et al. 2001 and references therein). For different values of m_* (e.g that of Bell et al. 2003 adapted to our cosmology, 8.3×10^{10} $M_\odot$) the sub-m_* characterization of ULIRGs may change to $\sim m_*$. Still, in the local Universe, the progenitor disk galaxies to ULIRGs do not need to be as massive as e.g. the Milky Way.

ULIRG masses derived from Hα emission-line dispersions are also sub-m$_*$ (Colina et al. 2005). Tracing the ionized gas by the [FeII] emission lines that appear in our spectra, we find that while the mean dispersion of the gas is similar to that of the stars, in individual cases gas and stellar dispersions may significantly deviate due to gas outflows. Gas kinematics in these ULIRGs will be presented in a forthcoming paper (Tacconi et al. 2006, in preparation).

The result that ULIRGs are sub-m_* to m_* galaxies does not contradict with findings from imaging studies which show that ULIRGs have NIR luminosities greater than L_* (e.g. Veilleux et al. 2006 Sanders et al. 2000; Colina et al. 2001). ULIRGs can simultaneously be sub-m_* and (1-2)$\times L_*$ (in the H-band) mergers since they are selected at the peak of their starburst emission; during this phase luminosity-to-mass ratio of ULIRGs does not remain constant (see also Tacconi et al. 2002; Rupke et al. 2002; 2005a; 2005b).

3.5.2 ULIRGs And The Fundamental Plane Of Es

The $V_{\rm rot}/\sigma$ ratio of the ULIRG remnants indicates that mergers of ultra-luminous infrared output lead to dispersion-supported systems with a non-negligible rotational component. To investigate what type of ellipticals ultra-luminous IR mergers form, Genzel et al. (2001) and Tacconi et al. (2002) placed our initial sample of ULIRGs on the fundamental plane of early-type galaxies (Djorgovski & Davis 1987; Dressler et al. 1987) that relates the velocity dispersion, effective radius and surface brightness of these sources. Genzel et al. (2001) and Tacconi et al. (2002) concluded that the remnants resemble moderate mass ellipticals (of stellar mass a few 10^{11} $M_\odot$). Our new data increase the number of objects in the range of ULIRG luminosity to be compared with early-type galaxies.

The $R_{\rm eff}$ - σ projection of the plane that we construct from our data is shown in Fig. 3.5. Data for early-type galaxies are taken from Bender et al. (1992), Faber et al. (1997), and Pahre (1999). Giant boxy ellipticals (squares) occupy the upper-right corner of the FP projection, while disky, moderate-mass ellipticals (circles) are located at the center. On the left panel of Fig. 3.5 we overplot the ULIRG remnants in triangles; 29 are from this study and 2 from Rothberg & Joseph (2006), UGC 5101[3] and IC 5298. The location of ULIRGs on the plane agrees very well with that of moderate-mass ellipticals. On the right panel of Fig. 3.5, we show where remnants of other merger categories are located. Local LIRGs (filled diamonds) lie from the lower-left corner of the FP projection up to the locus of giant Es (data from Shier & Fischer 1998, James et al. 1999, and Rothberg & Joseph 2006).

[3]the H- and K-band effective radius of this source equals 0.27 kpc and 1.42 kpc respectively (Scoville et al. 2000); Rothberg & Joseph 2004)

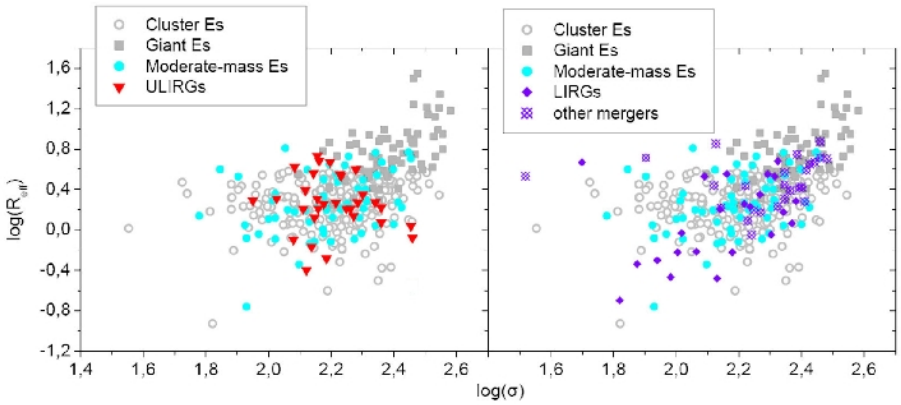

Figure 3.5: The $R_{\rm eff}$-σ projection of the early-type galaxies fundamental plane. The data for the giant boxy and moderate-mass disky Es (squares and circles respectively) are taken from Bender et al. (1992) and Faber et al. (1997). More (cluster) Es (open circles) are from Pahre (1999). For viewing clarity, the various types of mergers are plotted in separate panels. The ULIRG remnants (29 from this study and 2 from Rothberg & Joseph 2006) are plotted as triangles (left panel). LIRGs (diamonds) from Shier & Fischer (1998), James et al. (1999), and Rothberg & Joseph (2006) and other (visually-selected) mergers from Rothberg & Joseph (2006) are plotted in diamonds and open-crossed diamonds respectively (right panel).

The position of ULIRGs on this FP projection is better constrained than that of LIRGs; this result implies that ULIRGs have a narrower range of intrinsic dynamical properties than LIRGs. Other visually-selected merger remnants (i.e. sources with perturbed morphology but no IR excess; Rothberg & Joseph 2006) are shown as open-crossed diamonds. That these merger remnants lie closer than both the ULIRGs and the LIRGs to the locus of giant Es possibly reflects their different merger origin (see § 3.5.3).

In the 3-dimensional view of the plane, ULIRGs are known to deviate from the position of early-type galaxies along the surface brightness axis due to extinction and population effects (e.g., Genzel et al. 2001). Due strong starbursts, ULIRGs have a significant population of newly formed asymptotic-giant-brach stars, red giants, and supergiants. Thus, their NIR surface brightnesses are higher than those of quiescent ellipticals (Veilleux et al. 2002; Pahre 1999). Prior to comparing ULIRGs and Es, the removal of light originating from starburst components is therefore instructive. Since a significant fraction of the starburst emission is nucleated, we opt to remove the central PSF (Veilleux et al. 2006) simultaneously removing any AGN-originating emission.

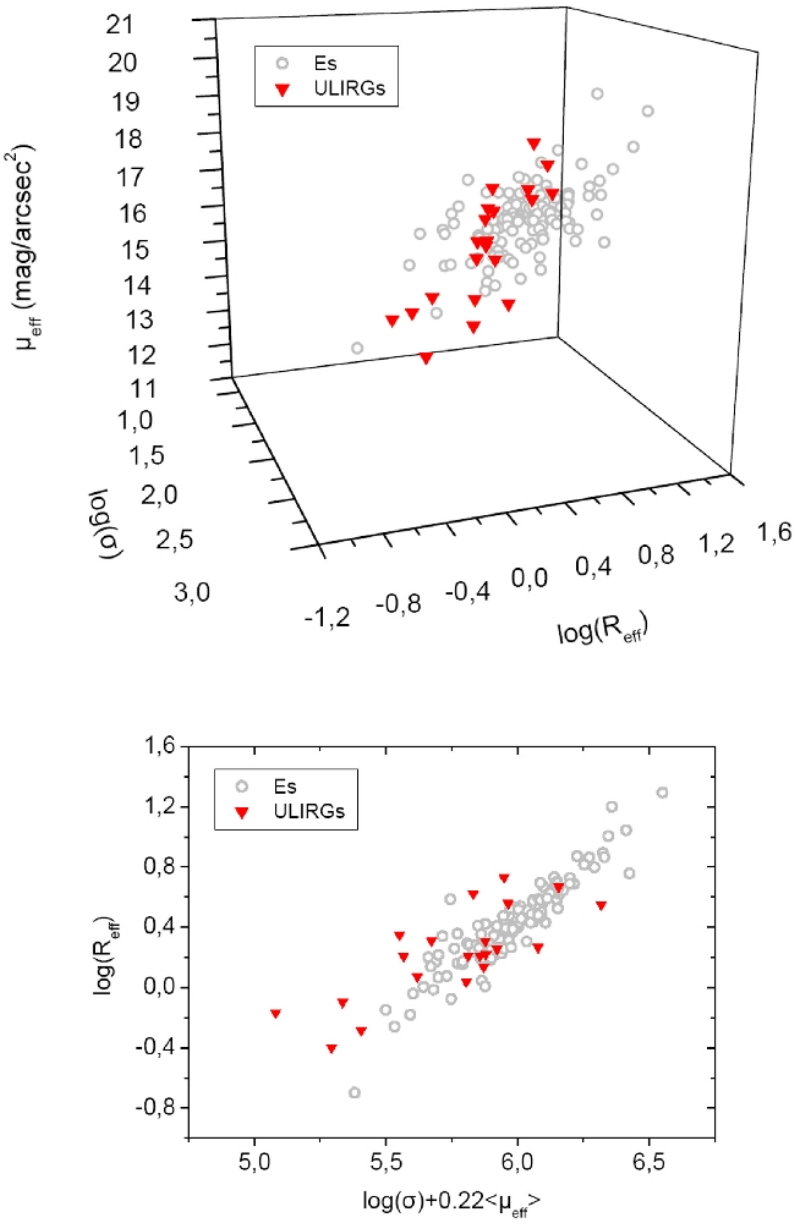

Figure 3.6: Upper panel: The 3-dimensional view of the H-band fundamental plane of early-type galaxies. Local early-type galaxies (mainly from the Coma and Virgo clusters) are plotted as open circles (Zibetti et al. 2002). ULIRGs are plotted as triangles. All data are PSF removed (see Table 3.2). No extinction corrections have been applied to the fluxes. Lower panel: The fundamental plane, viewed as in Pahre (1999).

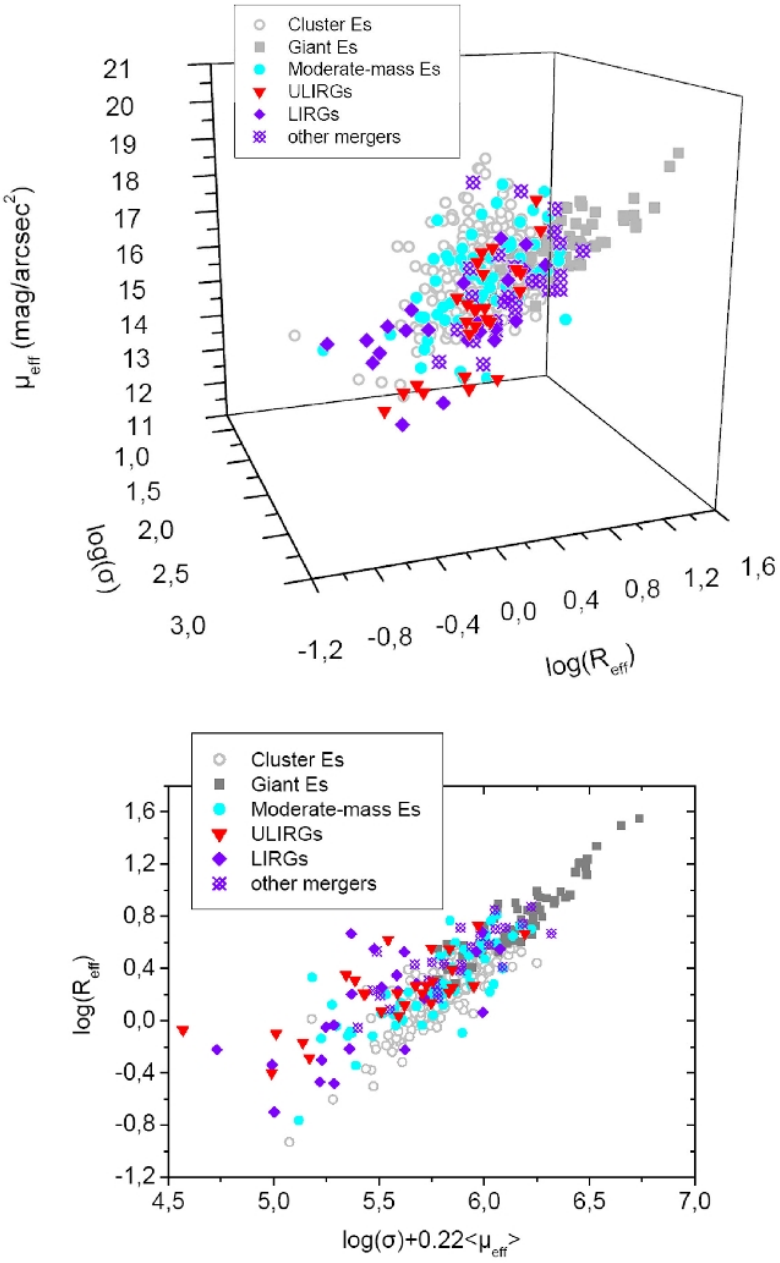

Figure 3.7: Upper panel: The 3-dimensional view of the K-band fundamental plane of early-type galaxies. The symbols used are identical to those in Fig. 3.5. A PSF estimate has been removed to all photometric data initially taken from Kim et al. (2002) (see Table 3.2). No extinction corrections have been applied to the data. Lower panel: The fundamental plane, viewed as in Pahre (1999).

In the H-band, the nuclear PSF removal has already been performed by Surace & Sanders 1999, Colina et al. 2001 and Veilleux et al. (2006) for most of the sources in our sample. For the sources taken from Scoville et al. (2000), we use the mean H-band ratio between the luminosity of the PSF-subtracted galaxy and the total luminosity, which equals 0.64 (Surace & Sanders 1999; Colina et al. 2001; Veilleux et al. (2006)). To construct the K-band 3-dimensional view of the fundamental plane, we use the total magnitudes[4] from Kim et al. (2002). In the K band, the value of the ratio between the luminosity of the PSF-subtracted galaxy and the total luminosity is 0.75 times that in the H band (Surace & Sanders 1999), therefore equals 0.48. We compute the mean surface brightness (within the effective radius) of each galaxy, $< \mu_{\rm gal} >$, by adding $2.5log(2\pi R^2_{\rm eff})$ mags (where $R_{\rm eff}$ is in $''$) to its PSF-subtracted magnitude in both bands. In Table 3.2 we tabulate the H and the K-band value of $< \mu_{\rm gal} >$ for each source.

In Fig. 3.6 (upper panel) we show the 3-dimensional view of the fundamental plane in the H-band. For viewing clarity, we also plot in Fig. 3.6 (lower panel) the fundamental plane in one of the representations introduced in Pahre (1999) (and used by Genzel et al. 2001). H-band data for (mainly cluster) Es are from Zibetti et al. (2002) and references therein. The ellipticals are plotted as open circles[5] and the ULIRGs as triangles. In the H-band, the individual PSF subtraction brings ULIRGs very close to the fundamental plane, indicating that ULIRG remnants will resemble Es once their on-going starbursts cease. That ULIRGs are on average somewhat brighter than Es is justified by the fact that a (diffuse) part of their starburst emission remains unremoved after the PSF subtraction. In Fig. 3.7 we show the K-band 3-dimensional view and Pahre (1999) visualization of the plane. In the K-band, ULIRGs lie again close to moderate-mass Es, after the statistical PSF removal. Along the photometric axis of the plane, PSF-subtracted ULIRGs are also close to LIRGs and other merger remnants.

We have not attempted to correct the photometric data (of any wavelength) for extinction effects; the value of the usually-assumed equivalent screen correction (Scoville et al. 2000; Genzel et al. 2001; Tacconi et al. 2002) is uncertain and changes after removal of the nuclear PSF. The application of an extinction correction will make the surface brightness of ULIRGs brighter. No k-corrections have been applied since they are negligible for the majority of the sources in our sample.

[4](magnitudes corresponding to a flux integrated up to the truncation radius of the galaxy)
[5]to enhance the clarity of the diagram we have excluded the dwarf Es, since they do not fall on the plane of all other Es

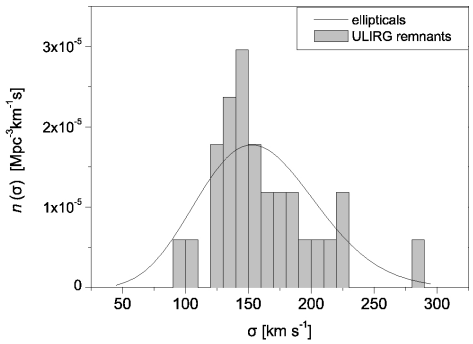

Figure 3.8: The number density of sources as a function of their stellar velocity dispersion is plotted in this figure. The solid line corresponds to the number density per σ of SDSS ellipticals, computed from their dispersion function (Sheth et al. 2003). The number density per σ of ULIRG remnants, plotted as a histogram, is calculated by multiplying the % fraction of our remnants that resides in each σ bin with the local volume density of ULIRGs from Sanders et al. (2003). To facilitate the comparison, the ULIRG histogram is further normalized so that its mean has the same number density as that of the elliptical $n(\sigma)$ distribution.

3.5.3 Discussion: The role of ULIRGs in the formation of Es

Our main conclusion from the fundamental plane analysis is that ULIRGs lie characteristically in the locus of local moderate-mass ellipticals of typical stellar mass of the order $10^{10} - 10^{11}\ M_{\odot}$. To further investigate the type of elliptical galaxy that ULIRGs form (at highest rates), we compare the number density of local ULIRG remnants and ellipticals as a function of their stellar velocity dispersion.

In Fig. 3.8, we plot the source number density per stellar dispersion in the range between 50 and 300km s^{-1} ; ULIRGs are plotted as a histogram and local SDSS ellipticals ($0.01 < z < 0.3$; Bernardi et al. 2003) as a solid line. For the ellipticals, $n(\sigma)$ is computed from the velocity dispersion function of Sheth et al. (2003). The $n(\sigma)$ distribution of ULIRGs is calculated by multiplying the % fraction of ULIRG remnants per σ bin with the (converted to our cosmology) volume density of ULIRGs (2.5×10^{-7} Mpc^{-3}) from Sanders et al. (2003). To facilitate the comparison between the two $n(\sigma)$ distributions, we apply a normalization factor of 7×10^3 to the ULIRG histogram so that its mean has the same number density as that of the SDSS ellipticals. Physically, this normalization factor is related to the ratio between the time over which ellipticals have been formed and the lifetime of a single ultraluminous burst.

Its value is only a rough estimate since it depends on the completeness of the 1 Jy and the SDSS (sub-)samples and the fact that ultraluminous mergers are not the only mechanism to produce elliptical galaxies.

The $n(\sigma)$ distribution of SDSS elliptical galaxies has a mean dispersion similar to that of ULIRGs, 157 (with a standard deviation of 54) km s^{-1} . In other words, the descendants of ULIRGs will resemble the ellipticals that are most common in the local Universe. Local ULIRGs seem to form at highest rates sources of characteristic σ between 130 and 160 km s^{-1} . That local Es are mainly produced by mergers of spirals of specific luminosities (or masses) is also found in the recent simulations of Kaviraz et al. (2006).

At low dispersions, the ratio between $n(\sigma)$ and $n(<\sigma>)$ seems to be lower for ULIRGs than for ellipticals. This deviation can probably be attributed to the fact that mergers of gas-rich galaxies below a certain mass threshold do not possess enough gas to undergo a ULIRG phase.

Deviations between the two distributions also exist at the high-dispersion end. For most bins at the high-dispersion end, the ULIRG distribution seems again underpopulated compared to that of SDSS ellipticals. We cannot formally rule out the possibility that the most massive ULIRGs have been missed either due to sample incompleteness, small volume densities, or possible shorter (than the average) burst timescales of the most massive sources. However, a case with high velocity dispersion, Mrk 273, has been observed in our sample. Even for Mrk 273, the total mass of the system (that also depends on its effective radius) is insufficient to classify it as a giant elliptical (of stellar mass $> 5 \times 10^{11} M_{\odot}$). Moreover, the fundamental plane analysis for all ULIRGs in our sample seems to suggest that ULIRGs do not account for the formation of (a significant fraction of) the giant elliptical galaxies in the local Universe. To quantify this, we perform a KS test to the ULIRG remnants and the (literature-selected) giant Es we used to construct the fundamental plane, acknowledging the different space-volumes they occupy. We find that the probability that ULIRG remnants and the giant ellipticals originate from the same population is extremely small (10^{-9}; see also Genzel et al. 2001; Rothberg & Joseph 2006).

To further assess how typically ULIRGs may form giant Es, we used the mass function of local Es to estimate what fraction f of the sources with mass $> 10^{10} M_{\odot}$ (mass threshold similar to that of ULIRGs) corresponds to giant ellipticals (of stellar mass $> 5 \times 10^{11} M_{\odot}$). Given that the fraction may significantly vary according to the adopted mass function, we used the best fit to the K-band mass function from various authors in the literature. Giant ellipticals comprise 18.7% of local Es with mass $> 10^{10} M_{\odot}$ for the mass function of Bell et al. (2003), found for Es in the Sloan Digital Sky (SDSS)

and the Two Micron All Sky (2MASS) surveys assuming a diet[6] Salpeter initial mass function (IMF). The fraction f is 20.1% for the 2MASS K-band luminosity function of local Es (Kochanek et al. 2001) which we convert to mass function using $m/L = 1.32\ M_{\odot}/L_{\odot}$ (Cole et al. 2001). This K-band m/L ratio is computed for both early- and late- type galaxies in the 2MASS and 2dF Galaxy Redshift Surveys, assuming a Salpeter IMF. An estimate of the m/L ratio for local ellipticals only can be derived from the work of Cappellari et al. (2005a) using the mean I-band m/L value and I-K color correction of the SAURON project sources. Combining the 2MASS K-band luminosity function with this early-type-galaxy m/L value ($0.75\ M_{\odot}/L_{\odot}$) yields f=10.9%. Although f is between 10% and 20%, we do not observe any source of $m > 5 \times 10^{11}\ M_{\odot}$ in our sample of 29 ULIRG remnants. This fact indicates that local giant ellipticals cannot be accounted for, if assumed to originate only from ultraluminous mergers.

One possible scenario for the formation of local giant Es is that most of these objects have formed at higher redshifts. This scenario is based on the fact that the more massive galaxies are, the faster and the earlier their stellar populations have formed (Thomas et al. 2005; van Dokkum 2005 and references therein). Tacconi et al. (2002) showed that local giant Es are mainly located in clusters whereas ULIRGs in the field, further reinforcing this scenario. Furthermore, other types of mergers (e.g. elliptical-spiral or elliptical-elliptical ones) account for the formation of most elliptical galaxies (Khochfar & Burkert 2003; Kaviraz et al. 2006) both at low and high redshift. Elliptical-spiral mergers enhance the star-formation activity already existing in one of the merging components and, for adequate amounts of gas, may appear as LIRGs. Gas-depleted elliptical-elliptical mergers (also known as "dry" mergers) are not easy to detect observationally (e.g, van Dokkum 2005; Bell et al. 2006) since they do not have unambiguous signatures such as luminous/ultraluminous phase(s) other than their perturbed morphologies; therefore, they can mainly be traced by visual identification. Dry merging is now believed to be a key element in the formation of local giant Es (Naab et al. 2006).

Rothberg & Joseph (2006) recently compiled a sample of local merger remnants selected by visual inspection. Such a sample probably comprised of merger remnants of all possible (S-S; E-S; E-E) categories. Rothberg & Joseph (2006) measured σ from Ca II triplet (optical) spectroscopy for 38 remnants, of which, 11 were LIRGs and 2 were ULIRGs. They found that the hypothesis that the LIRGs/ULIRGs in their sample and giant ellipticals can

[6] In this initial mass function, the number of low-mass stars is reduced leading to a total stellar mass reduced by 30%.

be drawn from the same parent population at a probability of 10%. Lake & Dressler (1986) also obtained optical velocity dispersion measurements for 13 merger remnants. Of those, 10 have Infrared Astronomical Satellite (IRAS) fluxes; no ULIRG exists in the sample of Lake & Dressler (1986) and only one source, AM 0921-225, is a LIRG[7]. Rothberg & Joseph (2006) computed the probability that the remnants of Lake & Dressler (1986) and giant Es originate from the same parent population and found it to be 5%.

The conclusion from the comparison of the optically-selected remnants of Rothberg & Joseph (2006) and Lake & Dressler (1986) with the IR-selected remnants in our study (and those of Genzel et al. 2001 and Tacconi et al. 2002) is what expected from theory: while galaxy mergers in general account for the formation of galaxies of various morphological classes and mass contents (e.g., Schweizer & Seitzer 1992; Springel & Hernquist 2005; Springel et al. 2005a), ultraluminous IR mergers in particular seem to have a very specific output (moderate-mass ellipticals) originating from their very specific input (sub-m_* spirals).

3.5.4 Wavelength Dependence Of The Stellar σ Measurement

Systematic differences between the measured and the actual values of the host dispersion can arise when extracting σ from different wavelengths, i.e. from the Ca II triplet in the optical (e.g. Rothberg & Joseph 2006) and the CO bandheads in the NIR. The host kinematics extracted from the NIR bandheads are often representative of young stellar populations. These populations could still be linked to the gas from which they formed (which is believed to settle into a disk early compared to the stars in the progenitor disks: Mihos & Hernquist 1996), and have less perturbed orbits than the old stars. Therefore, host dispersions extracted from the CO bandheads could be systematically lower than those of the merging bulges. The low $V_{\rm rot}/\sigma$ ratio that we measure for our ULIRGs is a good indication that even the young stellar populations are significantly heated, and therefore, systematics originating from NIR dispersion measurement are unlikely to have a major effect on our conclusions.

In the case of the Ca triplet, systematic errors are mainly related to the presence of dust. Due to scattering of light from dust particles, photons originating from high-velocity stars in the center of the galaxy will be scattered into random lines of sight. This will particularly bias the LOS velocity distribution at large radii where host dispersion is lower than that in the center

[7] We computed the IR luminosity of these sources with the formula of Sanders & Mirabel (1996) using mid-infrared fluxes from Moshir et al. (1990a), the Point Source Catalog (1988), and data given to the NASA Extragalactic Database in private communication

(Baes & Dejonghe 2002). The effects of dust in the observed stellar kinematics will further increase with increasing dust mass and extent (Baes & Dejonghe 2002). Since ULIRGs are highly obscured systems, dispersions extracted from the Ca triplet may be systematically higher than those of the stars in the central spheroid.

Such possible systematics have not been investigated in ULIRGs. Silge & Gebhardt (2003) have attempted to quantify the discrepancy between dispersion estimates derived from the NIR and the optical regimes for local quiescent galaxies. While they found no significant difference for elliptical galaxies, the systematics were non-negligible in S0 lenticulars, with the largest difference in σ ($\sim$30-40%) found in the most massive sources of their sample. The opposite conclusion can be derived from the velocity dispersion of ellipticals and Seyfert-type AGNs in Oliva et al. (1995) and Oliva et al. (1999). The σ values for the objects in their sample were systematically greater in the NIR than in the optical. The difference was large for type 1 Seyferts (up to a factor of 2) but low for type 2 Seyferts and ellipticals (<10%). Three LIRGs in the Rothberg & Joseph (2006) sample have been observed in the NIR by James et al. (1999) and Hinz & Rieke (2006). For these sources the systematics were negligible ($\leq$ 12km s^{-1}). On the other hand, the NIR results of James et al. (1999) and Hinz & Rieke (2006) are a factor of $\sim$2 higher than those of Shier & Fischer (1998), who have observed 2 of those 3 sources. It is therefore unknown whether the measurement of σ from the CO bandheads and the CaII triplet would systematically yield different results in the ULIRG stellar kinematics, and if yes, whether they would reflect real dynamic trends instead of measurement errors.

We investigate whether the use of the Ca II triplet for the measurement of σ may affect our results on the formation of (giant) Es under the hypothesis that the optical σ values can be indeed greater than the NIR ones due to population and extinction effects. We compute the maximum possible increase that can be applied to the dispersions of the sources in our sample, which is the maximum reported deviation (40%) in the results of Silge & Gebhardt (2003), which corresponds to an addition of $\sim$60 km s^{-1} in σ or a shift of 0.15 in the (logarithmic) horizontal axis of the fundamental plane. It is clear that this shift brings merger remnants closer to, but not at, the region populated by giant ellipticals. We also recompute the masses of the individual remnants in our sample after increasing their dispersion by 40%. The average mass is now 1.69×10^{11} $M_{\odot}$, which is again close to m_* and there is no source more massive than $5\times10^{11}M_{\odot}$. Therefore, our main conclusions are insensitive to the wavelength dependence of the stellar velocity dispersion measurement. Furthermore, the (not corrected for inclination effects) $V_{\rm rot}$(obs)/σ ratios of S0 lenticulars are typically greater than those of ULIRGs; e.g, for the combined

sample of Pizzela et al. (2005) and Cappellari et al. (2005b) the ratio is twice that of the remnants in our sample (0.6) indicating that deviations of the order 30-40% between the CO and Ca dispersion measurement are probably high for ULIRGs.

3.6 Black Holes in ULIRGs

3.6.1 A Picture Of The $M_{\rm BH}$-σ Relation Time Evolution

The size of a black hole seems to be closely linked to the depth of the potential well in which it forms and grows (Ferrarese & Merritt 2000). This is reflected i.e. in the local $M_{\rm BH} - \sigma$ relation, the correlation between $M_{\rm BH}$ and the stellar dispersion in the bulge of the host galaxy (Ferrarese & Merritt 2000; Gebhardt et al. 2000). Since the $M_{\rm BH} - \sigma$ relation is found for (virialized) bulge systems, it should be valid at the end of the merger process, when the bulge stellar kinematics have reached their final dynamical state and AGN winds and supernovae feedback have expelled the gas away from the nucleus, preventing further BH growth, terminating the starburst phase, and making the system resemble an elliptical galaxy. The merger remnants in recent simulations (Di Matteo et al. 2005; Springel et al. 2005b; Robertson et al. 2006a) are able to reproduce the $M_{\rm BH} - \sigma$ relation by subjecting a portion of their interstellar gas to accretion and feedback.

For ULIRGs however, the conversion of the host velocity dispersion into $M_{\rm BH}$ carries the uncertainty of applying the $M_{\rm BH} - \sigma$ relation to systems out of dynamical equilibrium. It is not yet known if, or to what extent, the $M_{\rm BH} - \sigma$ relation is valid between the first encounter and shortly ($\lesssim 10^8$ yrs) after the final coalescence, when most of the ultraluminous infrared activity occurs.

To investigate whether (and under which conditions) merging disk galaxies fall on the $M_{\rm BH} - \sigma$ relation during interaction phases prior to coalescence, we ran gas-rich merger simulations (details to be presented in Naab et al. 2006, in preparation) that have already been discussed briefly in Paper I. To include the effects of a dissipative component we replaced 10% of the stellar mass in the initial disks with isothermal gas at a temperature of approximately 10^4K. The initial scale length of the gas disk was equal to that of the stellar disk, h. Each galaxy had a stellar bulge with 1/3 of the disk mass and was embedded in a pseudo-isothermal halo to guarantee a flat rotation curve at large radii. All galaxies approached each other on nearly parabolic orbits with a pericenter distance of two disk scale lengths. The evolution of the stars and the gas was computed with the N-body smoothed-particle-hydrodynamics code VINE using an isothermal equation of state for the gas. For this study we analyzed

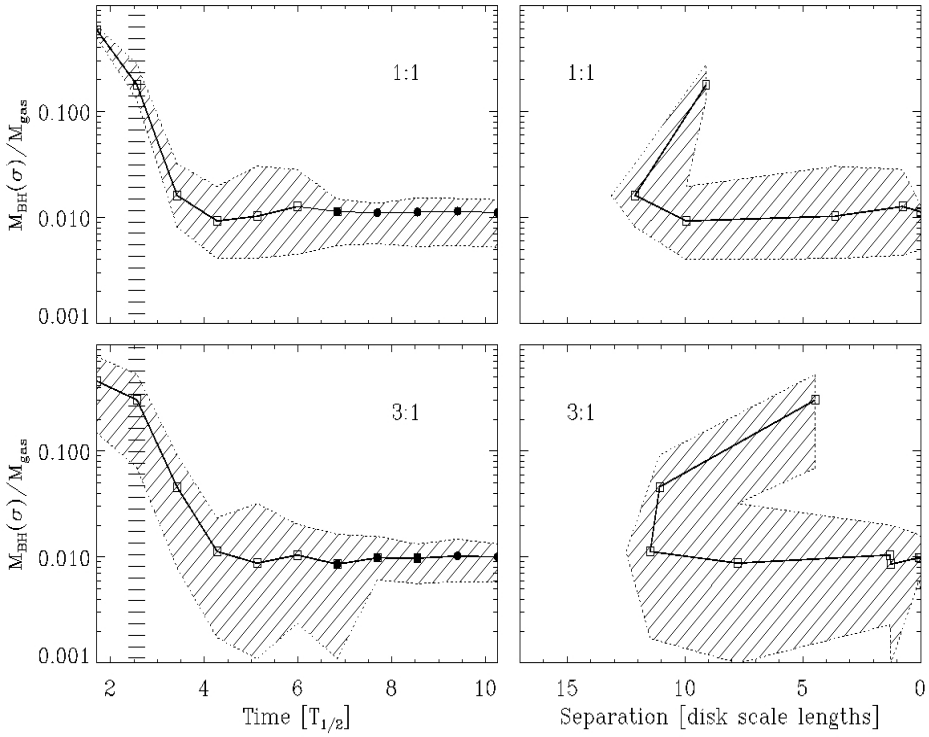

Figure 3.9: Evolution, during a disk-galaxy merger, of the average black-hole mass inferred from the central (line-of-sight) stellar velocity dispersion of the simulated galaxies. The black hole mass is in units of the average total accreted gas mass onto the center of the simulations. In the left column, the evolution is given as a function of time. Time is plotted in units of the half-mass rotation period, $T_{1/2}$, of the more massive progenitor disk. Open squares represent disks that are still separated, filled dots indicate fully merged systems. The spread originating from the initial disk orientations is indicated by the diagonally shaded area. The vertically shaded area indicates the first data point after the first encounter. In the right column, the evolution is plotted as a function of nuclear separation of the interacting galaxies. The nuclear separation unit is the disk scale length h of the more massive disk. We begin plotting data points for 1 step prior to first encounter, as in the left panels. We show 1:1 mergers in the upper and 3:1 mergers in the lower panels.

mergers with 16 different initial disk orientations (geometries 1-16 of Naab & Burkert 2003) and mass ratios 1:1 and 3:1.

We analyzed snapshots in the orbital plane approximately every half-mass rotation period of the more massive disk to follow the time evolution of the (projected) central stellar velocity dispersion and the gas accretion history onto the center of the system. At each snapshot, we calculated $M_{\rm BH}$ from the velocity dispersion assuming that the $M_{\rm BH} - \sigma$ relation is always valid. As in Paper I, we used the Tremaine et al. (2002) formula

$$M_{BH} = 1.35 \times 10^8 [\sigma/200]^{4.02} M_\odot \ , \tag{3.5}$$

where σ is in units of km s^{-1} , to calculate the black hole masses. To quantify the gas accretion, we computed the total gas mass $M_{\rm gas}$ that has ever reached a radius of $0.1h$ (i.e. twice the resolution element of the simulations) around the mass center of the system. By calculating the ratio between the quantities $M_{\rm BH}$ and $M_{\rm gas}$ we derive the accretion efficiency ϵ that is needed to maintain the black hole mass on the Tremaine et al. (2002) formula at any time. We define accretion efficiency ϵ as the fraction of the gas that accretes onto the black hole from the gas accumulated into the nuclear region.

In Fig. 3.9 we show the evolution of the accretion efficiency (needed to keep the black hole on the $M_{\rm BH} - \sigma$ relation) as a function of time (left column) and nuclear separation (right column). Time is given in units of the half-mass rotation period, $T_{1/2}$, of the more massive progenitor disk. The nuclear separation is given in disk scale lengths of the more massive disk. The efficiency is averaged over the 16 initial geometries for 1:1 and 3:1 mergers (upper and lower panels). The diagonally shaded area indicates the spread due to the varying initial disk geometries.

According to the left panels of Fig. 3.9, before nuclear coalescence, the estimated black hole mass and the gas accumulated at the center of the simulation already scale linearly. In other words, if we assume that the $M_{\rm BH} - \sigma$ relation is valid at *any* time during the merger, then the accretion efficiency remains constant shortly after the first encounter (shown in vertical dashes) until relaxation. Vice-versa, if we assume that the $M_{\rm BH} - \sigma$ relation is *only* valid at relaxation and that ϵ stays constant during the merger, then the black hole mass can be computed from the $M_{\rm BH} - \sigma$ relation from relaxation to mid-way to first encounter (when reading Fig. 3.9 backwards in time). Assuming that the $M_{\rm BH} - \sigma$ relation is valid at relaxation is reasonable since these remnants are to become elliptical galaxies.

The result of these simulations is that the $M_{\rm BH} - \sigma$ relation can be used to compute black hole masses in merging systems, from mid-way between first encounter and nuclear coalescence until the remnant becomes an elliptical galaxy, as long as ϵ remains constant. This is true for both equal- (1:1) and unequal- (3:1) mass major mergers. A constant efficiency ϵ conceptually

corresponds to subjecting a specific gas fraction to AGN feeding, an assumption also made for models that include star formation and ISM feedback (e.g. Springel et al. 2005b). However, it is likely that on short timescales (e.g. during specific accretion events) the efficiency ϵ may vary significantly. Therefore individual black hole estimates calculated from the $M_{\rm BH} - \sigma$ relation carry this uncertainty.

In the right panels of Fig. 3.9, the "folding" of the efficiency ϵ at large nuclear separations is due to the fact that the galaxies move towards apogalacticon before they fall back together. Clearly, at these merger phases, the use of the $M_{\rm BH} - \sigma$ relation is misleading. For a constant ϵ, the $M_{\rm BH} - \sigma$ relation begins to be valid beyond 5 disk scale lengths, which corresponds to a nuclear separation $\sim$7 kpc for our ULIRGs (see Paper I). If the assumption of a constant ϵ holds, the black hole estimates for $\sim 2/3$ of the binary sources are reasonable (but still lower limits on their actual values). For the ULIRG remnants, computing BH masses from stellar dispersions is justified. This is further supported by the fact that the kinematics of the latter are expected to have almost settled to their relaxation values (Mihos 2000).

3.6.2 Black Hole Sizes and Accretions Rates

We calculate the individual black hole masses of the sources in our sample using the Tremaine et al. (2002) formula and tabulate the results in Table 3.3. The mean black hole mass of the ULIRG remnants is $8.4 \times 10^7 M_\odot$. Since our sources are still in an ultraluminous IR emission phase, gas and dust are still present in the nuclear region and will continue accreting onto the black hole. However, beyond coalescence, the timescales for further gas accretion onto the black hole are probably shorter than those of the pre-coalescence staburst (e.g. Springel et al. 2005b). Therefore, the black hole masses of the fully relaxed systems will be somewhat larger than those presented in Table 3.3. Simple gas content (typical gas mass of ULIRGs is 5×10^9 $M_\odot$; Downes & Solomon 1998) and accretion efficiency (0.01, see § 3.6.1) arguments indicate that the additional increase of the remnant BH masses will not exceed 10^8 $M_\odot$ by the time the ultraluminous activity ends. In this order-of-magnitude calculation we have ignored the fact that only part of the gas reaches (or remains in) the center of the merging system, further reducing the upper limit on the black hole mass.

We calculate the BH mass each source would have, if it were accreting at the Eddington rate

$$L_{\rm Edd}/L_\odot = 3.8 \times 10^4 M_{\rm Edd}/M_\odot. \quad (3.6)$$

To calculate the Eddington BH mass $M_{\rm Edd}$, we assign to the Eddington lumi-

nosity $L_{\rm Edd}$ half of the luminosity emitted in the IR, given that some ULIRGs are largely starburst- while others are AGN- powered (Genzel et al. 1998; Rigopoulou et al. 1999; Veilleux et al. 1999; Joseph 1999; Sanders 1999). The Eddington efficiency $\eta_{\rm Edd}$, the ratio of the Eddington $M_{\rm BH}$ estimate over the dynamical black hole mass, is given in Table 3.3. The mean Eddington efficiency of the merged-ULIRG sample is 0.89, with a wide range of values. While statistically appropriate, the assumption that 50% of the IR luminosity originates from the AGN may make some sources appear as if accreting at super-Eddington rates (see Table 3.3). If we assign $\eta_{\rm Edd}$=1 for these sources and recalculate the average efficiency, we find it to be 0.47.

The inferred accretion rates may be higher than in reality if an overestimated fraction of the IR emission is assigned to the AGN. This could occur, if for example, the starburst is still the dominant source of the IR luminosity after the merging nuclei coalesce. The relative strengths of the starburst ($\rm L_{SB}$) and the AGN ($\rm L_{AGN}$) luminosity at each merger phase are uncertain. However, the MIR ISO spectroscopic study of local ULIRGs by Genzel et al. (1998) and Rigopoulou et al. (1999) indicates that most ULIRGs are starburst dominated systems, implying that probably less than 50% of the IR luminosity should be assigned to the AGN. Veilleux et al. (2002) have found that the strength of nuclear (continuum) emission increases with decreasing nuclear separation. Therefore, the Eddington efficiencies of the progenitors presented in Paper I may be systematically overestimated compared to those of the remnants. Future papers presenting SPITZER MIR spectroscopy of local ULIRGs will indicate the appropriate luminosity fraction that needs to be assigned to the AGN for ULIRGs before and after nuclear separation.

3.7 Conclusions

We have acquired NIR spectroscopic, long-slit, data of 54 ULIRGs at a variety of merger phases to trace the evolution of their host dynamical properties. From the analysis of the stellar kinematics in 29 ULIRG remnants, we find that:

1. Indications of an increase of the stellar random motions exist as the merger advances. The mean stellar σ, as measured from the CO rovibrational bandheads, equals 142 km $\rm s^{-1}$ for the binary sources (of mean nuclear separation 9.4 kpc, including IRAS 00456-2904 and IRAS 09111-1007) and 161 km $\rm s^{-1}$ for the remnants. This difference in the means of the pre- and post- coalescence distributions is marginally significant and requires more data to be accurately constrained. Furthermore, any increase of the stellar dispersion observed in ULIRGs corresponds to only

a part of the dynamical heating that occurs during the merger, since the merger timescales are longer than those of the ultraluminous starburst.

2. The dynamical and structural properties of the remnants indicate that they originate from mergers mainly of 1:1 and 2:1 progenitor mass ratios. This confirms what we found in Paper I by directly measuring the masses of the individual progenitors of binary ULIRGs.

3. Ultraluminous mergers will mainly lead to the formation of moderate mass ellipticals (of stellar mass $\sim 10^{11} M_{\odot}$). Depending on the definition of m_*, ULIRGs are between sub- and $\sim m_*$. ULIRGs are located in a region of the fundamental plane of early-type galaxies different from that of local giant Es, possibly indicating a different formation history for the latter. Local mass and dispersion functions support this argument; however, the current statistics cannot exclude the formation of few giant Es from ULIRGs.

4. We have performed simulations to investigate whether a black hole mass-host dispersion relation is appropriate for calculating the black hole masses of our ULIRGs. We find that already before nuclear coalescence, the mass of the gas that falls into the center of the merging system scales linearly with the black hole mass predicted by the $M_{\rm BH} - \sigma$ relation. However, this is only true if the efficiency of gas accretion onto the BH from its surroundings remains constant with time.

5. The black hole masses of the merged ULIRGs are of the order 10^7-$10^8 M_{\odot}$ and their accretion rates are high (Eddington efficiencies often > 0.5). If the AGN luminosity output of a ULIRG nucleus increases with time, our accretion rates in pre-coalescence ULIRGs may be overestimated relative to post-coalescence ULIRGs.

Acknowledgments:
We are grateful to N. Scoville for providing us H-band NICMOS imaging data for seven sources and D. C. Kim for frequently giving us prior-to-publication NICMOS photometric results for several sources. We would like to thank the ESO VLT staff for their support both in the service and visitor mode data acquisition. A. J. Baker acknowledges support from the National Radio Astronomy Observatory, which is operated by Associated Universities, Inc., under cooperative agreement with the National Science Foundation.

4

A scenario of QSO phases

...or... Host dynamics and origin of PG QSOs

K. M. Dasyra, L. J. Tacconi, R. I. Davies, R. Genzel, D. Lutz, B. M. Peterson, S. Veilleux, A. J. Baker, M. Schweitzer, E. Sturm, in preparation

Abstract

We present host dispersion velocities of 12 local (mainly Palomar-Green) quasars measured directly from the stellar CO absorption features in the H band. Our data were obtained with the ISAAC spectrometer on the Very Large Telescope. They constitute part of a larger program, QUEST, that aims to investigate whether the evolution of local Ultraluminous Infrared Galaxies is linked to that of quasars. We find that the mean bulge dispersion of the QSOs in our sample equals 186 km s^{-1} with a standard deviation of 24 km s^{-1} . The measurement of the stellar dispersion in QSOs enables us to place them on significant observational diagrams, such as the local black-hole mass and host-galaxy bulge relation and the fundamental plane of early-type galaxies. On the fundamental plane, PG QSOs are located between the regions that moderate-mass and giant ellipticals occupy. The QSO bulge and black hole masses, computed from the stellar velocity dispersions, are on an order of $10^{11} M_{\odot}$ and $5 \times 10^{7} - 10^{8} M_{\odot}$ respectively. The Eddington efficiency of their black holes is on average 0.25, assuming that all of the bolometric luminosity originates from the active nucleus. Our results suggest that Palomar-Green QSOs are related to galaxy mergers with gas-rich components and that they are formed in analogous manner with the most massive ULIRGs, regardless of their mid-infrared emission. However, they seem to have different host dynamics and formation

mechanisms than QSOs with supermassive black holes of $5\times10^8-10^9 M_\odot$ that accrete at low rates and reside in massive spheroids.

4.1 Introduction

In the current picture of galaxy formation and evolution, starbust and active-galactic-nucleus activity are believed to be closely linked to each other and to merger events (e.g., Haehnelt & Rees 1993; Hopkins et al. 2005). The link is believed to be the presence of gas which is indispensible both for initiating starbursts and feeding the AGN (e.g., Scoville et al. 2003; Evans et al. 2001; Greve et al. 2005 and references therein). However, the details of how mergers (of gas-rich galaxies) initiate both activities are not well understood, with the uncertainties mainly originating from our insufficient knowledge and treatment of the interstellar medium physics. Of such a nature is the debated question (e.g., Joseph 1999; Sanders 1999) whether quasar phases can be associated with Ultraluminous Infrared Galaxies[1]; Sanders & Mirabel 1996. Various scenarios have been expressed that relate QSOs and ULIRGs.

Sanders et al. (1988a) and Sanders et al. (1988b) suggested that after the nuclei of the merging galaxies coalescence, the IR emission arising from circumnuclear bursts and AGN-surrounding dust is strong enough for the system to reach QSO-like luminosities. Later in time, the dust and gas clear out from the nuclear region due to AGN winds and supernova feedback; then, the system goes through an optically bright phase before further accretion and star formation are finally prevented. According to these authors, all ULIRGs should eventually go through a QSO phase once their nucleus is revealed. It is, of course, possible that by the time the nuclear region is optically thin, the gas that remains there to fuel the AGN is not sufficient to make the latter shine as brigth as a QSO. Therefore, a more plausible scenario is that some ULIRGs may evolve into QSOs, depending on the amount of gas consumed during their early-merger stages. Various models have recently been published that are able to initiate a short (up to 10^8 yrs) QSO phase after the nuclear coalescence of gas-rich galaxy mergers (Di Matteo et al. 2005; Springel et al. 2005b; Hopkins et al. 2005; Cattaneo et al. 2005). The outcome of these simulations again depends strongly on the treatment of the interstellar medium.

Another scenario is that QSOs and ULIRGs do not necessarily follow each other on some evolutionary sequence, but they are both triggered under similar conditions (e.g., Canalizo & Stockton 2001). This assumption could hold, for example, if ULIRGs are triggered by major and QSOs by minor mergers of

[1] gas-rich mergers of infrared emission greater than 10^{12} $L_\odot$

gas-rich galaxies.

All the above-mentioned scenarios are based on the fact that ULIRGs have IR luminosities $> 10^{12}\,L_{\odot}$ and number counts similar to those of QSOs (Sanders et al. 1988a) in the Bright Quasar Survey (BQS; Schmidt & Green 1983) within the Palomar-Green (PG) catalog. Furthermore, PG QSOs have on average "warmer" IR spectral energy distributions (SEDs) than ULIRGs (Sanders et al. 1989), and some of them have host galaxies with signs of recent interaction (e.g. Surace et al. 2001). Evidence linking (so far) PG QSOs to mergers is summarized in Canalizo & Stockton (2001) and references therein.

Canalizo & Stockton (2001) have pointed out that the link between QSOs and ULIRGs needs to be sought by detecting starbursts in QSO host galaxies with the aid of spectroscopy. In the optical regime, spectra of the QSO host galaxy (or of star-forming regions in it) have been successfully modelled by Canalizo & Stockton (2001); however, no stellar kinematic information was extracted. The best-suited wavelength regime for the spectroscopy of stellar dynamics in QSO host galaxies is the near-infrared H band. The ratio of the host to the QSO photon counts is there maximum, dropping at both shorter and longer wavelengths due to increase in the AGN continuum emission. In the H and in the K band, Oliva et al. (1995) and Oliva et al. (1999) performed observations of young stellar populations in AGNs with luminosity mainly lower than that of QSOs, i.e. in Seyfert 1 AGNs.

We aimed to investigate the possibility that QSOs and ULIRGs are related by deriving the dynamics of the stellar populations that best trace recent starbursts in local PG QSOs and compare them to those of ULIRGs. For this purpose, we have carried out a European Southern Observatory large program[2] to acquire spectroscopic data for 54 ULIRGs (together with sources presented in Genzel et al. 2001 and Tacconi et al. 2002) and 12 QSOs. The ULIRG stellar kinematics have already been discussed in Dasyra et al. (2006a) and Dasyra et al. (2006b), hereafter Paper I and Paper II. In this paper, we present the host dynamics of (mainly) PG QSOs. These Very Large Telescope spectroscopic data constitute part of a larger project that aims to comprehend whether local ULIRGs and QSOs are related through near- and mid- infrared spectroscopy and imaging of their hosts; the program is called QUEST (*Quasar and ULIRG Evolutionary STudy*) and it is originally presented in Veilleux et al. (2006).

This paper is arranged as follows. We present our sample and briefly summarize the observations and data reduction techniques in § 4.2. The host and black hole (BH) properties of the QSOs in our sample (as inferred from the stellar dynamics) are given in § 4.3; the dynamical results for the PG QSOs

[2]PI Tacconi

are then compared to those of ULIRGs in § 4.4. We discuss the plausibility of a scenario that relates PG QSOs to gas-rich mergers and investigate the origin of local QSO populations in § 4.5. A summary is presented in § 4.6.

4.2 Observations and data reduction

4.2.1 Sample selection

To investigate how realistic evolutionary scenarios that associate ULIRGs with QSOs are, we need to select amongst the local QSOs that are believed to have the most active AGNs. This requirement is based on the high accretion rates of ULIRGs (e.g., Paper II). To meet this requirement, the Bright QSO sample of the Palomar-Green catalog (Schmidt & Green 1983) is best-suited; the point-like appearance, the U-B selection, and, mainly, the B-band magnitude threshold ($\lesssim$16 mag) of these sources favors the selection of the most active local AGNs (Jester et al. 2005).

The plethora of data available in the literature for PG QSOs allows for an optimum choice of the sample under examination. For example, measurements of the black-hole mass, $M_{\rm BH}$, have been performed for 19 PG QSOs by Kaspi et al. (2000) and Peterson et al. (2004). Approximately half of the sources in our sample were selected to have such a $M_{\rm BH}$ measurement. The remaining sources were chosen amongst the Surace et al. (2001) sample of so-called IR-excess QSOs. These are QSOs with strong mid- and far- infrared (MIR and FIR) emission compared to their optical luminosity; they are believed to be the QSOs that resemble the most to ULIRGs. Furthermore, we observed sources at redshift $z \lesssim 0.1$ to maximize the signal and facilitate the extraction of the host kinematics. The identifier, coordinates, redshift, and B-band magnitudes of the 11 sources selected and observed are given in Table 4.1.

Table 4.1: QSO List

Galaxy	RA [a] (2000)	Dec [b] (2000)	z	m_B (mag)	slit P.A. [c] (°)	$t_{\rm integration}$ [d] (mins)	$R_{\rm eff}$ (kpc)	m_H [e] (mag)
PG 0007+106	00:10:31.0	+10:58:30	0.0893	16.1 [f]	139,49	160,160	3.66 [i]	14.12 [i]
PG 0050+124	00:53:34.9	+12:41:36	0.0611	14.4 [f]	134,44	80,80	1.97 [i]	12.56 [i]
LBQS 0307−0101	03:10:27.8	-00:49:51	0.0804	16.3 [g]	44,134	120,120	...	...
PG 1119+120	11:21:47.1	+11:44:18	0.0502	15.4 [f]	89,179	80,80	1.39 [i]	13.22 [i]
PG 1126−041	11:29:16.6	-04:24:08	0.0600	15.4 [f]	154,64	110,105	4.21 [i]	13.26 [i]
PG 1211+143	12:14:17.7	+14:03:13	0.0809	14.4 [h]	0,89	130,130	2.57 [j]	14.38 [j]
PG 1229+204	12:32:03.6	+20:09:29	0.0603	15.5 [h]	29,119	140,110	5.12 [i]	13.00 [i]
PG 1404+226	14:06:21.8	+22:23:46	0.0980	16.5 [h]	45,135	120,120	7.15 [j]	14.38 [j]
PG 1426+015	14:29:06.6	+01:17:06	0.0865	15.7 [h]	60,-30	180,120	6.49 [j]	13.1 [j]
PG 1617+175	16:20:11.3	+17:24:28	0.1124	15.5 [h]	-1,89	120,110	2.43 [j]	14.98 [j]
PG 2130+099	21:32:27.8	+10:08:19	0.0630	14.7 [h]	-41,49	150,70	4.44 [i]	13.40 [i]
PG 2214+139	22:17:12.2	+14:14:21	0.0658	15.0 [f]	-1,89	120,120	3.97 [j]	13.67 [j]

[a,b] Units of right ascencion are hours, minutes and seconds, and units of declination are degrees, arcminutes, and arcseconds.
[c,d] Slit position angles and respective integration times per slit.
[e] The $H-$band mean surface brightness within the effective radius.
[f] Apparent magnitudes from Schmidt & Green (1983).
[g] Value taken from Chaffee et al. (1991).
[h] The (epoch-averaged) B-band magnitude is from Kaspi et al. (2000).
[i] NICMOS H-band data from Veilleux et al. (2006).
[j] NICMOS H-band data from McLeod & Rieke (1994a).

Table 4.2: Source IR fluxes and luminosities

Galaxy	$\log(\lambda L_\lambda[5100\dot{A}]/\mathrm{L}_\odot)^a$	f(12 μm)^b Jy	f(25 μm)^b Jy	f(60 μm)^b Jy	f(100 μm)^b Jy	$\log(L_{\mathrm{IR}}/\mathrm{L}_\odot)^c$	$L_{\mathrm{IR}}/L_{\mathrm{bb}}^d$
PG 0007+106	11.23	0.10	0.16	0.21	0.22^e	11.38	0.36
PG 0050+124	11.21	0.55	1.01	2.30	2.96	11.91	1.71
LBQS 0307−0101	...	...	...	...	...	...	...
PG 1119+120	10.55	0.12	0.28	0.55	0.75	11.13	0.70
PG 1126−041	10.80	0.11	0.31	0.67	1.17	11.34	0.68
PG 1211+143	11.17	0.17	0.30	0.31	0.67	11.55	0.38
PG 1229+204	10.50	0.12	0.30	0.16	0.53^f	11.16	0.60
PG 1404+226	10.80	<0.10	<0.10	<0.15	<0.35	<11.41	...
PG 1426+015	11.14	0.12	0.17	0.32	0.35^e	11.45	0.92
PG 1617+175	10.90	<0.07	<0.07	<0.10	<0.25	<11.37	0.31
PG 2130+099	10.88	0.19	0.38	0.48	0.62^g	11.41	0.58
PG 2214+139	11.08	0.06	0.10	0.34	<0.29	<11.04^h	0.30

[a] Optical luminosities taken from Peterson et al. (2004) or Vestergaard & Peterson (2006).
[b] All data are from Sanders et al. (1989) unless otherwise noted.
[c] Infrared luminosities calculated using the Sanders & Mirabel (1996) prescription from the MIR fluxes.
[d] Ratio of integrated IR over blue bump luminosity (see text for definition) from Surace et al. (2001) and Guyon et al. (2006).
[e] Infrared Space Observatory flux from Haas et al. (2003).
[f,g] Infrared Astronomical Satellite flux from Moshir et al. (1990a) and Moshir et al. (1990b).
[h] Lower limit for $\log(L_{IR}/\mathrm{L}_\odot)$ of PG 2214+139 is 10.99, when assigning f(100 μm)=0

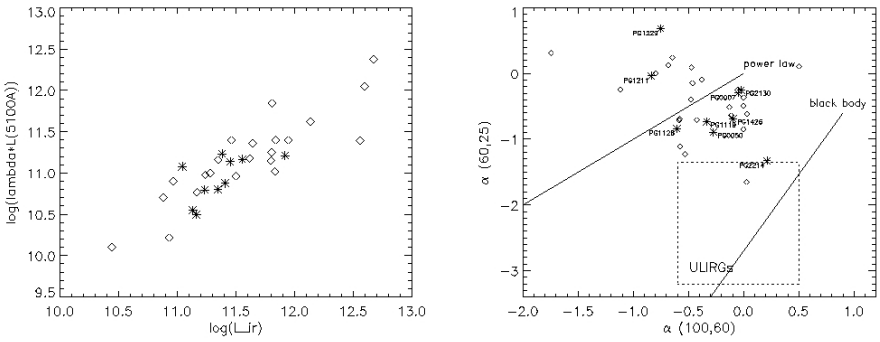

Figure 4.1: *Left panel:* The optical vs. IR luminosity of our sources. *Right panel:* The MIR color-index diagram used to identify possible transition objects between ULIRGs and QSOs (see Lípari 1994; Canalizo & Stockton 2001). The empirically determined position of ULIRGs on this diagram is indicated by a dotted box (Canalizo & Stockton 2001).
In both panels, all PG QSOs with MIR flux measurements are plotted as diamonds. The QSOs in our sample are plotted as asterisks. This diagram indicates that in terms of both optical and MIR/FIR properties, the QSOs in our sample are representative of the local PG population.

The whole range of AGN properties in local QSOs can be matched by compiling a sample that includes sources fainter than ∼16 mag in the B band. As a pilot attempt to extract host kinematics from such a source, we have observed a source from the Large Bright QSO Survey, LBQS 0307-0101 (Chaffee et al. 1991). This source is at a redshift representative of that of our entire sample, and according to Chaffee et al. (1991) has a B-band magnitude of 16.3. Unfortunately, the accuracy of the flux measurement with the photographic plates was low; Sloan Digital Sky Survey flux measurements yielded magnitudes of 15.92 and 15.77 respectively in the G and R bands. Since its actual B-band magnitude may not deviate from those of the entire sample, LBQS 0307-0101 does not require individual handling. Including this source, our sample comprises a total number of 12 local QSOs.

To investigate how representative our PG subsample is of the entire BQS PG population, we used the optical and MIR/FIR luminosities of our sources that we tabulated in Table 4.2. The optical luminosities $\lambda L_\lambda(5100\dot{A})$ are taken from Peterson et al. (2004) and Vestergaard & Peterson (2006). We computed the infrared luminosities L_{IR} from the 12, 25, 60, and 100 μm fluxes (of Sanders et al. 1989; Moshir et al. 1990a; Moshir et al. 1990b; Haas et al. 2003) using the Sanders & Mirabel (1996) prescription. The IR luminosity of all sources in our sample is greater than $10^{11}\,L_\odot$. This luminosity threshold is

similar to that of Luminous Infrared Galaxies[3]. In Table 4.2 we also present the ratio of the IR over the optical/ultraviolet luminosity of our sources from Surace et al. (2001) and Guyon et al. (2006). The latter is denoted as "blue bump" luminosity, $L_{\rm bb}$, and it is computed by integrating the luminosity per unit wavelength from $\sim$0.01 to 1 μm.

In Fig. 4.1, left panel, we plot the optical versus the infrared luminosity of PG QSOs. To construct this diagram, we used all QSOs of Peterson et al. (2004) and Vestergaard & Peterson (2006) that have an exact flux measurement [4] at 12, 25, 60, and 100 μm, either from Infrared Astronomical Satellite (IRAS) or from Infrared Space Observatory (ISO) data. We also used only PG QSOs at the redshift range of our QUEST project ($z \lesssim 0.3$). The PG QSOs of our sample are plotted as asterisks and all others as diamonds. Both the optical and IR luminosity of the sources in our sample are very close to those of the mean of the local PG QSO population. In Fig. 4.1, right panel, we plot the 60-25 μm versus 100-60 μm color index α diagram of local PG QSOs; the symbols used are identical to those of the left panel of Fig. 4.1. The MIR color indices of our sources are typical of all QSOs, indicating that the sample compiled is representative of the entire PG population.

4.2.2 Data acquisition and analysis

Our long-slit spectra were obtained with the ISAAC spectrometer (Moorwood et al. 1998) mounted on the Antu telescope unit of the ESO Very Large Telescope on Cerro Paranal, Chile. The QSO observations were typically performed in service and visitor mode under excellent seeing conditions (optical seeing of $\sim$0.″5-0.″6) to minimize the effects of AGN light diluting the host signal. The integration time for each exposure was 300 sec, to avoid saturation of the detector; the total on-source integration time varied from 160 to 320 mins. The slit width was 0.″6 and the detector scale 0.″146 per pixel (see Paper I). The central wavelength was in the $H-$band and varied from 1.70 to 1.77 μm, depending on the redshift z of each source and the wavebands of high atmospheric transmission. The spectral resolution $R = \lambda/\delta\lambda$ was equal to 5100. The slit position angles (PAs) and the respective integration time per PA are tabulated in Table 4.1 for the 12 sources observed. The redshift range of these QSOs ($0.050 < z < 0.112$) is on average lower than that of ULIRGs ($0.018 < z < 0.268$), and the integration times $\sim$2 times longer (on average), to ensure a high signal-to-noise (S/N) ratio of the host-galaxy signal.

For most of the QSOs in this study, the $H-$band effective radius $R_{\rm eff}$ and

[3] QSOs of $L_{IR} > 10^{12}\,L_{\odot}$ (that therefore can be classified as ULIRGs) are rather rare in the Palomar-Green catalog

[4] instead of an upper limit

mean surface brightness $\mu_{\rm eff}$ within it are measured from Hubble Space Telescope NICMOS imaging data (McLeod & Rieke 1994a; Veilleux et al. 2006). For some sources, NIR imaging data (assisted by adaptive optics) are also available by Guyon et al. (2006)[5]. The quantities $R_{\rm eff}$ and $\mu_{\rm eff}$ are given in Table 4.1, after being converted to the cosmology used in this paper (H_0=70 km s^{-1} Mpc^{-1}, Ω_m=0.3, $\Omega_{\rm total}$=1).

The data reduction tasks and procedures used to extract the host-galaxy spectra from the acquired ISAAC data can be found in Papers I and II, where they are presented in full detail. In the rest of this subsection, we mainly list the differences in the reduction method and the derived results between the ULIRG and the QSO data.

The main difference originates from the fact that photon counts associated with the AGN continuum are roughly one order of magnitude greater than those of the host galaxy, leading to a significant suppression of the stellar absorption features. For this reason, the (highly nucleated) AGN emission needs to be avoided for the accurate extraction of the stellar kinematics. To optimize the host S/N ratio per slit, we extract the spectra from the widest possible aperture (typically $\pm1\farcs0$-$1\farcs4$ from the center), excluding the very central region ($\pm0\farcs3$-$0\farcs4$). We then combine the results of the two slits into a single spectrum per object.

The method of extracting the stellar velocity dispersion σ from the reduced spectra is based on a Fourier correlation quotient technique (Bender 1990); the latter uses a template spectrum to provide the profile of the stellar kinematics along the line-of sight (LOS) to a galaxy (see Paper I). We fit a Gaussian to this kinematic profile to determine the projected stellar velocity dispersion. In contrast to Papers I and II where σ was measured from the central aperture, the stellar dispersion derived for the QSO hosts is typically measured from a radius of $\sim R_{\rm eff}/4$. In gas-rich merger remnants the velocity dispersion at the center and at the effective radius tends to deviate by $\sim$10% (Bendo & Barnes 2000). We ignore aperture effects since the expected deviations are typically whithin our error bars. No information on the rotation of the host galaxy can be obtained for the QSOs, given that rebinning of all spatial information is required to achieve the maximum possible S/N ratio.

We have observed four template stars for the extraction of the host dispersion velocity; an M0III giant (HD 25472), an M1Iab supergiant (HD 99817), a K5Ib supergiant (HD200576), and a K0Iab supergiant (HD 179323). The spectra of the first three stars are presented in Genzel et al. (2001). The K0I

[5]It is not possible to use our acquisition images to derive $R_{\rm eff}$, as we did in Papers I and II for the ULIRGs, since the photon counts in our short-exposure-time acquisition images are strongly dominated by the (point-like) AGN, leading to unrealistically small values for $R_{\rm eff}$.

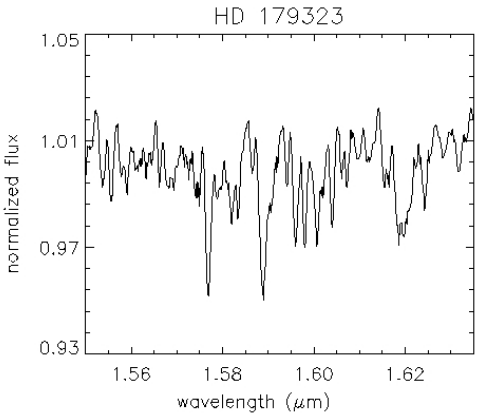

Figure 4.2: The H-band spectrum of the K0Iab supergiant HD 179323 that is used for the extraction of the stellar kinematics of some QSO hosts.

supergiant was observed with the integral-field-unit SINFONI on the VLT, which has a spectral resolution R=3000 in the H-band. The 2-d images were flat-fielded and converted into a wavelength-calibrated 3-d datacube using the C-language-based SINFONI datacube reduction package "SPRED" (Schreiber et al. 2004). After the extraction of the 1-d spectrum from the 3-d datacube, the stellar spectrum was sky-background subtracted and corrected for atmospheric absorption using a stellar telluric. The methodology followed for these corrections was identical to that applied for all sources in our program. The H-band spectrum of HD 179323 is presented in Fig. 4.2. From all available templates, we used the M0III giant and the K0I supergiant (or a linear combination of the two) since they provided the best description of the QSO-host spectra. The template used for each source is tabulated next to its dispersion in Table 4.3. The use of different stellar templates lead to σ measurements that deviate typically by 5 to 20%.

We plot the restframe spectrum of each QSO host galaxy in Fig. 4.3. For each source, we overplot the selected stellar template after convolving it with a Gaussian of dispersion equal to that measured. The spectrum shown in Fig. 4.3 is convolved to the resolution of the SINFONI observations for the sources that are best described by the K0I supergiant (or the combination of the K0I and the M0III templates).

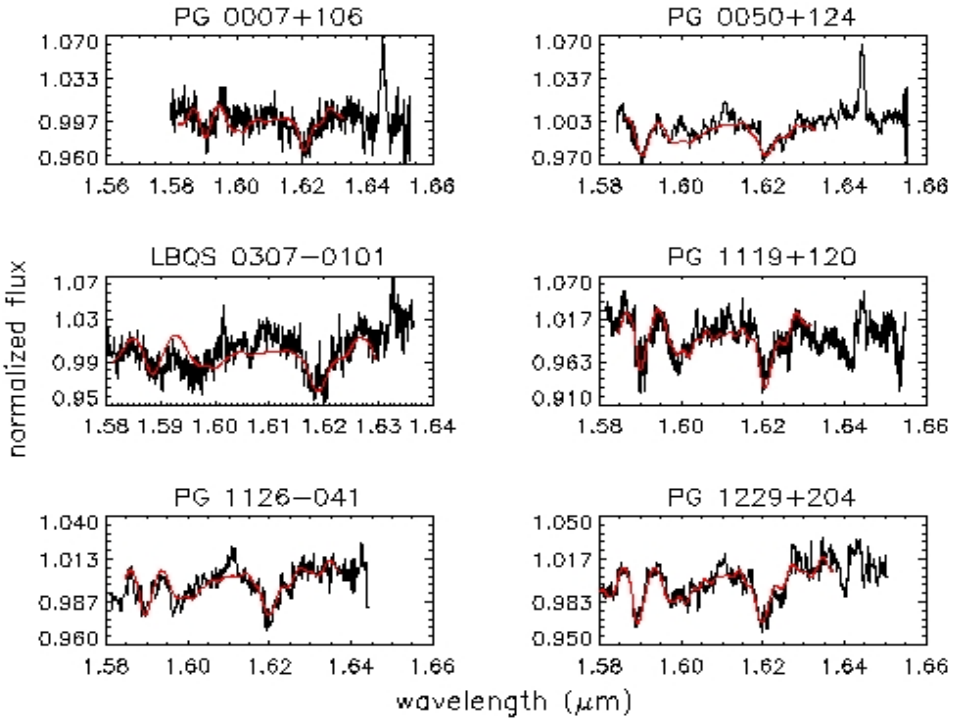

Figure 4.3: The H-band spectra of the QSOs in this study. The selected stellar template for each source is overplotted as a solid line after being convolved with the Gaussian that represents the LOS broadening function of the source. All spectra are shifted to the rest frame. The emission lines occasionaly seen at 1.611 μm and 1.644 μm correspond to Br 13 and [FeII] respectively.

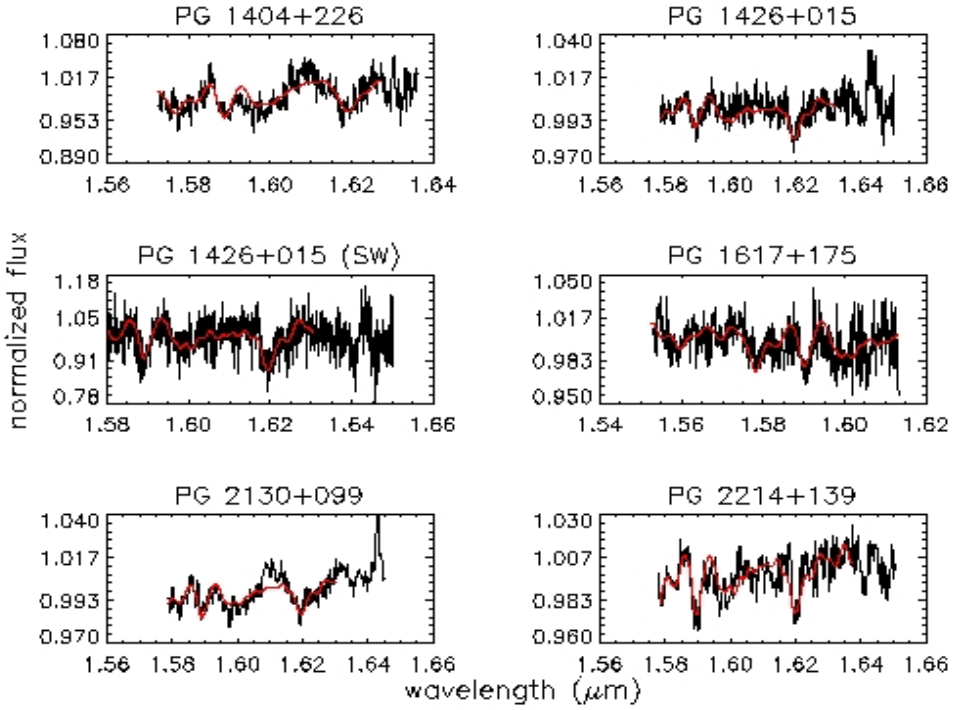

Fig. 4.3. — continued.

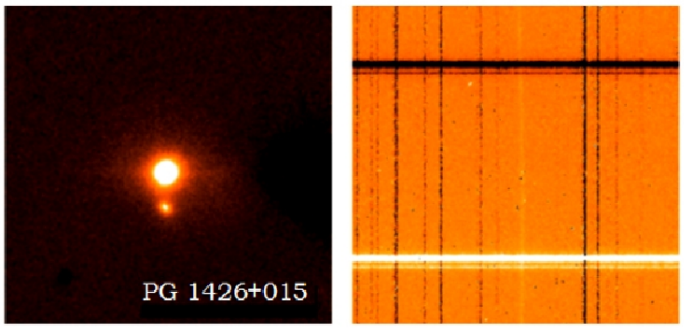

Figure 4.4: *Left panel:* The acquisition image of PG 1426+015 clearly shows that it is an interacting pair of 4.4 kpc nuclear separation. The QSO correspond to the NE nucleus.
Right panel: The spectrum of PG 1426+015 for a slit passing through both nuclei. This image shows the difference between two 10-min integrations at different detector positions; this technique is used to remove the sky lines. The number counts of the QSO spectrum are one order of magnitude greater than those of the faint nucleus. The velocity dispersion of the NE and the SW nucleus equal 185 (± 67) and 154 (± 27) respectively. km s^{-1} .

Table 4.3: Host dispersions, black hole masses and Eddington efficiencies

Source (PG)	σ (km s^{-1})	apert.[a] ($''$)	template star	$M_{\rm BH}$ [b] ($M_\odot$)	$M_{\rm BH}$(Edd.) [c] ($M_\odot$)	$\eta_{\rm Edd}$ [d]	$M_{\rm BH}$(rev.) [e] ($M_\odot$)	$M_{\rm BH}$(S.E.) [f] ($M_\odot$)
PG 0007+106	201 (± 81)	0.22-1.10	M0III	1.38×10^8	4.05×10^7	0.29	...	5.35×10^8
PG 0050+124	188 (± 36)	0.22-0.96	K0I	1.05×10^8	3.85×10^7	0.37	...	2.76×10^7
LBQS 0307−0101	207 (± 49)	0.22-0.96	M0III	1.55×10^8	...	...	...	...
PG 1119+120	162 (± 28)	0.22-0.96	M0III	5.79×10^7	8.39×10^6	0.14	...	2.95×10^7
PG 1126−041	194 (± 29)	0.22-1.10	K0I+M0III	1.19×10^8	1.50×10^7	0.13	...	5.61×10^7
PG 1211+143	...	...	...	...	3.48×10^7	...	9.14×10^7	...
PG 1229+204	162 (± 32)	0.22-1.25	K0I+M0III	5.79×10^7	7.44×10^6	0.13	7.32×10^7	...
PG 1404+226	237 (± 52)	0.22-0.96	K0I	2.67×10^8	1.48×10^7	0.06	...	7.74×10^6
PG 1426+015 [g]	185 (± 67)	0.22-1.10	M0III	9.87×10^7	3.25×10^7	0.33	1.30×10^9	...
PG 1617+175	183 (± 47)	0.37-1.40	M0III	9.45×10^7	1.87×10^7	0.20	5.94×10^8	...
PG 2130+099	172 (± 46)	0.22-0.96	K0I+M0III	7.36×10^7	1.79×10^7	0.24	4.57×10^8	...
PG 2214+139	156 (± 18)	0.37- 1.40	K0I+M0III	4.97×10^7	2.84×10^7	0.57	...	3.56×10^8

[a] The single-sided aperture within which σ was measured.
[b] Dynamical black hole masses estimated from their relation to the bulge dispersion (Tremaine et al. 2002).
[c] Eddington black hole mass, calculated by attributing *all* of $L_{\rm bol}$ to the AGN (L_{Edd}).
[d] Ratio of Eddington over dynamical black hole mass.
[e] Reverberation black hole masses from Peterson et al. (2004).
[f] Single-epoch, virial black hole masses from Vestergaard & Peterson (2006).
[g] The velocity dispersion of the SW (stellar-light-dominated) component of this interacting system is 154 (± 27) km s^{-1} ; it is derived using the M0III giant.

The error bars on the measured value of σ are in some cases $\gtrsim$ 50 km s^{-1} due to an artificial template mismatch caused by the strong dilution of the host-galaxy spectrum into the AGN continuum. This dilution may affect the velocity dispersion measurement since it alters the shape of the wings of the stellar absorption features. To quantify this effect, we have constructed artificial QSO ISAAC data from which we measured the bulge velocity dispersion as we did for the real data. We convolved the spectrum of our stellar template with a Gaussian of σ =200 km s^{-1} . We scaled its photon counts to those of a $<\mu_{\rm eff}>=$ 16.5 de Vaucouleurs bulge at $z = 0.076$ that fall in our 0.″6 slit. We diluted this host-galaxy signal with a continuum the strength of which is determined by counting the photons that fall in the slit and originate from a point source of 13.3 apparent magnitude (Veilleux et al. 2006) under 0.″6 seeing conditions. After adding Poissonian noise, we extracted the bulge dispersion and found it equal to 176 km s^{-1} with a standard deviation of 41 km s^{-1} . Therefore, strong absorption-line dilution may result in velocity dispersions smaller by ∼15% than in reality. In addition to this, any weak lines (e.g. at the 0.1% continuum levels) intrinsic to the telluric star we used to correct for the atmospheric absorption (see Paper I) may also affect our spectra, since the stellar continuum is roughly at the 10% level of the AGN emission.

The S/N ratio was insufficient for the detection of stellar absorption from the host galaxy of PG 1211+143, possibly due to a very strong dilution of the host-galaxy light by the AGN continuum. PG 1426+015 is an interacting galaxy with two components. The data for both the QSO and the secondary, south-west (SW) nucleus are presented here (see Figs. 4.3, 4.4), while a detailed discussion on this source can be found in § 4.5.1.

4.3 Results

4.3.1 Host-galaxy dynamical properties

The stellar velocity dispersion of all QSO host galaxies is presented in Table 4.3. The dispersion of the SW nucleus of PG 1426+015 (which is not a QSO) is excluded from all statistical analyses of this paper. The mean value of σ is 186 km s^{-1} , with a standard deviation of 24 km s^{-1} and a standard error (uncertainty of the mean) of 7 km s^{-1} . Most of the sources of Table 4.3 with $\sigma <$ 200 km s^{-1} , show spiral structure or tidal tails (PG 0050+124, PG 1119+120, PG 1126-041, PG 1229+204, PG1426+015, PG 2130+099) in their NIR images (Surace et al. 2001; Veilleux et al. 2006).

For a stellar system characterized by a dispersion velocity σ, the total

(bulge) mass is computed from

$$m = 1.40 \times 10^6 \sigma^2 R_{\rm eff}, \tag{4.1}$$

where σ is in units of km s^{-1} , $R_{\rm eff}$ is in kpc and m is in $M_\odot$ (see Tacconi et al. 2002; Paper II). Using this formula we find that the mean bulge mass of all QSOs in our sample is 1.92×10^{11} $M_\odot$. This result implies that the hosts of PG QSOs are $\sim 1.5 m_*$ galaxies, for $m_* = 1.4 \times 10^{11}$ $M_\odot$ (see Genzel et al. 2001, Paper II, and references therein).

In Fig. 4.5 we place our QSOs on the K-band fundamental plane (FP) of early-type galaxies (Djorgovski & Davis 1987; Dressler et al. 1987) using the host effective radii and mean surface brightnesses from Veilleux et al. (2006) and McLeod & Rieke (1994a) tabulated in Table 4.1. We converted H- into K- band host magnitudes using the mean Two Micron All Sky Survey (2MASS) mean $H-K$=0.3 color index correction (Jarrett et al. 2003)[6]. The data for the early-type galaxies are taken from Bender et al. (1992), Faber et al. (1997), and Pahre (1999) and converted to our cosmology. Giant boxy ellipticals (squares) are located on the upper-right part of the fundamental plane $R_{\rm eff}$-σ projection, while moderate-mass ellipticals (circles) occupy the central and the lower-left parts (see Fig. 4.5, left panel). PG QSO hosts (stars) lie between moderate-mass and giant Es (but still closer to the former) both in the $R_{\rm eff}$-σ projection that relates the dynamical properties of the systems (upper panel) and in the 3-dimensional plane that takes into account their photometric properties (middle and lower panels).

Other optically-faint QSOs that are hosted mainly by giant Es (Dunlop et al. 2003) are also plotted in Fig. 4.5 (asterisks). The velocity dispersion of their host galaxies does not originate from a direct measurement; it is inferred from their black-hole masses using the Tremaine et al. (2002) relation (see also § 4.3.2). Prior to this computation, we recalculated the black hole masses of the sources in Dunlop et al. (2003) using the Haering et al. (2004) black hole - stellar spheroid mass relation. The host dynamical properties of these QSOs are systematically higher than those of PG QSOs, although there is a small overlap between the locii of the two populations (see also § 4.5.2).

4.3.2 Black hole properties

We compute the black hole masses of the QSOs in our sample from their relation to the stellar velocity dispersion in the bulge, known as the $M_{\rm BH} - \sigma$

[6] we do not discriminate between elliptical or spiral hosts since the difference is small for the 2MASS galaxies and since the hosts of some of our QSOs show patterns of spiral structure (e.g. Surace et al. 2001; Guyon et al. 2006)

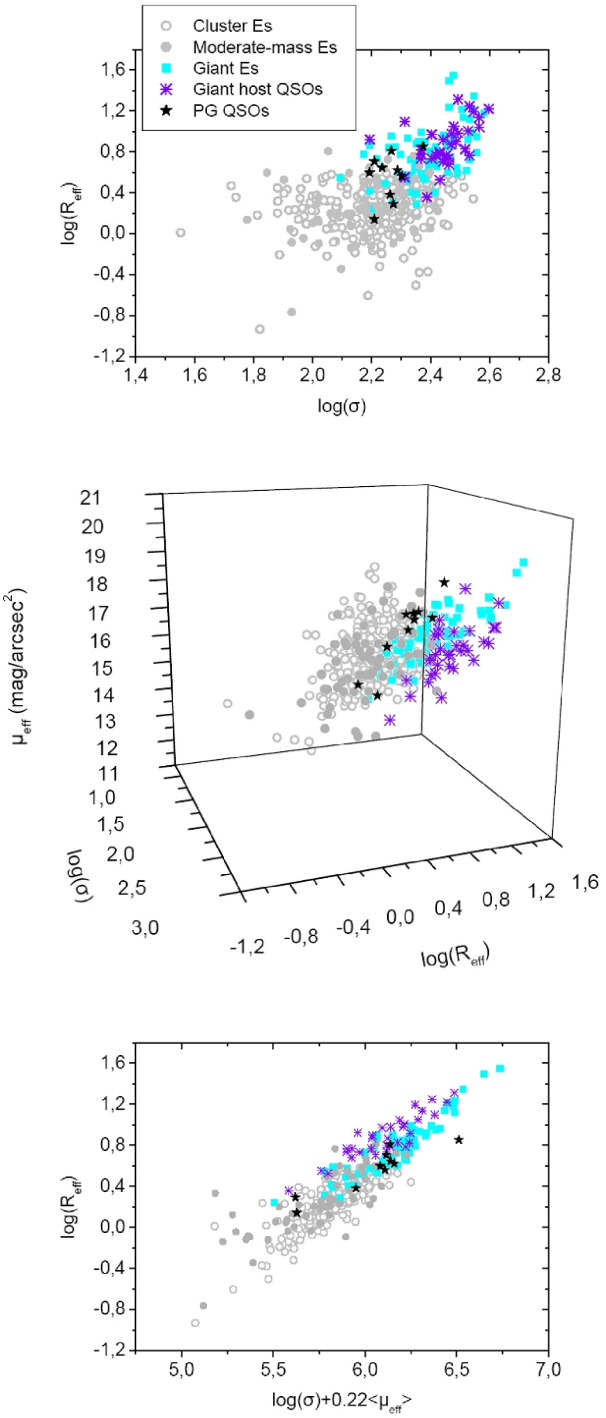

Figure 4.5: The K-band fundamental plane of early-type galaxies. *Upper panel:* The dynamical $R_{\rm eff}$-σ projection of the plane. *Middle panel:* The 3-d view of the plane *Lower panel:* The Pahre (1999) projection of the plane plotted for viewing clarity. In all panels, giant boxy and moderate-mass disky Es (squares and circles respectively) are from Bender et al. (1992) and Faber et al. (1997). More (cluster) Es (open circles) are from Pahre (1999). The QSOs of this study as plotted as stars and the QSOs of Dunlop et al. (2003) as asterisks.

relation (Gebhardt et al. 2000a; Ferrarese & Merritt 2000). For this purpose, we use the Tremaine et al. (2002) formula,

$$M_{BH} = 1.35 \times 10^8 [\sigma/200]^{4.02} M_\odot \ , \tag{4.2}$$

as in Papers I and II. The application of the $M_{\rm BH} - \sigma$ relation yields an average black hole mass of 1.12×10^8 $M_\odot$ (see Table 4.3).

The $M_{\rm BH} - \sigma$ relation was originally established for local quiescent ellipticals in which the black hole masses were primarily determined from stellar, gas, or maser kinematics (see Gebhardt et al. 2000a, Ferrarese & Merritt 2000 and references therein). It was subsequently shown that a similar relationship exists in low-luminosity AGN (type 1 Seyferts; Gebhardt et al. 2000; Ferrarese et al. 2001; Nelson et al. 2004; Onken et al. 2004). In the case of AGN, the black hole masses were measured from reverberation mapping experiments (Kaspi et al. 2000; 2005; Peterson et al. 2004; Vestergaard & Peterson 2005) Reverberation-mapping techniques (Blandford & McKee 1982; Peterson 1993) use the kinematics of broad-line-region (BLR) gas to compute BH masses, assuming that the BLR is virialized. In this case, $M_{\rm BH} \sim fR\Delta V^2$, where R is the size of the BLR as measured by the time delay between continuum and emission-line variations, ΔV is the emission-line width, and f is a scaling factor that describes (and depends upon) the structure and inclination of the BLR. The mean value of f, 5.5 (Onken et al. 2004), is statistically determined by assuming that the $M_{\rm BH} - \sigma$ relation is the same in both active and quiescent galaxies. According to Vestergaard & Peterson (2005), the use of a statistical value for f leads to black hole mass estimates that appear to be accurate to a factor of ~ 3. However, on individual cases the actual error bar values may strongly depend on the inclination of the BLR (Collin et al. 2006).

Reverberation BH masses are available in the literature (Peterson et al. 2004) for four of the QSOs in our sample that have a host dispersion measurement (see Table 4.3). In the case of PG 1229+204, there is a good agreement between the dynamical and the reverberation black hole measurement. However, there is a trend for the average dynamical black hole mass of all four sources to be smaller (by a factor of 7) than that computed from reverberation experiments. This trend is better illustrated in Fig. 4.6 where we place PG QSOs on the $M_{\rm BH} - \sigma$ relation. We plot the QSOs (stars) over the quiescent galaxies (triangles) of Tremaine et al. (2002) and Ferrarese & Merritt (2000) and over the AGNs (circles) of Onken et al. (2004) and Nelson et al. (2004)[7]. We use the black hole estimates that are directly derived from the virial techniques; for the AGNs, these masses are identical to the quotient

[7]For the sources with two σ measurements we use the average of the two.

$M_{\rm BH}/f$. This formalism helps avoiding uncertainties that originate from the inaccurate knowledge of the factor f that describes the BLR geometry. The solid and dashed lines correspond respectively to the Tremaine et al. (2002) and Ferrarese (2002) fit to the data of quiescent ellipticals. We find that the 4 reverberation-mapped QSOs lie on the relation of quiescent galaxies, above the locus of Seyfert 1 AGNs with similar dispersions.

This result may reflect realistic differences in the host and AGN properties of low- and high- mass AGNs. For example, supermassive black holes of $\gtrsim 10^8$ $M_\odot$ may be hosted on bulges less massive than those predicted by the current best fit to the low-luminosity AGN data [8]. It may also be attributed to an evolution of the $M_{\rm BH}-\sigma$ relation with z (Woo et al. 2006); however, this scenario is less probable given the small redshift difference between the QSOs in our sample and the Seyfert 1 AGNs in Onken et al. (2004) and Nelson et al. (2004). Deviations on the location of the various AGN types in Fig. 4.6 may also be caused by factors such as small number statistics or possible systematic errors in the measurement of σ (e.g. from population effects).

Stellar population effects appear when using NIR velocity dispersion measurements to place QSOs on the AGN $M_{\rm BH}-\sigma$ relation, which is originally constructed using optical σ values. Silge & Gebhardt (2003) attempted to trace and quantify systematic discrepancies between CO and various optical dispersion measurements on a sample of 17 S0 lenticular and 7 elliptical galaxies. The systematic differences between the NIR and optical σ values were negligible for the elliptical galaxies. For the lenticular galaxies, the NIR values were typically 10 % smaller than the optical ones, and the discrepancies were most prominent (up to 30-40%) in the most massive sources. The opposite conclusion can be derived for some of the Seyfert 1 AGNs in Onken et al. (2004) that have been observed in the $H-$ and $K-$ band by Oliva et al. (1995) and Oliva et al. (1999); for most of the sources the host dispersion in the NIR was greater (by up to a factor of 2) than that in the optical. For ellipticals and Seyfert 2 AGNs, the systematics were smaller (<10%). However, the Oliva et al. (1995) and Oliva et al. (1999) results may reflect the low resolution of their spectra, which was equal to 1600 and 2500 in the $H-$ and $K-$ band respectively. While it cannot be disregarded as a possible source of uncertainty, the measurement of σ from different wavelengths is neither properly quantified nor confirmed to reflect real differences in the kinematics of the various stellar populations. Further data are required to confirm or quantify such effects.

To investigate whether our result is an artifact of small-number statistics,

[8] That is either the Tremaine et al. (2002) or the Ferrarese (2002) function, divided by the mean value of f, 5.5, to scale with the AGN datapoints.

we check how well the host dispersions of 10 QSOs in our sample that have indirect $M_{\rm BH}$ estimates from the literature fit the $M_{\rm BH} - \sigma$ relation. The $M_{\rm BH}$ estimates are derived from single-epoch-flux measurements. Instead of monitoring continuum and emission-line flux variations to infer the size of the BLR, single-epoch techniques use reverberation-based relations that connect the optical/ultraviolet luminosity and the various emission-line fluxes to the radius of the system (Kaspi et al. 2000; 2005; Vestergaard 2002). Using such scaling relations, Vestergaard & Peterson (2006) have recently provided $M_{\rm BH}$ sizes for PG QSOs without reverberation $M_{\rm BH}$ estimates. Of those, we use the values computed from the width of the H_β line and the $5100\dot{A}$ luminosity. According to Vestergaard & Peterson (2006), the statistical 1-sigma uncertainty in these mass estimates corresponds to 0.52 dex or a factor of 3.3; we use this 1-sigma uncertainty as the most plausible error in the estimate of $M_{\rm BH}$ as we do for our dispersion measurements. We note, however, that in individual cases, the error in $M_{\rm BH}$ may actually be of an order of magnitude.

In Fig. 4.7, we plot the 10 PG QSOs (stars) with single-epoch $M_{\rm BH}$ estimates over the Seyfert 1 AGNs of Onken et al. (2004) and Nelson et al. (2004) (circles). We also overplot the $M_{\rm BH} \sim 10^6 M_\odot$ AGNs of Barth et al. (2005) (triangles) to simultaneously study the behaviour of the relation at its high- and low- mass end. The black hole masses used in this figure equal their virial value times the factor f, since this factor was incorporated in the calibration of the single-epoch scaling relations. We find that the relation that connects the the bulge dispersion to the black hole mass is indeed global, applying to AGNs with $M_{\rm BH}$ from 10^6 to 10^9 $M_\odot$. Both at the high- and at the low-mass end of the relation, there is a small and comparable offset between the single-epoch and the dynamically-predicted value of $M_{\rm BH}$; $< \delta \log[M_{\rm BH}] >$ is 0.15 and $\sim$0.25 for this and the Barth et al. (2005) samples respectively. This offset indicates that the difference in the location of quiescent galaxies and AGNs on this relation may be smaller than it was thought to be, implying a factor f smaller than 5.5. We also find that the QSO datapoints are now scattered more homogeneously than in Fig. 4.6 around the best-fit functions. Therefore, it is likely that the result found for the 4 reverberation-mapped QSOs is partially affected by small number statistics; the measurement of σ on larger samples of reverberation-mapped is a crucial step prior to the presentation of a new best fit to the AGN data.

To estimate at what rates our sources accrete, we calculate their Eddington black hole masses, M_{BH}(Edd), from their Eddington luminosities, $L_{\rm Edd}$, as

$$L_{\rm Edd}/L_\odot = 3.8 \times 10^4 M_{\rm BH}({\rm Edd})/M_\odot. \quad (4.3)$$

We consider that all of the QSO bolometric luminosity comes from their active nucleus (in contrast to Paper I and Paper II where we assigned half of the

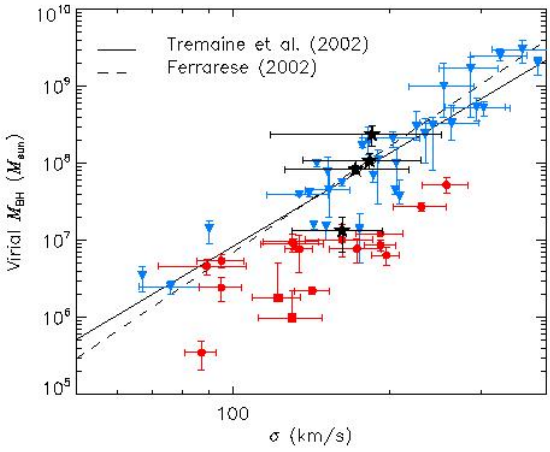

Figure 4.6: The local $M_{\rm BH} - \sigma$ relation for quiescent galaxies and AGNs with direct $M_{\rm BH}$ measurements. For the AGNs (including the PG QSOs), the virial black-hole masses are equal to the quotient $M_{\rm BH}/< f >$ of the reverberation experiments (Peterson et al. 2004). The quiescent galaxy datapoints (Tremaine et al. 2002; Ferrarese & Merritt 2000) are plotted as triangles and the Seyfert 1 AGNs of Onken et al. (2004) and Nelson et al. (2004) are circles. Few low-luminosity AGNs with upper limits on their $M_{\rm BH}$ values are plotted as squares. The QSO datapoints are shown an stars. The solid and the dashed lines correspond to the laws that fit the quiescent galaxy data (Tremaine et al. 2002 and Ferrarese 2002 respectively).

infrared luminosity of ULIRGs to $L_{\rm Edd}$). We compute the bolometric from the optical luminosity (see Table 3.1) as

$$L_{bol} = C * \lambda L_{\lambda}(5100\dot{A}), \tag{4.4}$$

where the conversion factor C is ~ 9 (Kaspi et al. 2000). The value of C may significantly differ from one QSO to another; therefore, the accuracy of its mean is rather small (within a factor of 3; Elvis et al. 1984; Sanders et al. 1989; Netzer 2003). The estimated Eddington accretion efficiencies, $\eta_{\rm Edd} \equiv M_{\rm BH}({\rm Edd})/M_{\rm BH}$, carry this uncertainty. Furthermore, since a part of the emission is originating from the host, the values of $\eta_{\rm Edd}$ given in Table 4.3 should be treated as upper limits. The mean Eddington accretion efficiency of the QSOs in our sample is 0.25, in good agreement with McLeod et al. (1999).

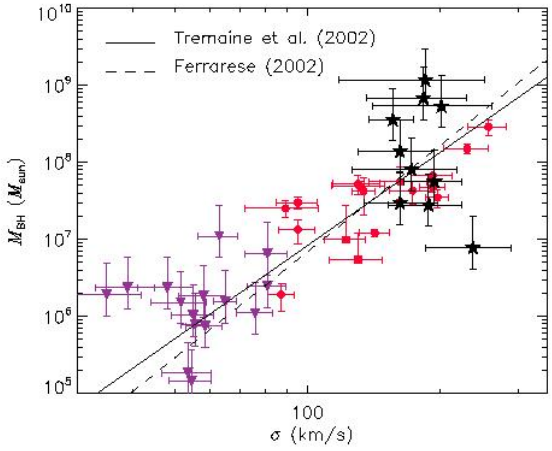

Figure 4.7: The AGN $M_{\rm BH} - \sigma$ relation studied at its high- and low- mass end using indirect, single-epoch, $M_{\rm BH}$ estimates for local PG QSOs (Vestergaard & Peterson 2006) and low-mass AGNs (of $M_{\rm BH} \sim 10^6$; Barth et al. 2005). In contrast to Fig. 4.6, the black hole masses used in this figure equal their virial value times the factor f. The symbols for the Seyfert 1 AGNs of Onken et al. (2004) and Nelson et al. (2004) and the PG QSOs of this study are identical to those used in Fig. 4.6. The low-mass AGNs are plotted as triangles. The solid and the dashed lines correspond to the Tremaine et al. (2002) and Ferrarese (2002) laws.

4.4 ULIRG vs. (IR-excess) PG QSO dynamics

To properly investigate whether QSOs and ULIRGs may be related, it is of particular importance to establish a solid classification method for the QSOs with IR-excess emission and compare the dynamics of the latter to those of ULIRGS. Several criteria have been used in the literature to identify IR-excess QSOs (see Sanders et al. 1989, Surace et al. 2001, Lípari 1994, Canalizo & Stockton 2001, and references therein). Some were based on 60 μm and 25/60 μm flux thresholds. Sanders et al. (1989) and Surace et al. (2001) defined IR-excess QSOs to be these sources with $L_{\rm IR}/L_{\rm bb} > 0.46$. Lípari (1994) and Canalizo & Stockton (2001), among others, used the diagram of MIR color indices (Fig. 4.1, right panel) to select sources in a possible transition phase between starburst and QSO activity. The classification is based on the fact that AGN-dominated (power law) sources occupy a different locus than starbursts of characteristic interstellar dust temperature of $10-10^2 K$ (Downes & Solomon 1998). We opt to use the definitions that are based on all IRAS bands, since they are less susceptible to data reduction approximations and

(possibly subjective) thresholds set. We refine the IR-excess definition to take into account both the ratio of the IR over the optical/ultraviolet luminosity and the MIR color-index diagram. As IR-excess we classify those sources that have $L_{\rm IR}/L_{\rm bb} > 0.46$ and lie between the AGN- and starburst- dominated locii on the diagram of MIR color indices.

Five sources satisfy the IR-excess criteria set, namely, PG 0050+124, PG 1119+120, PG 1126-041, PG 1426+015, and PG2130+099. Using the IR-excess PG QSO subsample to perform all calculations yields a mean velocity dispersion of 180 km s^{-1} with a standard deviation of 15 km s^{-1} and a standard error of 6 km s^{-1} . This mean σ value is insignificantly (less than 1-Gaussian sigma) smaller than that of our entire sample. Therefore, we find no particular reason to separately compare the dynamical properies of IR-excess QSOs to those of ULIRGs; the evolutionary discussion that follows refers to the entire QSO sample under examination.

The mean velocity dispersion of all QSO hosts is 1.16 times that of ULIRG remnants (see Paper II). This difference in σ corresponds to a difference in mass of $\sim 5 \times 10^{10}$ $M_{\odot}$. That the measured difference in the mass is $\sim 10^{11}$ $M_{\odot}$ can mainly be attributed to the effective radii of QSOs which are twice as large as those of ULIRGs [9]. According to Tacconi et al. (2002), the measured effective radii of the gas-rich merger remnants may increase when the ultraluminous phases cease, since the strongly nucleated starburst emission will eventually fade away. Under this hypothesis, the difference in the stellar mass of the QSO hosts and the elliptical galaxies that ULIRGs will finally form, may be smaller than that measured at present time.

The fact that the average black hole mass of PG QSOs is greater than that of ULIRG remnants while their accretion rates are of the same order is reasonable if the evolutionary scenario that relates the two were correct. The amount of gas that falls onto the AGN as the merger progresses increases from the ultraluminous to the QSO and finally to the quiescent phase; still, during the first two phases substantial amounts of gas are still present to permit the AGN to accrete at high rates.

4.5 Discussion

4.5.1 Relation of PG QSOs to gas-rich mergers

In this section, we place our results for the QSO host dynamics into a wider evolutionary framework by combining multiwavelength spectroscopic and imag-

[9] We note that the QSO mass corresponds to that of the bulge while that of the ULIRGs to the dynamical one, which, for the radii we work on, is practically equal to that of the stars.

ing evidence that links QSOs to gas-rich (not necessarily ultraluminous) mergers. In several cases, the triggering of a QSO phase from mergers or interactions is unambiguous.

Some sources in our sample are binary systems; for example, the imaging analysis of PG 1119+120 by Surace et al. (2001) showed that the main nucleus has an elongated north-west companion. According to Guyon et al. (2006) PG 1126-041 also interacts with a galaxy 6.6 kpc away. Stockton (1982) and Canalizo & Stockton (2001) spectroscopically confirmed that PG 0050+124 has a companion galaxy 16.5 kpc to the west of the QSO. Hubble Space Telescope (HST) imaging data presented in Schade et al. (2000) indicated the presence of a second nucleus south-west of the bright nucleus of PG 1426+015 (also see the acquisition image on Fig. 4.4, left panel). Our host absorption-line spectroscopy of PG 1426+015 confirms that the redshift of the second nucleus is identical to that of the QSO. The projected nuclear separation of the interacting galaxies is 4.4 kpc. The bright (NE) nucleus has an optical spectrum with broad emission features (Kaspi et al. 2000), representative of a type I AGN. Its $H-$band spectrum, mainly dominated by the strong AGN continuum, has $\sim$30 times more photon counts than that of the faint SW nucleus (see Fig. 4.4, right panel). Such large differences in the number counts of the AGN continuum and the host galaxy are typical of all the QSOs presented in this work. PG 1426+015, PG 1126-041, and PG 0050+124 are amongst the objects in our sample for which the QSO phase has been reached already before the individual nuclei coalesce[10] (see also McLeod & Rieke 1994b).

Other sources show clear signs of interaction such as distrurbed morphology (e.g. PG 1211+143; PG 2214+139; Surace et al. 2001; Guyon et al. 2006) and tidal tails (e.g. PG 0007+106; Surace et al. 2001). Since all these systems are also LIRGs, they constitute good examples of how mergers that involve gas-rich galaxies can simultaneously initiate strong AGN-accretion and starburst events.

Various pieces of evidence for star-formation exist in several of our sources. Canalizo & Stockton (2001) have modeled the optical spectra of 9 ULIRGs and QSOs suspected to be in a possible ULIRG/QSO transition phase (from their MIR color-index diagram). They find that the spectra of most of their objects are described by a combination of old and recently formed stellar populations. The ages derived for the starbursts were $< 300\ Myr$. According to Canalizo & Stockton (2001), one of the sources in our sample, PG 0050+124 (or I Zw 1) has ongoing star formation.

In the MIR, SPITZER IRS spectroscopy performed for QSOs and ULIRGs

[10] on the other hand, PG 1119 has a bolometric luminosity $< 10^{12}\ M_{\odot}$ (Surace et al. 2001)

for our QUEST project (PI Veilleux) indicates the presence of starbursts in PG QSOs. Polycyclic Aromatic hydrocarbon (PAH) molecule emission (related to star formation) has been individually detected for 11 of the 26 QSOs observed (Schweitzer et al. 2006). For the remaining sources, stacking of the spectra also reveales the presence of PAHs. The ratio between the PAH (or the low-excitation [NeII] line) and the FIR luminosity is similar in ULIRGs and QSOs (Schweitzer et al. 2006). Further similarities between the two populations revealed from MIR spectroscopy will be presented in forthcoming papers (Veilleux et al. 2006, in preparation; Netzer et al. 2006, in preparation).

Evans et al. (2001) compiled a sample of 10 PG QSOs with CO J=(1-0) gas emission detected. The CO luminosities were at most an order of magnitude lower than those of ULIRGs (Evans et al. 2001; Downes & Solomon 1998; references therein). Detection of molecular CO gas was reported in Scoville et al. (2003) for 6 more PG QSOs, of which, PG 0050+124 was the source with the greatest molecular gas mass ($\sim 10^{10}$ $M_{\odot}$, for a CO-to-H_2 conversion factor of 4 $M_{\odot}$ $K^{-1}[km/s]^{-1}pc^{-2}$).

Veilleux et al. (2006) performed HST NICMOS $H-$band imaging of (QUEST) PG QSOs and found that the difference between their host surface brightness and that of ULIRGs is insignificant. Therefore, the position of PG QSOs and ULIRGs on the $R_{\rm eff}$-$\mu_{\rm eff}$ projection of the fundamental plane (Kormendy relation; Kormendy 1985) was similar.

We now place both QSOs and various types of merger end-products to the fundamental plane to better visualize the phase-space that each population occupies (see Fig. 4.8). The panel are identical to those of Fig. 4.5. Local ULIRGs (Genzel et al. 2001; Tacconi et al. 2002; Paper II; Rothberg & Joseph 2006) are shown in triangles and LIRGs (Shier & Fischer 1998; James et al. 1999; Rothberg & Joseph 2006; Hinz & Rieke 2006) in circles. Other, visually-selected merger remnants (Rothberg & Joseph 2006) are plotted as boxes; this category may include mergers of various categories (e.g. spiral-spiral, elliptical-spiral, elliptical-elliptical), possibly including former ULIRGs and LIRGs the starbursts of which have now faded away. Other QSOs (of optical magnitudes mainly lower than those of the PG population) are plotted as asterisks (Dunlop et al. 2003). For viewing clarity we do not overlay any early-type galaxies on this figure. PG QSOs lie at the upper end of the locus of ULIRGs and LIRGs and in the middle of the locus of visually-selected mergers; therefore a subset of all ULIRGs and PG QSOs have identical dynamical properties.

In some cases, the evidence that relates local PG QSOs and ULIRGs is unambiguous; for example, some sources are known to fulfill both the ULIRG and QSO classification criteria (e.g. PG 0157+001; PG 1226+023). Still, not all ULIRGs can be associated with PG QSOs (and vice-versa). Some of

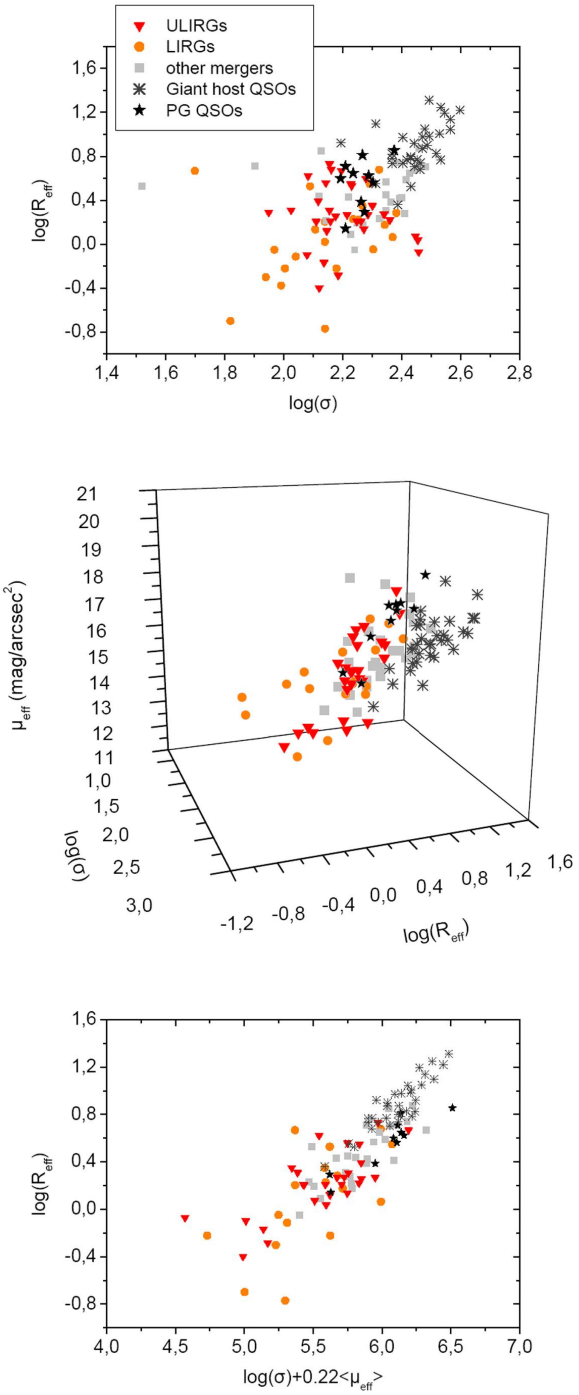

Figure 4.8: The K-band fundamental plane of merger remnants. *Upper panel:* The dynamical $R_{\rm eff}$-σ projection of the plane. *Middle panel:* The 3-d view of the plane *Lower panel:* The Pahre (1999) projection of the plane plotted for viewing clarity. In all panels, ULIRG, LIRG, and other (visually-selected) remnants are plotted as triangles, circles, and squares respectively. The merger remnant data are from Genzel et al. (2001), Tacconi et al. (2002), Paper II, Rothberg & Joseph (2006), Hinz & Rieke (2006), Shier & Fischer (1998), and James et al. (1999). The QSOs of this study as plotted as stars and the QSOs of Dunlop et al. (2003) as asterisks.

the QSOs that show a single nucleus in the imaging data, namely PG 1126-041, PG 1229+204, and PG 2130+099, have signatures of spiral structure (Surace et al. 2001; Veilleux et al. 2006). If these sources have indeed gone through a recent interaction, they were probably involved in unequal-mass major[11] or minor mergers[12], since the latter are known to form remnants with components of significant angular momentum (e.g., Bendo & Barnes 2000). Spiral structure seems to be met more often among QSO-host galaxies than among ULIRG remnants (Veilleux et al. 2006); these statistics may be justified by the fact that these QSOs have IR output comparable to that of LIRGs. LIRGs are believed to originate from a wider merger variety and larger progenitor mass ratios than those of ULIRGs (e.g., Ishida et al. 2006, in preparation). In such cases, QSO activity is triggered by initial conditions similar but not identical to those of ULIRGs.

While we cannot distinguish whether PG QSOs and ULIRGs have identical initial conditions or not, we can safely assume that both require the presence of gas-rich merger components. This assumption is supported by the fact that the majority of PG QSOs are LIRGs, and some LIRGs are plausibly the progenitors or descendants of ULIRGs. Therefore, both ULIRGs and PG QSOs experience simultaneous strong star-formation and AGN-accretion events. That starburst- and AGN- emission are related phenomena has often been stated in the literature (Scoville et al. 2003; Kauffmann et al. 2003; Di Matteo et al. 2005; Springel et al. 2005b; Lípari & Terlevich 2006).

4.5.2 Relation of PG QSOs to other QSO populations

It is important to point out that gas-rich mergers are not the direct progenitors of all local QSOs; the PG QSO sample is not selecting objects representative of all local QSO populations (Vestergaard & Peterson 2006). Selection effects and differences between the Palomar BQS and the SDSS samples have been extensively studied in Jester et al. (2005). The completeness of the BQS is reported to be smaller than that of surveys other than the SDSS, i.e. the Hamburg-ESO Quasar Survey (Wisotzki et al. 2000). Due to their B-band magnitude cutoff, $m_B \lesssim 16$, the BQS sample selects the brightest local AGNs, and therefore, those that accrete at high rates (see § 4.2.1).

A sample compiled with the opposite magnitude cutoff will mainly include faint AGNs (that accrete at low rates); such an example is the V-band magnitude $m_V \gtrsim 15$ radio-loud (RL) or radio-quiet (RQ) QSO population at $0.138 < z < 0.258$ of Dunlop et al. (2003). These authors selected objects fainter than 15 mags in the V-band, to match the optical properties of the

[11] of progenitor mass ratio ∼3:1
[12] of progenitor mass ratio >3:1

entire sample to those of their RL subsample (Dunlop et al. 1993). These RL QSOs and their optical RQ counterparts have, indeed, supermassive black holes of 10^8-10^9 $M_\odot$ that accrete at low rates ($\sim$0.055 of the Eddington value) and are typically located on massive elliptical hosts (of mean bulge mass 5.6×10^{11} $M_\odot$). To better illustrate how the PG and the Dunlop et al. (2003) flux-limited samples are complementary in sampling the entire range of AGN properties in local QSOs, we place the RL/RQ Dunlop et al. (2003) sources on the fundamental plane of early-type galaxies (see Figs. 4.5, 4.8; asterisks).

The location of the RL/RQ QSOs on the fundamental plane is identical to that of giant ellipticals and does not overlap with that of ULIRGs. As reported in Tacconi et al. (2002) and Dunlop et al. (2003), such differences in the locii of the two populations indicate that their origin may be sought in different mechanisms. That PG QSOs are located between ULIRGs and massive-host QSOs indicates that gas-rich mergers can produce black holes of a specific mass sizes and cannot account for the formation of all local AGNs. A possible scenario for the formation of 5×10^8-10^9 $M_\odot$ BH QSOs is by the reignition of a 10^7-$10^8 M_\odot$ black hole with a new interaction with a gas-rich source or through the merger of gas-depleted galaxies, i.e. via elliptical-elliptical mergers. In either case, a series of merging events is required for the formation of the supermassive AGN and the giant E host.

A similar conclusion may be derived from the comparison to SDSS radio-loud sources. Best et al. (2005) have recently found a dependence between radio-activity and the size of the host galaxy and black hole mass; the bulk of radio emission mainly originates from the sources with the most massive black holes ($log[\, M_{\rm BH}] \gtrsim 8.2$) and the most massive bulges in their sample. Similar to the most massive sources in the Dunlop et al. (2003) sample, such SDSS radio-loud QSOs likely have a different formation history than that of PG QSOs.

4.6 Conclusions

We have acquired spectroscopic H-band long-slit, data of 12 mainly PG QSOs to study the dynamical properties of their hosts and investigate whether they have an origin analogous to that of ULIRGs. The compiled sample is representative of all local PG QSOs and appropriate to investigate the triggering of QSO activity by mergers. We find that:

1. The long-integration, excellent-seeing-condition spectroscopic data obtained from the VLT have enabled us to directly extract host-galaxy dispersion and dynamic properties of local QSOs in the H band.

2. The individual stellar velocity dispersions vary from 156 to 237 km s^{-1} . The mean σ value of the sample is 186 km s^{-1} with a standard deviation and error of 24 and 7 km s^{-1} . The host galaxies have bulges of $\sim$1.5 m_* stellar mass.

3. The black hole masses of the PG QSOs are of the order 5×10^7-$10^8 M_\odot$ and accrete at Eddington efficiencies of the order 10^{-1}.

4. The measurement of the host velocity dispersion enables us to place some PG QSOs on the AGN $M_{\rm BH} - \sigma$ relation, acknowledging the large error bars and possible systematics of the measurement. They are located above the AGN (and closer to the quiescent-galaxy) best-fit formula.

5. The BH and host-galaxy properties of our entire sample and the IR-excess subsample are insignificantly different. The dynamical properties of all QSOs in our sample overlap only with those of the most massive ULIRGs. This result is confirmed by the position of the PG QSOs on the fundamental plane of early-type galaxies, which is between the locii that moderate-mass and giant Es occupy.

6. In some sources, the starburst and strong AGN-accretion phase is unambiguously triggered by a merger event. A scenario where some ULIRGs may undergo a QSO phase as the merger evolves is therefore plausible. The same applies for a scenario which assumes that some ULIRGs and QSOs may have similar, but not identical, initial conditions (gas-rich mergers). Since there is no evidence that favorizes one of those scenarios, both may simultaneously hold.

7. Since PG QSOs constitute only a fraction of the local QSO population, in particular those with the most active AGNs, an argument claiming that gas-rich mergers are the direct ancestors of all QSOs cannot be supported. Sources of $M_{\rm BH}$ 5×10^8-$10^9 M_\odot$ probably have a different origin.

Acknowledgments:
We are grateful to ESO for the acquisition of excellent-quality data during the service-mode observations. K. M. Dasyra wishes to thank M. Vestergaard for helpful suggestions. A. J. Baker acknowledges support from the National Radio Astronomy Observatory, which is operated by Associated Universities, Inc., under cooperative agreement with the National Science Foundation.

5
Conclusions

We have acquired spectroscopic near-infrared long-slit data of 54 ULIRGs at a variety of merger phases and 12 local PG QSOs to study:

1. the interaction conditions that trigger ultraluminous activity,
2. the evolution of the galaxy kinematics in gas-rich mergers,
3. the end products of ultraluminous mergers, and
4. the triggering of QSO activity by gas-rich mergers.

From the host kinematics extracted from the CO absorption-bandheads, we find that:

1. The mass ratio of the individual components in binary ULIRGs is measured directly from the kinematics of each nucleus; its mean value is 1.5:1. The kinematic properties of ULIRG remnants also indicate that they mainly originate from mergers of 1:1 and 2:1 progenitor mass ratios, when compared to those predicted by models. Therefore, ultraluminous activity is mainly related to gas-rich galaxy mergers of comparable-mass components. Less frequently, unequal major mergers of 3:1 mass ratio do appear in our sample; however, the number of 3:1 mergers we observed may be somewhat underestimated due to the dynamical heating of the merging components and projection effects. Mergers of mass ratios $> 4:1$ are unlikely to form ULIRGs since they are not violent

enough to drive an adequate amount of gas to the center of the merging system, and therefore, to create the appropriate pressure conditions for strong starbursts.

2. Indications of an increase of the stellar random motions exist as the merger advances. The mean stellar σ equals 142 km s^{-1} for the pre-coalescence binary sources and 161 km s^{-1} for the remnants; the respective uncertainty in the mean is 3 and 7 km s^{-1} . The confidence of this result is at 2.3 Gaussian sigma; since this difference in the means of the pre- and post- coalescence distributions is marginally significant, it requires further data to be accurately constrained, prior to being compared to that of models. Furthermore, any increase of the stellar dispersion observed in ULIRGs corresponds to only a part of the dynamical heating that occurs during the merger, since the merger timescales are longer than those of the ultraluminous starburst.

3. Ultraluminous mergers will mainly lead to the formation of dispersion-supported systems of stellar mass $\sim 10^{11} M_{\odot}$. Depending on the definition of m_*, ULIRGs are between sub- and $\sim m_*$. Their black hole masses are of an order 10^7-$10^8 M_{\odot}$ and their accretion rates are high (Eddington efficiencies often > 0.5). This result implies the black holes of the objects that will finally form will be larger than those observed at present time; gas-mass arguments indicate that the final black hole masses will probably still be constrained to an order of 10^8 $M_{\odot}$. The remnants of ultraluminous mergers are located in a region of the fundamental plane of early-type galaxies characteristic of that of moderate-mass ellipticals and different from that of giant Es. Local mass and dispersion functions further support this argument. While the current statistics cannot exclude the formation of few giant Es from ULIRGs, the latter probably have a different formation history. Other kinds of mergers (e.g. spiral-elliptical or elliptical-elliptical) are the most probable progenitors of local giant Es.

4. The extraction of the host kinematics in QSOs was succesfully performed from the excellent-seeing-condition spectroscopic data from the VLT. The dispersions are somewhat larger than (but still within the range of) those of ULIRGs; the σ values vary from 156 to 237 km s^{-1} . The mean σ value of the sample is 186 km s^{-1} with an uncertainty of 7 km s^{-1} . The host galaxies have bulges of $\sim 1.5 m_*$ stellar mass. The black hole masses of the PG QSOs are of the order 5×10^7-$10^8 M_{\odot}$ and accrete at $\sim 0.2 - 0.3$ Eddington efficiencies. These dynamical properties overlap only with those of the most massive ULIRGs. The position of the

PG QSOs on the fundamental plane of early-type galaxies is between the locii that moderate-mass and giant Es occupy. Therefore, some ULIRGs and PG QSOs have a common origin. In some cases, unambiguous evidence that links the two populations exist. In most cases, PG QSOs are LIRGs; only a part of the local LIRG population are direct progenitors or ancestors of ULIRGs. Therefore, we cannot disentangle between a scenario where some ULIRGs undergo a QSO phase as the merger evolves and a scenario which assumes that ULIRGs and QSOs may have similar, but not identical, initial conditions. What seems certain is that PG QSOs are often involved in gas-rich mergers or interactions. Since PG QSOs constitute the local QSO population with the most active AGNs, an argument claiming that all local QSOs originate from gas-rich mergers QSOs cannot be supported; in fact, QSOs with $M_{\rm BH}$ 5×10^8-$10^9 M_\odot$ are believed to have a different origin, probably linked to a series of merger events that involves (an) elliptical component(s).

I am grateful to the MPE group for confiding in me the reduction and analysis of datasets of an equivalent time of 24 nights on the Very Large Telescope. In particular, I would like to thank my supervisors L. Tacconi and R. Genzel for the scientific input and support.

I wish to thank all the collaborators for the wonderful opportunity to work in a coordinated multi-wavelength effort to understand the nature of local ULIRGs. Of those, I wish to acknowledge the detailed theoretical input of T. Naab and A. Burkert, the great technical knowledge of R. Davies, and the helpful suggestions of D. Lutz; without those this work would have been incomplete. I deeply appreciate the fruitful collaboration with B. Peterson, the detailed input of A. Baker, and the constant guiding from my former supervisor, N. Kylafis.

To my parents and all my good frieds, I would like to say a big thanks for supporting me at hard times.

APPENDIX

Notes on individual objects

IRAS 00091-0738: This source has two overlapping nuclei separated by 1.4 kpc. Archival Wide Field Planetary Camera data of this source (PI Borne) also indicate an optical nuclear separation of 1.5 kpc.

IRAS 00199-0738: This object may be a multiple merger according to Duc et al. (1997). Our spectroscopy shows that the nucleus to the north of the brightest nucleus is probably not at the same redshift, and does not belong to the same system. The radial distribution of the sources to the west and south-east also matches better that of a point-like (rather an extended) source which is broadened due to seeing. It is thus possible that none of these sources belongs to the particular merger.

IRAS 00456-2904: According to the imaging analysis of Kim et al. (2002) and Veilleux et al. (2006) this source is probably a binary system at projected nuclear separation of 22.2 kpc (converted to our cosmology). The redshift of the NE nucleus is not spectroscopically confirmed but its ambiguous morphology indicates an interaction. The data presented in this paper are for the more luminous (late-type-host) SW nucleus.

IRAS 02364-4751: The spectroscopic results for this source indicate that the difference in the dispersion of the two nuclei is 51 km s^{-1} . Given the phase of the merger (nuclear separation of 1.5 kpc), one would expect smaller deviations in the progenitor dispersions which should be closer to their common equilibrium value. However, the spectroscopic results show that the south nucleus has a large recession velocity with respect to its counterpart. This fact, combined with the proximity of the sources (that leads to a spatial overlap of the spectra of the two nuclei) gives rise to an unrealistic increase of the southern nucleus dispersion.

IRAS 09111-1007: Duc et al. (1997) find that this source has two widely separated interacting nuclei; the ultraluminous IR component is the western source. The nuclear separation measured from our acquisition images equals 40.4 kpc.

IRAS 10565+2448: A dwarf galaxy is seen at 6.5 kpc south-east of the bright nucleus, while the second nucleus of the merging system is at the north-east

of the bright nucleus (see Murphy et al. 1996). The $V_{\rm rot}$ value of this source is more likely between the inclination corrected and non-corrected one, because it is in an early merger stage (nuclear separation of 21.7 kpc), thus its $V_{\rm rot}$ and $V_{\rm rot}/\sigma$ ratio will probably be closer to those of a spiral.

IRAS 11095-0238: Recent H-band imaging obtained with the NICMOS camera at the HST confirms that this is a close binary system (Veilleux et al. 2006, in preparation).

IRAS 12071-0444: This source was presented in Tacconi et al. (2002) as a merged system. The data presented here (taken under better seeing conditions) show the presence of two separate nuclei. HST NICMOS observations have also indicated the presence of two nuclei (Veilleux et al. 2006, in preparation).

IRAS 14348-1447: According to the NICMOS imaging of Scoville et al. (2000), this source has a projected nuclear separation of 6.0 kpc (converted to our cosmology).

IRAS 14378-3651: Two components separated by 1.5 kpc are visible in the acquisition image of this source.

IRAS 15250+3609: The two components of this source are separated by 0.8 kpc (Scoville et al. 2000).

IRAS 20046-0623: While two nuclei appear in the H-band images of this source, IRAS 20046-0623 has often been treated as a single object in the literature due to the faintness of the eastern nucleus and the phase of the merger. We have been able to extract the structural parameters and the spectroscopic results of the west, bright nucleus only.

IRAS 21329-2346: When deriving the H-band luminosity ratio of this system from the (non-PSF subtracted) NICMOS images of Veilleux et al. (2006, in preparation), we find a luminosity ratio of 2.53, in good agreement with our results.

IRAS 23578-5307: Our acquisition image indicates the presence of two nuclei separated by 1.4 kpc.

Arp 220: This source has a projected nuclear separation of 0.3 kpc (Scoville et al. 1998).

NGC 6240: The two nuclei of this source are separated by 1.4 kpc still show some discrete velocity patterns. The velocity dispersion of the system peaks between them; at the position of this peak the stellar kinematics may reflect localized motions of self-gravitating gas (Tecza et al. 2000; Genzel et al. 2001). For the velocity dispersion of this source we use the average of the value at two nuclei and at the internuclear peak which equals 229 km s^{-1} and which is close to the luminosity-averaged value, 225 km s^{-1} (Tecza et al. 2000).

Mrk 273: The nuclei of Mrk 273 are 0.8 kpc apart (Scoville et al. 2000).

Bibliography

Arp, H. 1966, ApJS, 14, 1

Baes, M. & Dejonghe, H. 2002, MNRAS, 335, 441

Barnes, J. E. 1992, ApJ, 393, 484

Barnes, J. E, & Hernquist, L., 1996, 471, 115

Barnes, J. E. 2001, ASP Conference Series 245: Astrophysical Ages and Timescales, eds. T. von Hippel, C. Simpson, N. Manset (San Fransisco: ASP), 382

Barnes, J. E. 2002, MNRAS, 333, 481

Barth, A. J., Greene, J. E., & Ho, L. C. 2005, ApJ, 619, L151

Baskin, A., & Laor, A. 2005, MNRAS, 356, 1029

Bell, E. F., McIntosh, D. H., Katz, N., Weinberg, M. D. 2003, ApJS, 149, 289

Bell, E. F. et al. 2006, ApJ, 640, 241

Bender, R. 1990, A&A, 229, 441

Bender, R., Burstein, D., & Faber, S. M. 1992, ApJ, 399, 462

Bendo, G. J., & Barnes, J. E. 2000, MNRAS, 316, 315

Bernardi, M. et al. 2003, AJ, 125, 1817

Bertin, E., & Arnouts, S. 1996, A&AS, 117, 393

Best, P. N., Kauffmann, G., Heckman, T. M., Brinchmann, J., Charlot, S., Ivezić, Z., & White, S. D. M. 2005, MNRAS, 362, 25

Binney, J., & de Vaucouleurs, G. 1981, MNRAS, 194, 679

Binney J., & Tremaine S. 1987, Galactic Dynamics, Princeton Univ. Press.

Blandford, R. D., & McKee, C. F. 1982, ApJ, 255, 419

Bryant, P. M., & Scoville, N. Z. 1999, AJ, 117, 2632

Burkert, A. & Naab, T. 2005, MNRAS, 363, 597

Canalizo, G., & Stockton, A. 2001, ApJ, 555, 719

Cappellari, M., et al. 2005, in press, astro-ph/0505042

Cappellari, M., et al. 2005, in press, astro-ph/0509470

Cattaneo, A., Combes, F., Colombi, S., Bertin, E., & Melchior, A.-L. 2005, MNRAS, 359, 1237

Chaffee, F. H., Foltz, C. B., Hewett, P. C., Francis, P. A., Weymann, R. J., Morris, S. L., Anderson, S. F., & MacAlpine, G. M. 1991, AJ, 102, 461

Cole, S., et al. 2001, MNRAS, 326, 255

Colina, L, et al. 2001, ApJ, 563, 546

Colina, L., Arribas, S., Monreal-Ibero, A. 2005, ApJ, 621, 725

Collin, S., Kawaguchi, T., Peterson, B., & Vestergaard, M. 2006, A&A accepted (astro-ph/0603460)

Dasyra, K. M., Tacconi, L. J., Davies, R.I., Lutz, D., Genzel, R., Burkert, A., Veilleux, S. & Sanders, D. 2006, ApJ, 638, 745

Dasyra, K. M., Tacconi, L. J., Davies, R.I., Naab, T., Genzel, R., Burkert, A., Veilleux, S. & Sanders, D. 2006, ApJ, submitted

Di Matteo, T., Springel, V., & Hernquist, L. 2005, Nature, 433, 604

Djorgovski, S., & Davis, M. 1987, ApJ, 313, 59

Downes, D., & Solomon, P.M. 1998, ApJ, 507, 615

Dressler, A., Lynden-Bell, D., Burstein, D., Davies, R. L., Faber, S. M., Terlevich, R., & Wegner, G. 1987, ApJ, 313, 42

Duc P.-A., Mirabel, I.F., & Maza, J. 1997, A&AS, 124, 533

Dunlop, J. S., Taylor, G. L., Hughes, D. H., & Robson, E. I. 1993, MNRAS, 264, 45

Dwek, E., et al. 1998, ApJ, 508, 106

Dunlop, J. S, McLure, R. J., Kukula, M. J., Baum, S. A., O'Dea, C. P., & Hughes, D. H. 2003, MNRAS, 340, 1095

Efstathiou, G., & Rees, M. J. 1988, MNRAS, 230P, 5

Elbaz, D. 2005, to appear in "ISO Science Legacy: A Compact Review of ISO Major Achievements"

Elvis, M., et al. 1984, ApJS, 95, 1

Evans, A. S., Frayer, D. T., Surace, J. A., & Sanders, D. B. 2001, AJ, 121, 1893

Faber, S. M., et al. 1997, AJ, 114, 1771

Ferrarese, L., & Merritt, D. 2000, ApJ, 539, L9

Ferrarese, L., Pogge, R. W., Peterson, B. M., Merritt, D., Wandel, A., Joseph, C. L. 2001, ApJ, 555, L79

Ferrarese, L. 2002, ApJ, 578, 90

Gao, Y., & Solomon, P. M. 1999, ApJ, 512, L99

Gebhardt, K. et al. 2000, ApJ, 539, L13

Gebhardt, K. et al. 2000, ApJ, 543, L5

Gebhardt, K., Bender, R., Bower, G., Dressler, A., Faber, S. M., Filippenko, A. V., Green, R., Grillmair, C., Ho, L. C., Kormendy, J., Lauer, T. R., Magorrian, J., Pinkney, J., Richstone, D., & Tremaine, S. 2001, ApJ, 555L, 75

Genzel, R., Lutz, D., Sturm, E., Egami, E., Kunze, D., Moorwood, A. F. M., Rigopoulou, D., Spoon, H. W. W., Sternberg, A., Tacconi-Garman, L. E., Tacconi, L., & Thatte, N. 1998, ApJ, 498, 579

Genzel, R., Tacconi, L. J., Rigopoulou, D., Lutz, D., & Tecza, M. 2001, ApJ, 563, 527

Greve, T. R., et al. 2005, MNRAS, 359, 1165

Guyon, O., Sanders, D. B., & Stockton, A., 2006, ApJ, submitted

Haas, M., et al. 2003, A&A, 402, 87

Haehnelt, M. G., & Rees, M. J., 1993, MNRAS, 263, 168

Haehnelt, M. G. 2004, in Carnegie Observatories Astrophysics Series, Vol. 1: Coevolution of Black Holes and Galaxies, ed. L.C. Ho (Cambridge: Cambridge Univ. Press), 406; (astro-ph/0307378)

Haering, N., & Rix, H.-W. 2004, ApJ, 604L, 89

Hernquist, L. 1993, ApJ, 409, 548

Hernquist, L., Spergel, D. N., & Heyl, J. S. 1993, ApJ, 416, 415

Hernquist, L., & Mihos, J. C. 1994, AAS, 185, 7508

Hernquist, L., & Mihos, J. C. 1995, ApJ, 448, 41

Hinz, J. L., & Rieke, G. H., 2006, astro-ph/0604286

Holmberg, E. 1941 ApJ, 94, 385

Hopkins, P. F., Hernquist, L., Cox, T. J., Di Matteo, T., Martini, P., Robertson, B., & Springel, V. 2005, ApJ, 630, 705

Hopkins, P. F. et al. 2006, ApJ, submitted, astro-ph/0602290

Houck, J. R., Schneider, D. P., Danielson, G. E., Neugebauer, G., Soifer, B. T., Beichman, C. A., & Lonsdale, C. J. 1985, ApJ, 290L, 5

Ishida, C. M. 2004, Ph. D. Thesis, University of Hawaii

James, P., Bate, C., Wells, M., Wright, G., & Doyon, R. 1999, MNRAS, 309, 585

Jarrett, T. H., Chester, T., Cutri, R., Schneider, S. E., & Huchra, J. P. 2003, AJ, 125, 525

Jester, S., et al. 2005, AJ, 130, 873

Joint Iras Science Working Group, 1988, Infrared Astronomical Satellite Catalogs, The Point Source Catalog v. 2.0, IRASP, C2, 0000

Joseph, R. D. 1999, Ap&SS, 266, 321

Kaspi, S., Smith, P. S., Netzer, H., Maoz, D., Jannuzi, B. T., Giveon, U. 2000, ApJ, 533, 631

Kaspi, S., Maoz, D., Netzer, H., Peterson, B. M., Vestergaard, M., Jannuzi, B. T. 2005, ApJ, 629, 61

Kauffmann, G.; White, S. D. M. 1993, MNRAS, 261, 921

Kauffmann, G., & Haehnelt, M. 2000, MNRAS, 311, 576

Kauffmann, G., et al. 2003, MNRAS, 346, 1055

Kaviraz, S., Devriendt, J. E. G., Ferreras, I., Yi, S. K., & Silk, J. 2006, MNRAS, submitted, astro-ph/0602347

Khochfar, S., Burkert, A. 2003ApJ, 597L, 117

Kim, D.-C., & Sanders, D. B. 1998, ApJS, 119, 41

Kim, D.-C., Veilleux, S., & Sanders, D. B. 2002, ApJS, 143, 277

Kochanek, C. S., et al. 2001, ApJ, 560, 566

Kormendy, J. 1985, ApJ, 292L, 9

Kormendy, J., Sanders, D. B. 1992, ApJ, 390L, 53

Lagache, G. et al. 2004, ApJS, 154, 112

Lake, G., & Dressler, A. 1986, ApJ, 310, 605

Le Fèvre, O., et al. 2000, MNRAS, 311, 565

Lípari, S. 1994, ApJ, 436, 10

Lípari, S. , & Terlevich, R. 2006, MNRAS, submitted (astro-ph/0602090)

Lonsdale, C. J., Farrah, D., & Smith, H. E., 2006, in "Astrophysics Update 2 - topical and timely reviews on astronomy and astrophysics", ed. J. W. Mason, Springer/Praxis books (astro-ph/0603031)

Lucy, L. B. 1974, AJ, 79, 745

Lutz, D., Spoon, H. W. W., Rigopoulou, D., Moorwood, A. F. M., & Genzel, R. 1998, ApJ, 505L, 103

Lutz, D., Veilleux, S., & Genzel, R. 1999, ApJ, 517L, 13

McLeod, K. K., & Rieke, G. H. 1994, ApJ, 420, 58

McLeod, K. K., & Rieke, G. H. 1994, ApJ, 431, 137

McLeod, K. K., Rieke, G. H., & Storrie-Lombardi, L. J. 1999, ApJ, 511, 67

Merritt, D., Ferrarese, L. 2001, ApJ, 547, 140

Mihos, J. C., & Hernquist, L. 1994, AAS, 185, 6802

Mihos, J. C., & Hernquist, L. 1994, ApJ, 431, L9

Mihos, J. C., & Hernquist, L. 1996, ApJ, 464, 641

Mihos, J. C., & Bothun, G. D. 1998, ApJ, 500, 619

Mihos, J. C. 1999, Ap&SS, 266, 195

Mihos, J. C. 2000, ASPC, 197, 275

Moorwood, A. F. M., et al. 1998, Messenger, 94, 7

Moshir, M. et al., 1990, Infrared Astronomical Satellite Catalogs, The Faint Source Catalog, v 2.0, IRASF, C, 0000

Moshir, M., et al. 1990, IRAS Z.C. 000

Murphy, T. W., Jr., Armus, L., Matthews, K., Soifer, B. T., Mazzarella, J. M., Shupe, D. L., Strauss, M. A., & Neugebauer, G. 1996, AJ, 111,1025

Murphy T. W., Soifer, B. T., Matthews, K., & Armus, L. 2001, ApJ, 559, 201

Naab, T., & Burkert, A. 2003, ApJ, 597, 893

Naab, T., Khochfar, S., & Burkert, A. 2006, ApJ, 636, L81

Nelson, C., Green, R. F., Bower, G., Gebhardt, K., & Weistrop, D. 2004, ApJ, 615, 652

Netzer, H. 2003, ApJ, 583L, 5

Neri, R., et al. 2003, ApJ, 597, L113

Press, W. H., Teukolsky, S. A., Vetterling, W. T., & Flannery, B. P. 1992, Numerical Recipes in C: The Art of Scientific Computing, Second Edition, Cambridge University Press

Oliva, E., Origlia, L., Kotilainen, J. K., & Moorwood, A. F. M. 1995, A&A, 301, 55O

Oliva, E., Origlia, L., Maiolino, R., & Moorwood, A. F. M. 1999, A&A, 350, 9

Onken, C. A., Ferrarese, L., Merritt, D., Peterson, B. M., Pogge, R. W, Vestergaard, M., & Wandel, A. 2004, ApJ 615, 645

Pahre, M. A. 1999, ApJS, 124, 127

Peterson, B. M. 1993, PASP, 105, 247

Peterson, B. M., et al. 2004, ApJ, 613, 682

Pérez-González, P. G., et al. 2005, ApJ, 630, 82

Pizzella, A., Corsini, E. M., Dalla Bonta, E., Sarzi, M., Coccato, L., Bertola, F. 2005, ApJ, 631, 785

Puget, J.-L., Abergel, A., Bernard, J.-P., Boulanger, F., Burton, W. B., Desert, F.-X., & Hartmann, D. 1996, A&A, 308, L5

Richardson, W. H. 1972, OSAJ, 62, 55

Rigopoulou, D., Spoon, H. W. W., Genzel, R., Lutz, D., Moorwood, A. F. M., & Tran, Q. D. 1999, AJ, 118, 2625

Robertson, B., Hernquist, L., Cox, T. J., Di Matteo, T., Hopkins, P. F., Martini, P., & Springel, V. 2006, ApJ, 641, 90

Robertson, B., Cox, T. J., Hernquist, L., Franx, M., T., Hopkins, P. F., Martini, P., & Springel, V. 2006, ApJ, 641, 21

Rothberg, B., & Joseph, R. D. 2004, AJ, 128, 2098

Rothberg, B., & Joseph, R. D. 2006, AJ, 131, 185

Rupke, D. S., Veilleux, S., & Sanders, D. B. 2002, ApJ, 570, 588

Rupke, D. S., Veilleux, S., & Sanders, D. B. 2005, ApJS, 160, 115

Rupke, D. S., Veilleux, S., & Sanders, D. B. 2005, ApJ, 632, 751

Sargent, W. L. W., Schechter, P. L., Boksenberg, A., Shortridge, K. 1977, ApJ, 212, 326

Simkin, S. M. 1974, A&A, 31, 129

Sanders, D. B., Soifer, B. T., Elias, J. H., Madore, B. F., Matthews, K., Neugebauer, G., & Scoville, N. Z. 1988, ApJ, 325, 74

Sanders, D. B., Soifer, B. T., Elias, J. H., Neugebauer, G., Matthews, K. 1988, ApJ, 328L, 35

Sanders, D. B., Phinney, E. S., Neugebauer, G., Soifer, B. T., & Matthews, K. 1989, ApJ, 347, 29

Sanders, D. B., & Mirabel, I. F. 1996, ARA&A,34,749

Sanders, D. B. 1999, Ap&SS, 266, 331

Sanders, D. B., Kim, D. C., Mazzarella, J. M., Surace, J. A., & Jensen, J. B. 2000, ASPC, 197, 295

Sanders, D. B., Mazzarella, J. M., Kim, D.-C., Surace, J. A., Soifer, B. T. 2003 AJ, 126, 1607

Schade, D. J., Boyle, B. J., & Letawsky, M. 2000, MNRAS, 315, 498

Schechter, P. 1976, ApJ, 203, 297

Schmidt, M. & Green, R. 1983, ApJ, 269, 352

Schreiber, J., Thatte, N., Eisenhauer, F., Tecza, M., Abuter, R., Horrobin, M. 2004, ASPC, 314, 380

Schweizer, F., & Seitzer, P. 1992, AJ, 104, 1039

Schweitzer, M. et al. (2006), ApJ, submitted

Scoville, N. Z., et al. 1998, ApJ, 492, L107

Scoville, N. Z., Evans, A. S., Thompson, R., Rieke, M., Hines, D. C., Low, F. J., Dinshaw, N., Surace, J. A., & Armus, L. 2000 AJ, 119, 991

Scoville, N. Z., Frayer, D. T., Schinnerer, E., & Christopher, M. 2003, ApJ, 585, L108

Sheth, R. K., et al. (2003), ApJ, 594, 225

Shier, L. M., & Fischer, J. 1998, ApJ, 497,163

Silge, J., & Gebhardt, K. 2003, AJ, 125, 2809

Springel, V. 2000, MNRAS, 312, 859

Springel, V., Di Matteo, T., & Hernquist, L. 2005 ApJ, 620, L79

Springel, V., & Hernquist, L. 2005 ApJ, 622, L9

Springel, V., Di Matteo, T., & Hernquist, L. 2005, MNRAS, 361, 776

Springel, V. et al. 2005, Natur, 435, 629

Stockton, A. 1982, ApJ, 257, 33

Surace, J. A.. Sanders, D. B., Vacca, W. D., Veilleux, S., & Mazzarella, J. M. 1998 ApJ, 492, 116

Surace, J. A., & Sanders, D. B. 1999, ApJ, 512, 162

Surace, J. A.. Sanders, D. B., & Evans, A.S. 2001, AJ, 122, 2791

Tacconi, L. J., Genzel, R., Lutz, D., Rigopoulou, D., Baker, A. J., Iserlohe, C., & Tecza, M. 2002, ApJ, 580, 73

Tacconi, L. J., et al. 2006, ApJ, 640, 228

Tecza, M., Genzel, R., Tacconi, L. J., Anders, S., Tacconi-Garman, L. E., & Thatte, N. 2000, ApJ, 537, 178

Thomas, D., Maraston, C., Bender, R., de Oliveira, C. M. 2005, ApJ, 621, 673

Toomre, A. 1977, in Evolution of Galaxies and Stellar Populations, ed. B. M. Tinsley & R. B. Larson (New Haven: Yale University Observatory), 401

Tremaine, S., Gebhardt, K., Bender, R., Bower, G., Dressler, A., Faber, S. M., Filippenko, A. V., Green, R., Grillmair, C., Ho, L. C., Kormendy, J., Lauer, T. R., Maggorian, J., Pinkney, J., & Richstone, D. 2002 ApJ, 574, 740

van Albada, T. S., Bahcall, J. N., Begeman, K., & Sancisi, R. 1985, ApJ, 295, 305

van Dokkum, P. G. 2005, AJ, 130, 2647

Veilleux, S., Kim, D.-C., & Sanders, D. B. 1999, ApJ, 522, 113

Veilleux, S., Kim, D.-C., & Sanders, D. B. 2002, ApJS, 143, 315

Veilleux, S., et al. 2006, ApJ, accepted

Vestergaard, M. 2002, ApJ, 571, 733

Vestergaard, M., & Peterson, B. M. 2005, ApJ, 625, 688

Vestergaard, M., & Peterson, B. M. 2006, ApJ, in press (astro-ph/0601303)

Wang, J. L., Xia, X. Y., Mao, S., Cao, C., Wu, H., & Deng, Z. G. 2006, ApJ, submitted

Wisotzki, L., Christlieb, N., Bade, N., Beckmann, V., Köhler, T., Vanelle, C., & Reimers, D 2000, A&A, 358, 77

Woo, J. H., Treu, T., Malkan, M. A., & Blandford, R. D. 2006, ApJ submitted, astro-ph/0603648

Zibetti, S., Gavazzi, G., Scodeggio, M., Franzetti, P., & Boselli, A. 2002, ApJ, 579, 261